UNIVERSITY OF ROCHESTER
LABORATORY FOR LASER ENERGETICS

Volume 145
October–December 2015
DOE/NA/1944-1255

LLE Review

Quarterly Report

About the Cover:

The cover photo highlights scientist Dr. Radha Bahukutumbi presenting results from simulations and experiments at the National Ignition Facility (NIF). In the background are projections of the simulated scattered light from a NIF implosion without (top) and with (bottom) cross-beam energy transfer (CBET). Measurements of scattered light in the NIF chamber can shed light on this process that can compromise the pressure that sets up the drive and the velocity of the imploding shell.

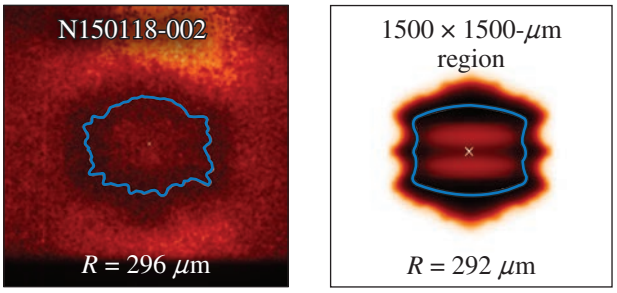

The figure on the left shows the measured and simulated radiograph, respectively, of an imploding shell on the NIF viewed from the equator using an iron backlighter and a gated framing camera. Simulations closely reproduce the measured shapes, indicating that the laser-deposition process (including the effect of CBET) and heat conduction to the ablation surface are modeled relatively well. This validation of the code is important for predictions of target performance in MJ-scale plasmas such as those in NIF implosions.

The work described in this volume includes current research at the Laboratory for Laser Energetics, which is supported by the New York State Energy Research and Development Authority, the University of Rochester, the U.S. Department of Energy Office of Inertial Confinement Fusion under Cooperative Agreement No. DE-NA00001944, and other agencies.

Printed in the United States of America
Available from
National Technical Information Services
U.S. Department of Commerce
5285 Port Royal Road
Springfield, VA 22161
www.ntis.gov

For questions or comments, contact James B. Oliver, Editor, Laboratory for Laser Energetics, 250 East River Road, Rochester, NY 14623-1299, (585) 275-1194.

www.lle.rochester.edu

UNIVERSITY OF ROCHESTER
LABORATORY FOR LASER ENERGETICS

Volume 145
October–December 2015
DOE/NA/1944-1255

LLE Review

Quarterly Report

UR LLE

Contents

In Brief

This volume of the LLE Review, covering October–December 2015, features "Direct Drive: Simulations and Results from the National Ignition Facility," by P. B. Radha, M. Hohenberger, D. H. Edgell, J. A. Marozas, F. J. Marshall, D. T. Michel, M. J. Rosenberg, W. Seka, A. Shvydky, T. R. Boehly, T. J. B. Collins, E. M. Campbell, R. S. Craxton, J. A. Delettrez, D. H. Froula, V. N. Goncharov, S. X. Hu, J. P. Knauer, R. L. McCrory, P. W. McKenty, J. F. Myatt, S. P. Regan, T. C. Sangster, and S. Skupsky (LLE); J. W. Bates, M. Karasik, and S. P. Obenschein (Naval Research Laboratory); S. N. Dixit and S. LePape (Lawrence Livermore Laboratory); J. A. Frenje, R. D. Petrasso, H. Sio, and A. Zylstra (Plasma Fusion Science Center, Massachusetts Institute of Technology); and D. D. Meyerhofer (Los Alamos National Laboratory). This article (p. 1) reports on the Laboratory for Laser Energetics' (LLE's) investigations of direct-drive implosions at the National Ignition Facility in order to validate models related to implosion velocities and the magnitude of hot-electron preheat. Implosion experiments indicate that the energetics are well-modeled when cross-beam energy transfer is included in the simulation. Trajectories from backlit images are also well predicted, although with lower velocities than theory, with discrepancies likely caused by nonuniformity growth seeded by laser imprint.

Additional research highlights presented in this issue include the following:

- A. A. Solodov, M. J. Rosenberg, J. F. Myatt, R. Epstein, S. P. Regan, W. Seka, J. G. Shaw, and M. Hohenberger (LLE); J. W. Bates (Naval Research Laboratory); and J. D. Moody, J. E. Ralph, D. P. Turnbull, and M. A. Barrios (Lawrence Livermore National Laboratory) report on hydrodynamic simulations to design a new experimental platform to investigate two-plasmon decay and other laser–plasma instabilities (p. 15). Proposed experiments utilize planar plastic targets with an embedded Mo layer to characterize the generation of hot electrons through Mo K_α fluorescence and hard x-ray emission, approximating conditions near both the equator and the pole of a polar-direct-drive implosion.

- S. X. Hu, V. N. Goncharov, R. L. McCrory, and S. Skupsky (LLE); and L. A. Collins and J. D. Kress (Los Alamos National Laboratory) report on first-principles investigations of the ionization and thermal conductivity of polystyrene (CH) over a wide range of plasma conditions (ρ = 0.5 to 100 g/cm^3 and T = 15,625 to 500,000 K) (p. 19). Hydrodynamic simulations of cryogenic deuterium–tritium targets with CH ablators on OMEGA and the National Ignition Facility predict an ~20% variation in target performance in terms of hot-spot pressure and neutron yield (gain) relative to traditional model simulations.

- V. N. Goncharov, S. P. Regan, T. C. Sangster, R. Betti, T. R. Boehly, E. M. Campbell, J. A. Delettrez, D. H. Edgell, R. Epstein, C. J. Forrest, D. H. Froula, V. Yu. Glebov, D. R. Harding, S. X. Hu, I. V. Igumenshchev, F. J. Marshall, R. L. McCrory, D. T. Michel, J. F. Myatt, P. B. Radha, W. Seka, A. Shvydky, C. Stoeckl, W. Theobald, and B. Yaakobi (LLE) and M. Gatu Johnson (Plasma Fusion Science Center, Massachusetts Institute of Technology) describe experiments on the OMEGA Laser System to evaluate cryogenic implosions that are hydrodynamically equivalent to spherical ignition designs for the National Ignition Facility (NIF) (p. 30). Current cryogenic implosions on OMEGA have reached 56 Gbar, and implosions with a shell convergence of CR < 17 and a fuel adiabat $\alpha > 3.5$ proceed close to 1-D predictions. Demonstrating hydrodynamic equivalence on OMEGA will require reduced coupling losses caused by cross-beam energy transfer and minimized long-wavelength nonuniformity. Ignition in a direct-drive cryogenic implosion on the NIF will require central stagnation pressures in excess of 100 Gbar.

- C. Stoeckl, R. Boni, F. Ehrne, C. J. Forrest, V. Yu. Glebov, J. Katz, D. J. Lonobile, J. Magoon, S. P. Regan, M. J. Shoup III, A. Sorce, C. Sorce, T. C. Sangster, and D. Weiner report on the installation of a next-generation neutron temporal diagnostic (NTD) at the Omega Laser Facility to determine the hot-spot pressure achieved in inertial confinement fusion experiments and assess the implosion quality (p. 36). This NTD is based on a fast-rise-time plastic scintillator, which converts the neutron kinetic energy to 350- to 450-nm-wavelength light that is relayed to a streak camera. An ~200× reduction in neutron background was observed during the first high-yield DT cryogenic implosions compared to the current NTD installation on OMEGA. An impulse response of ~40±10 ps was measured in a dedicated experiment with a 10-ps pulse from the OMEGA EP laser.

- S. Papernov, A. A. Kozlov, J. B. Oliver, and C. Smith (LLE); and L. Jensen, S. Günster, H. Mädebach, and D. Ristau (Laser Zentrum Hannover) report on the contribution of thin-film interfaces to the near-ultraviolet absorption and pulsed-laser–induced damage for ion-beam–sputtered and electron-beam–evaporated coatings (p. 43). Film characterization shows a small contribution to total absorption from the interfaces relative to that of the HfO_2 film material, with a higher damage resistance in the seven-layer coating compared to the single-layer HfO_2 film. The results indicate a similarity of interfacial film structure with that formed during the co-deposition of HfO_2 and SiO_2 materials.

- S.-W. Bahk, C. Dorrer, R. G. Roides, and J. Bromage describe a simple diagnostic to characterize 1-D chromatic aberrations in a broadband beam (p. 52). A Ronchi grating is placed in front of a spectrometer entrance slit to provide spatially coupled spectral phase information. The phase offset variation in the interferogram along the wavelength axis contains the information on chromatic aberrations that can be extracted using Fourier analysis. The radial-group delay of a refractive system and the pulse-front delay of a wedged glass plate have been accurately characterized in a demonstration.

James B. Oliver
Editor

Direct Drive: Simulations and Results from the National Ignition Facility

Introduction

In direct-drive inertial confinement fusion[1] nominally identical laser beams are incident on a capsule containing a layer of frozen deuterium–tritium (DT) within a shell made of an ablator such as plastic (CH). The beams ablate the outer material, driving the cryogenic DT layer inward. The shell accelerates during the laser pulse as a result of the pressure from the laser energy deposited in the corona and then decelerates when an outgoing shock is launched once the pressure in the vapor region is higher than the pressure in the inward-moving shell. The shell kinetic energy is then converted to the internal hot-spot energy during stagnation. Ignition requires that the temperature and areal density of the hot spot should be sufficient to generate heating by the alpha particles produced from the D–T fusion reaction. Several measures of target performance have been presented in the literature.[2,3] The minimum fuel energy required for ignition $E_{\min}$ considered here is given by[3]

$$E_{\min}(\mathrm{kJ}) = 50.8\,\alpha_{\mathrm{inn}}^{1.88}\left(\frac{V_{\mathrm{imp}}}{3\times 10^{7}\,\mathrm{cm/s}}\right)^{-5.89} \times\left(\frac{P}{100\ \mathrm{Mbar}}\right)^{-0.77}, \tag{1}$$

where α_{inn} is the adiabat defined as the ratio of the pressure to the Fermi-degenerate pressure in the inner surface of the shell, V_{imp} is the implosion (peak) velocity of the shell, and P is the ablation pressure. Direct drive couples ~3 to 5× more laser energy into the imploding shell than x-ray drive, resulting in larger values of V_{imp} for the same laser energy. From Eq. (1), for the same $E_{\min}$ and with larger values of V_{imp}, ignition designs with larger values of α_{inn} are possible in direct drive than from x-ray drive. Direct drive, for example, requires convergence ratios of ≳22 (defined as the ratio of initial radius to hot-spot radius at peak neutron production) to be ignition relevant, whereas x-ray drive requires convergence ratios of 30 to 40. Designs with higher adiabats are more robust to shock mistiming, preheat from fast electrons, or radiation. Higher-adiabat direct-drive designs also benefit greatly from reduced Rayleigh–Taylor (RT)[4] growth. The high power of the velocity term in Eq. (1) $\left(\sim V_{\mathrm{imp}}^{-5.89}\right)$ also indicates that robust predictions of ignition require knowledge of the shell's velocity to very high precision; a 5% decrease in velocity increases the minimum energy required for ignition by nearly 35%.

In direct drive, the implosion velocity and the ablation pressure are primarily determined by coupling the laser into the coronal plasma and the conduction of heat to the ablation surface. The equation of state has been shown to influence these quantities, although to a smaller extent.[5] While the dominant mechanism for laser-energy absorption is collisional absorption (or inverse bremsstrahlung), because of cross-beam energy transfer (CBET)[6] modifications in simulation codes are required to explain observables including capsule trajectory, scattered-light spectra and time histories, and bang times in OMEGA experiments.[7]

In CBET, ion-acoustic waves in the plasma mediate the transfer of energy from an incoming (pump) ray to an outgoing (probe) ray, reducing the energy available for deposition by the most hydrodynamically efficient incoming rays. The CBET gain factor scales as[6,7]

$$\mathrm{d}\tau_{\mathrm{CBET}} = f_{\mathrm{CBET}}\zeta_{\mathrm{pol}}\left[\frac{e^{2}}{c^{3}m_{\mathrm{e}}}\,\frac{n_{\mathrm{e}}}{1-n_{\mathrm{e}}}\,\frac{\lambda_{0}\langle Z\rangle}{\langle Z\rangle T_{\mathrm{e}}+3T_{\mathrm{i}}}\right] \times P(\eta)I_{\mathrm{pump}}\mathrm{d}s\,, \tag{2}$$

where f_{CBET} is an *ad hoc* multiplier used to explore sensitivity to the model; $\zeta_{\mathrm{pol}} = 1/4\left[1+(\hat{k}_{\mathrm{pump}}\cdot\hat{k}_{\mathrm{probe}})^{2}\right]$ is the polarization factor; e is the electron charge; c is the speed of light; m_{e} and n_{e} are the electron mass and electron density, respectively; λ_0 is the laser wavelength; $\langle Z\rangle$ is the average ionization of the material; T_{e} and T_{i} are the electron and ion temperatures, respectively; $P(\eta) = \eta\nu_{\alpha}/\left[(\eta\nu_{\alpha})^{2}+(1-\eta)^{2}\right]$ is the resonance function with $\eta = (\omega_{\mathrm{pump}}-\omega_{\mathrm{probe}}) - k_{\alpha}\cdot V_{\mathrm{fluid}}/\left|k_{\alpha}\right|c_{\alpha}$, where ω_{pump} and ω_{probe} are the pump and probe frequencies, and k_{α} is the wave number of the ion-acoustic wave given by the wave-matching condition with sound speed c_{α} and the dimensionless ion-wave damping coefficient ν_{α}; and V_{fluid} is the fluid velocity. The

energy gained or lost is given by $E_0\left[e^{d\tau_{CA}}e^{d\tau_{CBET}}-1\right]$, where $d\tau_{CA}$ is the absorption factor caused by collisional absorption. This model was implemented in the spherically symmetric code *LILAC*[8] and the axisymmetric code *DRACO*.[9] This CBET model was compared to 60-beam OMEGA implosions and, at this time, an overall multiplier $f_{CBET} = 1.5$ is required in *DRACO* to reproduce the observed neutron rates and scattered light. The reason for an overall multiplier is unknown. This fixed value of 1.5 is used in all *DRACO* simulations described in this article.

Differences between OMEGA[10] and National Ignition Facility (NIF)[11] implosions motivate the current experiments on the NIF. The simulated coronal temperature in NIF implosions is ~3.2 keV compared to ~2.75 keV in OMEGA implosions. Additionally, the path lengths ds for the rays [Eq. (2)] in the NIF corona are significantly longer; the volume in the NIF corona is approximately a factor of 1.5× larger than OMEGA-scale implosions. Therefore, it is expected that the CBET effect will be considerably larger on the NIF scale. As will be shown later, for the ongoing experiments, CBET decreases implosion velocity by ~18% and the ablation pressure by ~57%, significantly increasing E_{min}. Validating such a model and demonstrating mitigation of CBET are important to the larger direct-drive–ignition program.

The electron-heat conduction from the laser-deposition region to the ablation surface sets up the ablation pressure in direct drive. Nonlocal heat conduction[12] has been shown to play an important role in shock timing in cryogenic DT OMEGA experiments and, in combination with CBET, is required to reproduce all observables related to energetics including trajectories, bang times, time-resolved scattered light, and scattered-light spectra. It is expected that nonlocal electron thermal transport should also play an important role in NIF-scale experiments.

Preheat from two-plasmon decay (TPD)[13] is expected to be larger on the NIF scale compared to OMEGA implosions. In TPD, plasma waves accelerate electrons to energies (≥30 keV) with sufficiently long mean free paths so that their energy can be deposited in the cold shell, compromising compression or α_{inn}. TPD is a multibeam instability that requires the overlap of several beams to cooperatively overcome the threshold. In OMEGA implosions, the magnitude of the energy in the source of energetic electrons has been shown to scale with the threshold parameter η:[13]

$$\eta = \frac{I_{n_c/4}\left(\times 10^{14}\,\mathrm{W/cm^2}\right) L_{n_c/4}\left(\mu\mathrm{m}\right)}{233\,T_e\left(\mathrm{keV}\right)}, \qquad (3)$$

where $I_{n_c/4}$, $L_{n_c/4}$, and T_e are the intensity, density scale length, and electron temperature at the quarter-critical surface, respectively. As mentioned earlier, NIF implosions are characterized by higher coronal temperatures; however, the scale length is also larger—350 μm in the current experiments compared to 150 μm in OMEGA implosions. Note that since the target sizes in the ongoing experiments are determined by the phase plates on the NIF, the scale lengths are smaller than those in ignition-relevant designs (~500 to 600 μm). The extrapolation to longer scale lengths suggests that a larger source of hot electrons is expected on the NIF; however, beam polarizations and beam angles also influence the extent of this instability. One significant difference between OMEGA and NIF experiments is that the ongoing NIF implosions are performed in the polar-direct-drive (PDD) geometry.[14] Beams displaced toward the equator to improve symmetry are incident at oblique angles onto the target. More beams are overlapped in the NIF geometry than on OMEGA but with variations in the beam polarizations and incident angles. These differences motivate experiments on the NIF to estimate the TPD source and its effect on the imploding capsule.

This work presents results from implosion experiments on the NIF. While a subset of results presented in this work has appeared previously,[15] a more-complete analysis that includes the validation of the CBET model in OMEGA PDD implosions, comparison of scattered-light spectra, and time histories with updated simulations that include a first-principles equation of state (FPEOS)[5] is presented here. Also included is a discussion on the reasons for possible differences between simulation and experiment.

This article discusses (1) the target design and (2) results from the experiments, organized by the physics topics—energetics and preheat. Simulated scattered-light spectra show similar trends as observed; trajectories from backlit images and the shapes of the imploding core agree very well, although the trajectory from self-emission images lags the simulation in the experiment. These results and sensitivity analyses to possible errors in CBET modeling, the effect of laser imprint, and fast-electron preheat are examined and future work and conclusions are presented.

NIF Target Design

The primary target type considered in this article has an outer radius of ~1100 μm with an ~100-μm-thick, all-plastic (CH) shell filled with 20 atm of deuterium (D_2) gas [Fig. 145.1(a)]. The capsule is irradiated with a laser pulse shape whose temporal history includes a flat foot rising to a main pulse at varying laser intensities.[16,17] The shock launched

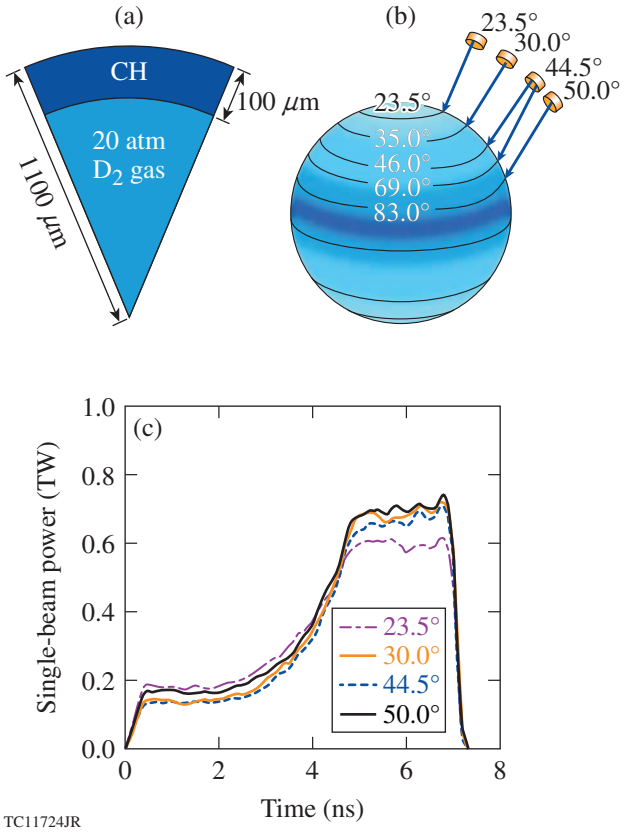

Figure 145.1
(a) Schematic of the target used in a typical polar-direct-drive (PDD) National Ignition Facility (NIF) implosion. (b) The pointing scheme in polar angle used for the PDD implosions. The four original cones at 23.5°, 30.0°, 44.5°, and 50.0° are repointed to the locations shown on the target. (c) Pulse shapes for each of the cones.

during the foot of the pulse shape sets the implosion at an ignition-relevant adiabat $\alpha_{inn} \sim 3$. The implosions have a low convergence ratio of ~13 (compared to ≳22 for direct-drive ignition), defined as the ratio of the initial radius of the fuel–shell interface to the final fuel radius at peak neutron production. The laser energy on target varies from ~350 kJ (for a pulse shape with an intensity of $\sim 4 \times 10^{14}$ W/cm^2 at the initial target radius) to ~650 kJ (corresponding to an on-target intensity of $\sim 1.2 \times 10^{15}$ W/cm^2). The pulse shapes are similar although they differ in the duration of the main pulse. The shell is deliberately set at a low implosion velocity of 1.8 to 2.2×10^7 cm/s, compared to ignition-relevant values of $\gtrsim 3.5 \times 10^7$ cm/s. The low velocity reduces the instability growth of the most-dangerous modes, which scale linearly with the implosion velocity.[18] This conservative design was chosen because the growth of single-beam nonuniformity (laser imprint) is expected to significantly compromise shell integrity in these implosions (also discussed in **Future Work**, p. 12); the existing laser-beam smoothing is insufficient to drive high-performing implosions. Beam profiles used in the x-ray drive ignition campaigns[19] are used in the design. The on-target beam profile is calculated by forward propagating the near-field phase-front information using the code *Waasikwa*'.[20] The laser beams are also defocused by 1 cm to improve symmetry, which is taken into account in the calculation. Since only one set of near-field beam phase-front information is available for each cone, the same calculated profiles are used for all of the beams within a cone.

The beam geometry on the NIF is configured for the axi-symmetric x-ray-drive configuration [Fig. 145.1(b)]. To improve irradiation symmetry, the equator requires additional drive. This is achieved by displacing the beams toward the equator as illustrated in Fig. 145.1(b). The beams on the NIF are arranged in cones at 23.5°, 30°, 44.5°, and 50°. In this PDD geometry, for example, the outer cone located at 50° is displaced to irradiate the target at 83°. The beam configuration in Fig. 145.1(b) is obtained by iteratively adjusting the combination of beam displacements, beam defocus, and beam pulse shapes to reduce shell asymmetry.[16] In addition, beams in cones 44.5° and 50° are displaced azimuthally to improve symmetry. Typical laser pulse shapes for the different cones are shown in Fig. 145.1(c). Notice that the 50° cone is driven with the highest power to provide additional drive in that region. The PDD configuration differs from the spherical-direct-drive (SDD) implosion studies on OMEGA,[16,21] where models have been validated. The lack of drive at the equator is deliberately compensated by displacing beams toward the equator. These beams displaced toward the equator scatter around the target and, consequently, more scattered light appears near the poles in PDD than SDD. SDD is quasi-symmetric; simulations indicate that the scattered light around the target chamber varies by less than 1% rms (root mean square), significantly smaller than PDD. CBET, in particular, is influenced by the PDD beam displacements. More ray crossings occur over a region around the equator; therefore, CBET influences the laser-energy deposition in the region over the equator. As the schematic in Fig. 145.2(a) indicates, an outgoing ray (probe) from the southern hemisphere near the equator acquires energy from an incoming ray (pump) in the northern hemisphere; this excess energy in the outgoing ray can appear as scattered light over the northern polar region. This is also shown in Fig. 145.2(b) in the contour plot of the CBET energy gained per unit volume and normalized to the hydrodynamic time step. The contour plot shows the region where CBET dominates. Most of the energy gain in the rays occurs away from the poles and in a range of polar angles closer to the equator. The projected scattered light around the target chamber is shown in Fig. 145.3 for an OMEGA PDD implosion. The hydrodynamic code *DRACO* with a full three-dimensional

(3-D) ray trace[22] that includes collisional absorption, nonlocal heat conduction,[23] and FPEOS[5] is used to simulate the PDD implosion. When the effect of CBET is included in the calculation [Fig. 145.3(b)], significantly more scattered light appears near the poles than when only collisional absorption is used to model the laser-energy deposition [Fig. 145.3(a)]. Scattered-light flux around the target chamber as a function of polar angle, collected using calorimeters in a PDD implosion irradiated with a pulse shape similar to one used in NIF implosions,[24] is shown in Fig. 145.3(c). The locations of the calorimeters are shown as

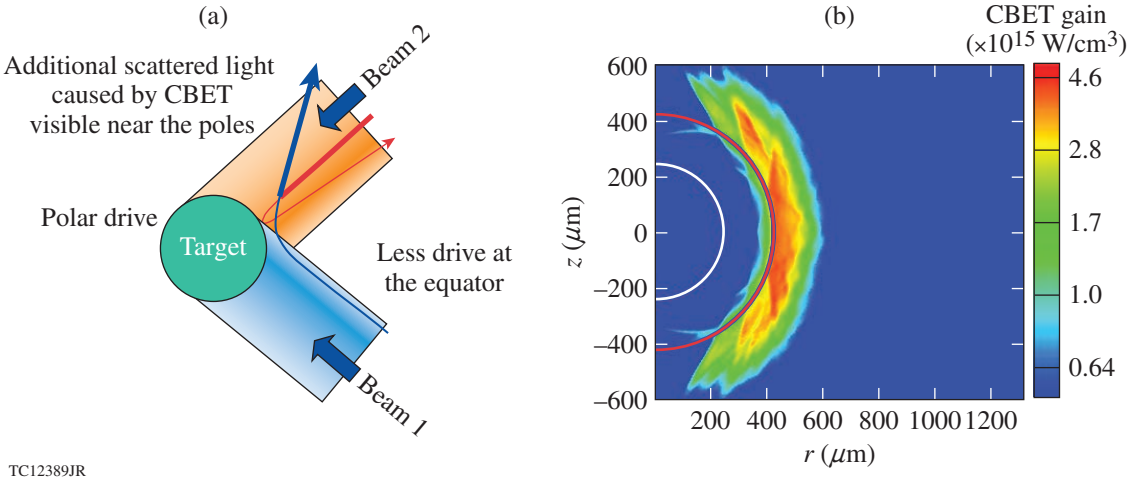

Figure 145.2
(a) Schematic of cross-beam energy transfer (CBET) in the PDD geometry. The dominant transfer occurs when energy is transferred from an incoming ray to an outgoing ray. (b) Contour plot of energy gained from CBET. The transfer occurs away from the poles; more ray intersections occur away from the poles because of PDD beam displacements.

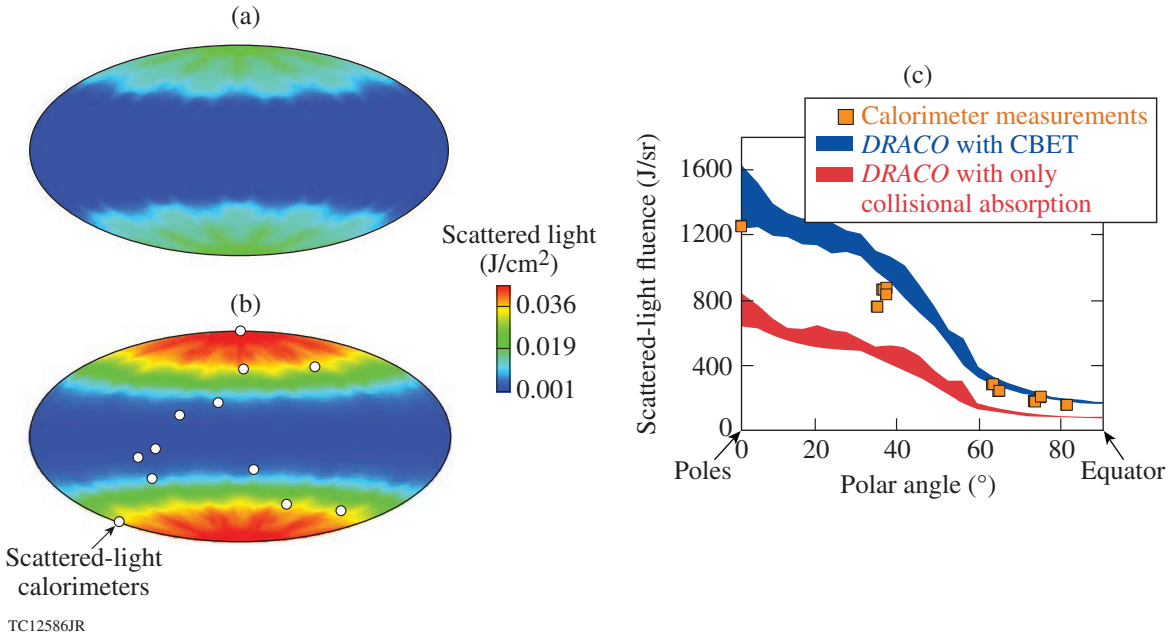

Figure 145.3
Projected scattered light in the OMEGA target chamber from a simulation that includes (a) only the effect of collisional absorption and (b) the effect of CBET. Circles indicate the locations of the calorimeters in the OMEGA chamber. (c) Scattered-light fluence at the calorimeters in shot 64099 on OMEGA (symbols). The simulation is shown as shaded regions, indicating the minimum and maximum scattered light along the azimuthal angle. Red corresponds to (a)—only the effect of collisional absorption is included. Blue corresponds to (b)—the effect of CBET is also included in the simulation.

circles on Fig. 145.3(b). As the figure indicates, significantly more scattered light appears near the poles when CBET is included in the calculation (blue) compared to when only collisional absorption is included (red). The shaded regions indicate the minimum and maximum light along the azimuth as calculated by the 3-D ray trace. The additional polar light agrees well with observations (symbols), which also show the same trend.

Simulations indicate that the energy transfer from the incoming rays occurs at the center of the beam for rays with the smallest incident angles that are the most hydrodynamically efficient. This results in less drive around the equatorial region; therefore, CBET makes the implosion more oblate than collisional only absorption as seen by the synthetic self-emission images of the imploding shell (Fig. 145.4). Requiring simulations to reproduce the observed shape of the imploding core, i.e., the drive as a function of polar angle, makes PDD a more-stringent test of direct-drive implosion physics than SDD.

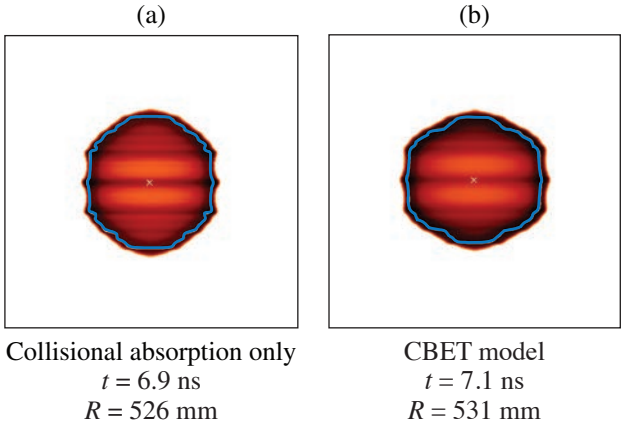

Figure 145.4
Simulated self-emission images from N150118-002 with (a) only collisional absorption laser deposition included in the calculation and (b) the effect of CBET also included in the calculation.

Results and Discussion

1. Energetics

a. Results. Energetics on the NIF is inferred from time-resolved scattered light measured using fast diodes[25] and a streak camera.[25] The time-resolved scattered light is plotted in Fig 145.5. The simulation tracks the observations very closely with deviations between 5 and 7 ns. The implication of the excess simulated scattering is unclear. Additional information is also available from the two full-aperture backscatter stations (FABS)[25] that measure the spectrum of scattered light. Figure 145.6(a) shows the spectra observed by the FABS. Features characteristic of implosions are observed in the spectra:

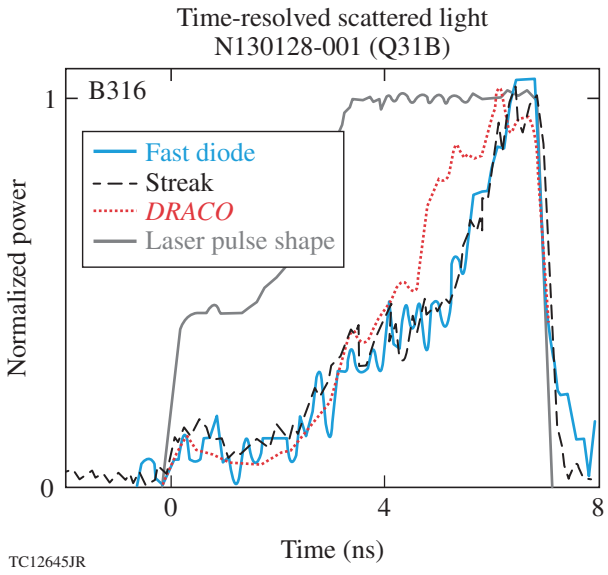

Figure 145.5
Time-resolved scattered light measured at one location, corresponding to B316, from fast diodes (blue solid line) and optical streak cameras (black dashed and solid lines). Time-resolved scattered light from a simulation including the effect of CBET is also shown (red dotted line).

a rapid blue shift is observed early in time corresponding to corona formation; the red shift at ~2 ns corresponds to the onset of inward motion of the corona during the acceleration phase. Very similar trends are observed in the *DRACO* simulation [Fig. 145.6(b)]. Similar agreement is obtained with the spectra from the other FABS location. Quantitative inferences of the energy in the scattered-light spectrum and the time-resolved light are in progress and are important to further validate the modeling (discussed in the next section).

Trajectories of the converging shell provide information about the laser energy coupled to the target and are measured in two ways: the first uses a gated framing cameras with a 1-mil-thick Be filter (~25 μm) to measure the self-emission of the target,[26] corresponding to photon energies ≳1 keV; the second uses a gated framing camera to measure a radiograph obtained by backlighting an implosion[27] using Fe (~6.7 keV). Excellent agreement is obtained with the CBET model on OMEGA to replicate observed trajectories from self-emission images,[21] while trajectories from backlit images have been explored to a more-limited extent.[27] The design for a backlit implosion requires changes to the beam configuration. Two quads (one from each hemisphere) are removed to irradiate an iron backlighter. The energies of eight neighboring quads and their pointing are adjusted to improve symmetry. Figure 145.7 shows typical images obtained from the framing cameras. The view from the pole records the self-emission. Simulations show that the location of the steepest

gradient corresponds closely to the ablation surface.[26] This location is shown on a typical simulated density profile of the implosion. Notice the circular polar image indicating that the nonuniformity imposed by the removal of quads to irradiate the backlighter has been adequately compensated by the increased energies and repointing of the eight neighboring quads. The view from the equator records the backlit image. The surface of greatest absorption corresponds to the location of the fuel–shell interface, as shown on the same density profile; therefore, the difference in the location of the two surfaces can be interpreted as the thickness of the imploding shell.

Trajectories for different shots are plotted in Fig. 145.8. Simulations are post-processed using the code *Spect3D*[28] to create the self-emission and backlit images. The finite spatial resolution (~20- to 30-μm pinhole size depending on the shot) and gating time window of the cameras (~100 ps) are included in the simulated images. The same analysis is used to extract average radii from the synthetic and measured images.[26,27] The black solid line from the backlit image reproduces the inferred trajectory very well, whereas the red dashed line from self-emission images apparently overestimates the drive. The slopes of the two trajectories indicate that the velocity from the backlit trajectory

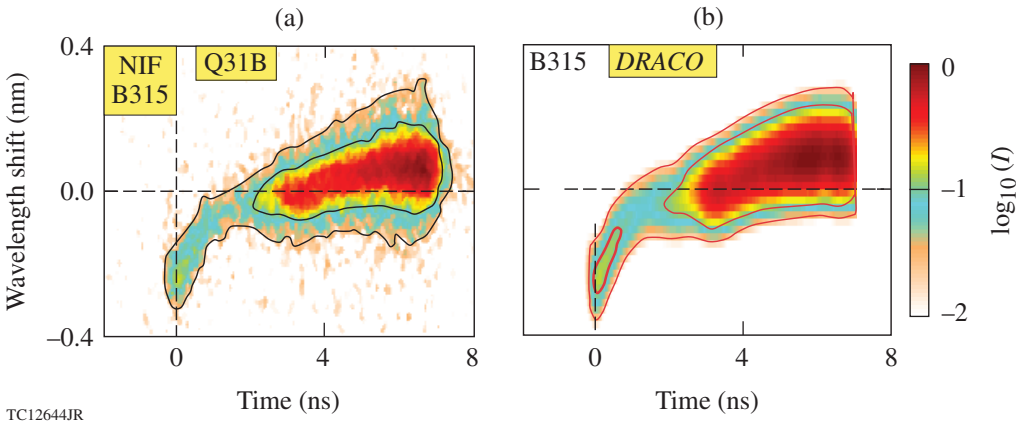

Figure 145.6
Scattered-light spectrum measured using the full-aperture backscatter station (FABS) diagnostic at one location and corresponding to the same location as the diodes. (a) Measured scattered-light spectrum and (b) spectrum from a simulation including the effect of CBET.

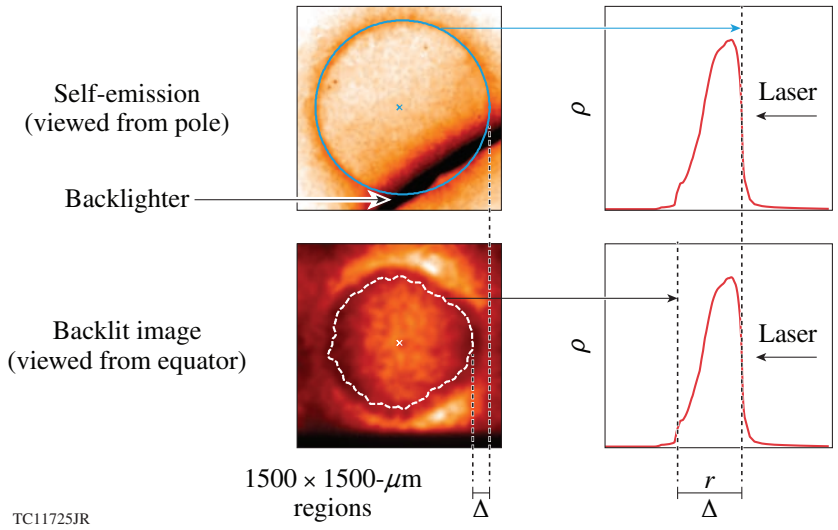

Figure 145.7
Typical self-emission image viewed from the pole and backlit image viewed from the equator (shot N140612-001). Absorption images are obtained at 6.7 keV by backlighting the implosion with Fe. Self-emission images are viewed at ≳1 keV with a Be filter of 1-mil thickness. The lineouts point to the surfaces in the density profile (right) that are extracted from the image.

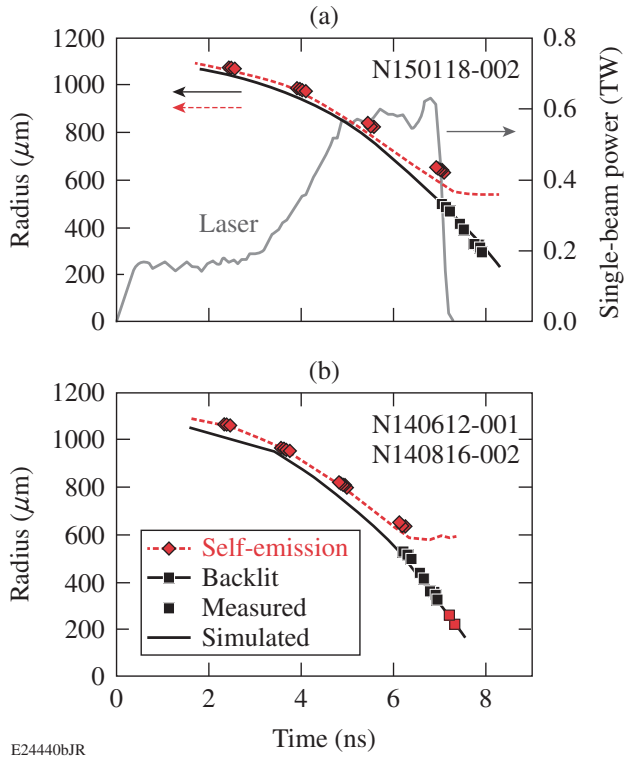

Figure 145.8
(a) Trajectories from backlit images from measurements (black squares) and simulations (black solid line). Trajectories from self-emission images from measurements (diamonds) and simulations (red dashed line) for shot N150118-002. (b) Same as (a) but for shots N140612-001 and N140816-002.

is reproduced to within 1% by the simulation, whereas the trajectory from the self-emission images is overestimated by ~9%. If the self-emission trajectory was representative of the velocity, this would significantly increase E_{min}, compromising ignition. It is, therefore, important to resolve the difference and identify which trajectory, if either, is representative of the true implosion velocity. Note that the inferred shell thickness estimated using the procedure in Fig. 145.7 is larger than the simulated value. The trajectories and shell thickness can be influenced by both 1-D and multidimensonal physics. One-dimensional physics energy includes coupling models and preheat (radiative or fast electron). Multidimensional physics such as Rayleigh–Taylor growth seeded by imprint can also change the location of peak emission or absorption of x rays. It is important to understand if the differences are caused by errors in the 1-D modeling since they influence models used to predict ignition. If imprint was the cause, it is expected to be of less concern since improved beam smoothing[29] and target designs with doped-CH overcoats[30] or Au layers[31] have been shown to mitigate this effect. Each of these factors is discussed below—first qualitatively and then collated in a plot showing the relative magnitude of each of these effects.

b. Sensitivity analysis. Overestimating the predicted velocity of the early shock (resulting from inaccuracies in the modeling of laser coupling or equation of state) can delay the trajectory. If the shock was slower than simulated, the breakout of the shock into the gas would be delayed, postponing the onset of acceleration. Shock mistiming can thicken the converging shell: a higher adiabat results in a lower-density shell that occupies a larger volume during convergence. However, for this pulse shape, the absorption during the low-intensity foot is very high (~95%). The mechanism for absorption during this time is primarily collisional absorption; so any mistiming of the shock is small and its effect on shell thickness and trajectory is insignificant. For example, mistiming the shock during the foot by using a flux-limited diffusive heat-conduction model with flux limiter $f = 0.06$ (Ref. 32) instead of the nonlocal transport delays the shock breakout by less than 20 ps, which only marginally influences trajectory and shell thickness. Therefore, it is hypothesized that the observations cannot be explained by shock mistiming alone.

Sensitivity analysis to the CBET model is examined using the spherically symmetric code *LILAC* by using a multiplier, $f_{CBET} = 2$, in the gain factor [Eq. (2)]. Figure 145.9 shows the density profiles in the simulation of a NIF-type implosion at different times when the inner surface of the shell has traveled the same distance. The shell becomes increasingly decompressed and the ablation pressure is reduced as the extent of CBET is increased in the modeling (Table 145.I). This also significantly reduces the absorption fraction, suggesting that

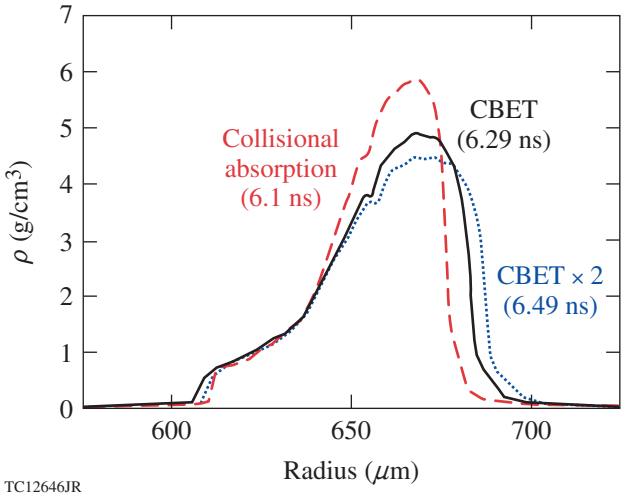

Figure 145.9
Density profiles showing the sensitivity of the shell thickness to different extents of CBET (red dashed line: collisional absorption only; black solid line: CBET with $f_{CBET} = 1$; blue dotted line: CBET × 2 with $f_{CBET} = 2$).

a detailed quantification of the scattered light is crucial to achieve higher accuracy in the laser-deposition CBET modeling. The implosion velocity, which decreases as the extent of CBET increases in the model, is listed in Table 145.I. This is also shown in Fig. 145.10 through the trajectories of the two surfaces; CBET reduces the velocity of both the surfaces while decompressing the shell. Agreement with the experimentally inferred trajectories requires that the backlit trajectory remains unchanged, whereas the self-emission trajectory becomes apparently slower; therefore, an error in the CBET modeling alone is insufficient to explain the observation.

Preheat from energetic "hot" electrons can also potentially influence the trajectories. The energy in hot electrons is inferred in NIF implosions from the filter-fluorescence x-ray (FFLEX)[33] diagnostic. FFLEX measures the time-resolved x-ray emission in ten channels ranging from ~20 keV to 250 keV. The inferred total cumulative energy E_{hot} is calculated assuming that the entire observed x-ray emission results from the deposition of the fast-electron energy in the CH ablator. A value of $E_{hot} \sim 2.5 \pm 0.3$ kJ is, therefore, obtained corresponding to ~0.4% of the total laser energy. The hot-electron temperature is inferred by fitting the measured time-integrated x-ray spectrum for the various FFLEX channels. The fit yields a value of 46±3 keV for the shots considered here.[15] This is consistent with temperature measurements on OMEGA.[34] A straight-line deposition formula is used in *LILAC* to simulate the effect of this distribution of electrons on the trajectory and shell thickness.[35] A wide angular divergence of the electrons (240°) is assumed in the model. Studies of TPD in SDD OMEGA implosions using Mo balls of different radii suggest that the electrons are produced at a large divergence angle.[34] Indications of isotropy were also observed in NIF PDD implosions in the DIME[36] (defect-induced mix experiment) campaign.[35] Energetic x rays produced in the DIME NIF PDD implosions are observed via pinhole images and are also isotropic.[37] Therefore, a straight model in the spherically symmetric code *LILAC* is expected to reproduce the sensitivity of the NIF implosion to fast-electron preheat. The observed time-resolved history of the x-ray emission (Fig. 13 in Ref. 15) is calculated by the model—almost no emission is observed until ~4 ns.

Table 145.I: The effect of selected implosion parameters with increasing extents of CBET using the spherically symmetric code *LILAC*. CBET × 2 corresponds to $f_{CBET} = 2$ in Eq. (2). The numbers in parentheses indicate the values (in %) of the quantity relative to the collisional absorption value.

Model	P_{abl} (Mbar)	M_{abl} ($\times 10^6$ cm/s)	V_{imp} ($\times 10^7$ cm/s)	f_{abs}(%)
Collisional absorption	70	1.4	2.2	95
CBET	30 (43%)	0.8 (57%)	1.8 (82%)	75 (79%)
CBET × 2	15 (21%)	0.6 (43%)	1.5 (68%)	64 (67%)

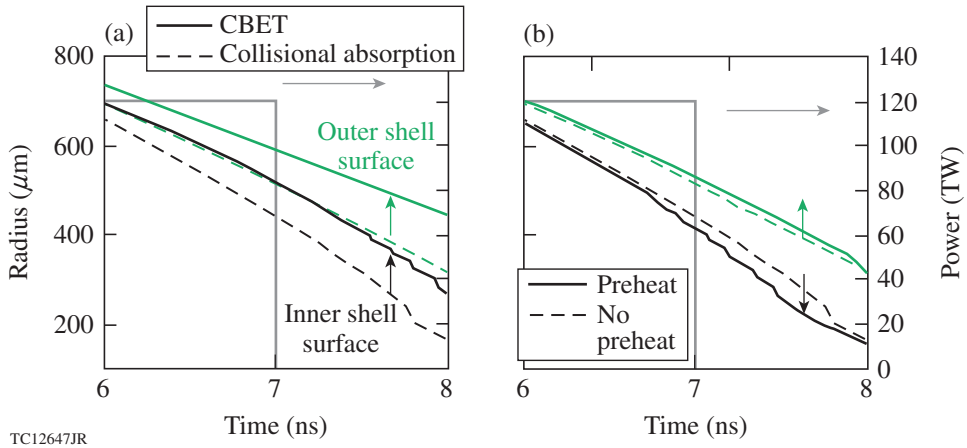

Figure 145.10
Dependence of the backlit and self-emission trajectory to models with (a) collisional absorption only (dashed lines), including the effect of CBET (solid lines) and (b) collisional absorption only (dashed line), including the effect of preheat (solid line). The laser pulse, corresponding to the right axis, is shown for reference.

The emission then increases during the main pulse and stops at approximately the end of the laser pulse. The effect of these electrons on the implosion is shown in Fig. 145.10. A factor of ~2 more electron energy (4.6 kJ) than experimentally inferred is required in the simulation to make the effect more visible on the plot. Preheat increases the shell thickness and decreases the slope of the self-emission trajectory as required to match the observations; however, note that it also increases the slope of the backlit trajectory contrary to what is required to match the observations. The significantly larger magnitude of the preheat source required to observably change trajectories and shell thickness suggests that preheat alone is not likely the cause of the observed discrepancies between simulation and measurements. A comparison of the simulated and inferred self-emission trajectory from a low-intensity shot (~4×10^{14} W/cm^2 at the initial target radius) also indicates the apparent slowing down of the self-emission trajectory (Fig. 145.11). At this intensity, the energy in fast electrons is estimated to be less than 0.05% of the laser energy at the noise level of the FFLEX instrument—a value that has an insignificant effect on the implosion. This also suggests that fast-electron preheat is less likely a cause for the apparent shell decompression. Fast-electron preheat can be conclusively ruled out only if the backlit trajectory is also well reproduced at the low intensity and the trend in the discrepancy at the two different intensities stays the same. This is being investigated with a low-intensity implosion where a backlit trajectory is also available.

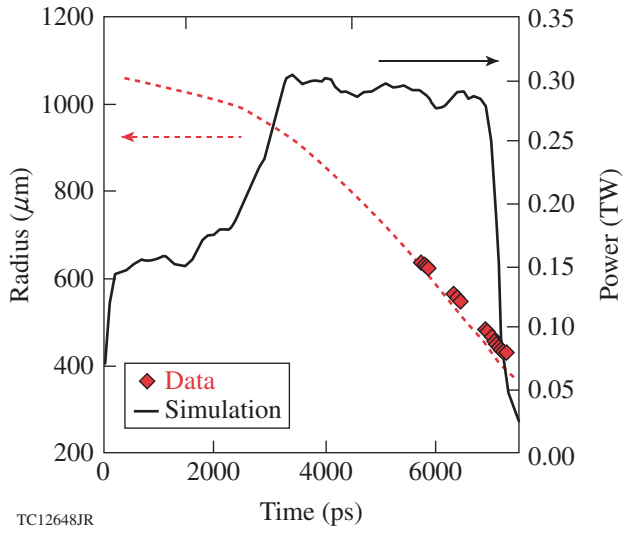

Figure 145.11
Trajectories from a low-intensity implosion (~4×10^{14} W/cm^2 average on-target intensity at the initial target radius), N130128-001. Only the self-emission trajectory is measured for this shot (red diamonds). The simulated trajectory, including the effect of CBET, is shown as the black solid line.

Finally, multidimensional effects are discussed. Single-beam laser nonuniformity imposes perturbations on the target starting at short wavelengths corresponding to ~10 μm ($\ell \sim$ 600 at the initial target radius).[9] The effect of laser imprint and the subsequent RT growth is modeled using *DRACO*. Density contours at the end of the acceleration phase for a NIF implosion are shown in Fig. 145.12(a). To make the simulation tractable, only modes up to $\ell \sim 200$ are included in the calculation. The shell is significantly distorted with a relatively intact inner shell. Trajectories from simulated images [Fig. 145.12(b)] indicate that the backlit trajectory is unchanged relative to a simulation with no distortions, whereas the self-emission region moves

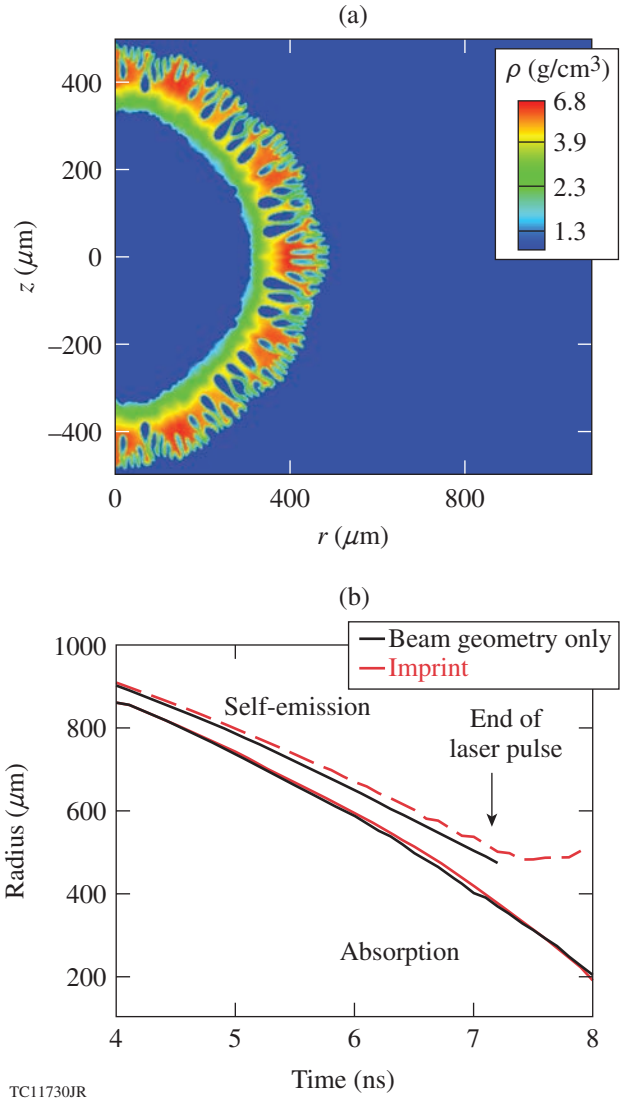

Figure 145.12
The effect of single-beam nonuniformity (laser imprint) is shown as (a) density contours at the end of the acceleration phase and (b) trajectories extracted from post-processed synthetic images of the simulation shown in (a).

farther outward, leading to an apparent decompression of the shell. This trend is consistent with experiments. A larger-scale simulation including modes up to $\ell \leq 600$ is being performed to study the influence of shorter wavelengths on the trajectory and shell thickness. Of the three sources of modeling uncertainty considered so far, only laser imprint shows the correct trends of keeping the backlit trajectory relatively unchanged and causing an apparent slowing down of the self-emission trajectory.

The results from these sensitivity studies are summarized in Fig. 145.13. The percentage increase in shell thickness over the nominal implosion (defined as including CBET, nonlocal transport, and FPEOS) is plotted against the percentage of preheat energy in the fast-electron source. To explore the sensitivity to angular divergence, electrons are launched isotropically and with an angular divergence of 240°. Shell thickness increases slowly with increasing preheat. The observed shell thickness, shown for two shots, is significantly higher than the increase caused by preheat, indicating that preheat alone is insufficient to explain the observed thickness. The increase in thickness from $f_{\text{CBET}} = 2$ is also shown in Fig. 145.13. The relatively small change in shell thickness resulting from any possible error in the CBET model also suggests that energetics are well modeled and is not likely the cause for the observed differences. The increase in shell thickness caused by imprint is shown in Fig. 145.13. Of all the sources considered, imprint is the dominant contributor to the increase in shell thickness. Imprint also leaves the backlit trajectory unchanged, which is required for consistency with the measurements. It is hypothesized that some combination of the various sources of error and imprint will explain the observations with imprint as the dominant source.

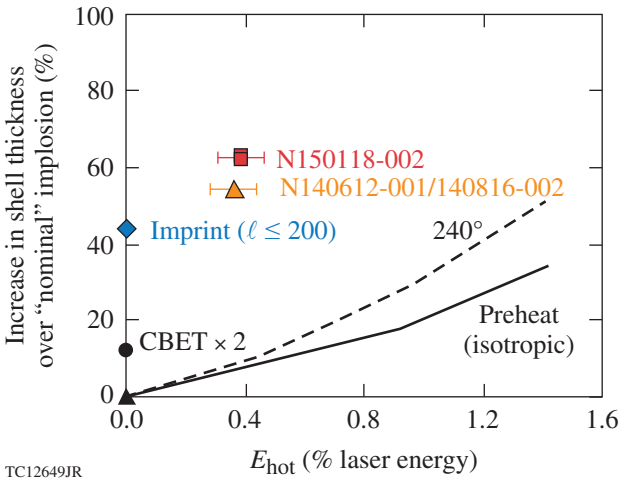

Figure 145.13
Increase in shell thickness (in %) over the nominal implosion defined as one including the effects of CBET, FPEOS, and nonlocal transport. The symbols with error bars correspond to measured values from framing-camera images. The dashed and solid lines correspond to the simulated effect of preheat. The circle indicates the effect of $f_{\text{CBET}} = 2$ in the CBET model. The diamond indicates the effect of imprint.

A further indication that the laser drive is well modeled is obtained from the shape of the imploding core. Simulated and observed backlit images are shown in Fig. 145.14 for approximately the same convergence. Note that the shapes are far from round. This is a limitation of the available beam profiles on the NIF. Significantly improved implosions can be obtained with custom beam profiles.[38] The observed shape is very well reproduced by simulations. This is quantified by the radial deviation about the mean radius in Fig. 145.14(c), where the observed and simulated lineouts of the radial deviation are overlaid. Excellent agreement is obtained, suggesting that energetics is well modeled. Small deviations are observed near the pole. This difference is also observed on a lower-

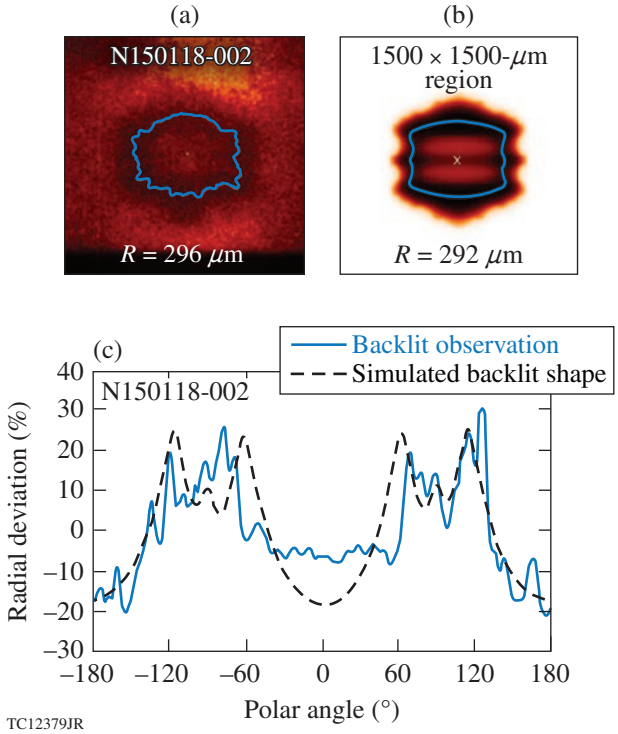

Figure 145.14
(a) Measured backlit image using the Fe line at 6.7 keV. The blue line indicates the surface of maximum absorption. (b) Simulated backlit image. The line shows the surface of maximum absorption. (c) Lineout in polar angle of the radial deviation about the mean at approximately the same convergence for measurements (solid) and simulations (dashed) for shot N150118-002.

intensity shot (Fig. 145.15). The measured and simulated images at the low intensity show reasonable agreement in the shape [Figs. 145.15(a) and 145.15(b)]. The deviation of the lineout about the average radius versus polar angle is shown in Fig. 145.15(c). The gross shape is well reproduced, although the polar region is driven significantly more in the simulation compared to experiment. Since this difference is systematic between two shots, a plausible reason for this difference could be incomplete knowledge of the calculated defocused beam profiles. No measurements of these profiles are available at this time. Moreover, as mentioned earlier, while different beam profiles are calculated for each cone, the same profile is used for all of the beams within the cone. Beam-to-beam variations are not included in the calculation since this information is unavailable.

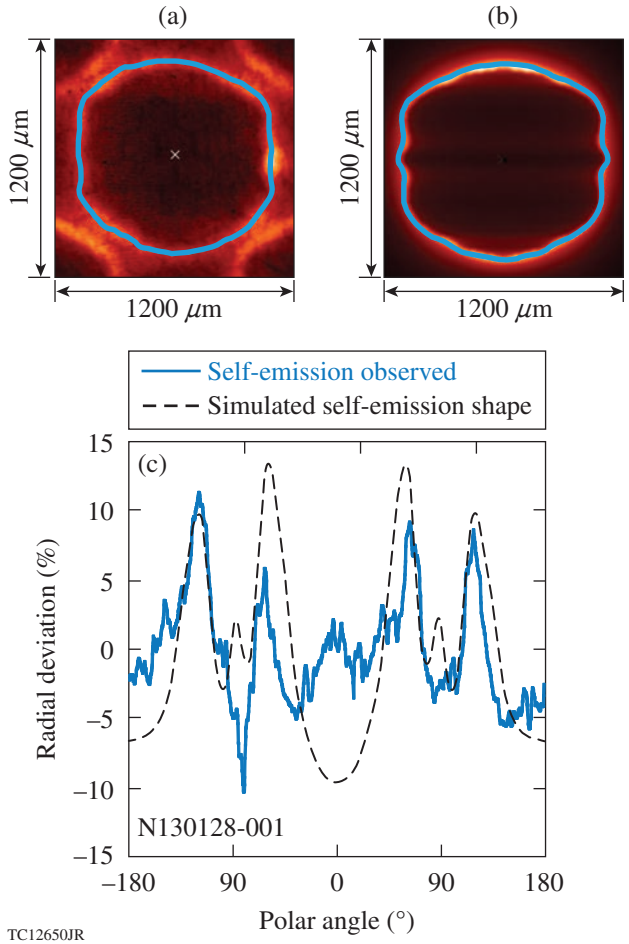

Figure 145.15
(a) Measured self-emission image. The blue line indicates the surface of steepest gradient of emission. (b) Simulated image. The blue line shows the surface of maximum absorption. (c) Lineout in polar angle of the radial deviation about the mean at approximately the same convergence for measurements (blue solid line) and simulations (black dashed line) for shot N130128-001.

c. Preheat. Estimates from FFLEX measurements in NIF implosions indicate that ~0.4% of the laser energy is converted into electron energy at intensities of 8×10^{14} W/cm^2 (the lowest ignition-relevant intensity).[15] Preheat results inferred from FFLEX for shots with varying intensity are summarized in Fig. 145.16. In integrated implosion experiments, typically only the preheat source is inferred from the measurement of bremsstrahlung x rays emitted by the fast electrons. The energy deposited in the cold shell, which is the relevant quantity for designs, is usually calculated using models[35] or estimated from complementary experiments.[39] It has been shown previously from semi-analytic estimates that ignition fails if ≥1.5% of the shell's kinetic energy is deposited as the preheat energy into the shell.[40] A typical ignition design at 1.5 MJ of laser energy, with ~80 kJ of the shell's kinetic energy, can tolerate a maximum of 1.2 kJ or 0.08% of the laser energy deposited in the cold shell without significantly compromising ignition. A similar fraction of ≲1% of the laser energy deposited in the cold shell has been previously obtained from *LILAC* simulations.[41]

The deposited energy in experiments described in this work is estimated using OMEGA implosions. A combination of room-temperature and cryogenic implosions of equivalent mass has been used to infer the energy deposited in the cold shell.[39] This work estimates that ~1/7th of the electron source energy is deposited in the high-density shell. The same ratio is applied to the NIF implosions; the same energy estimated from FFLEX is

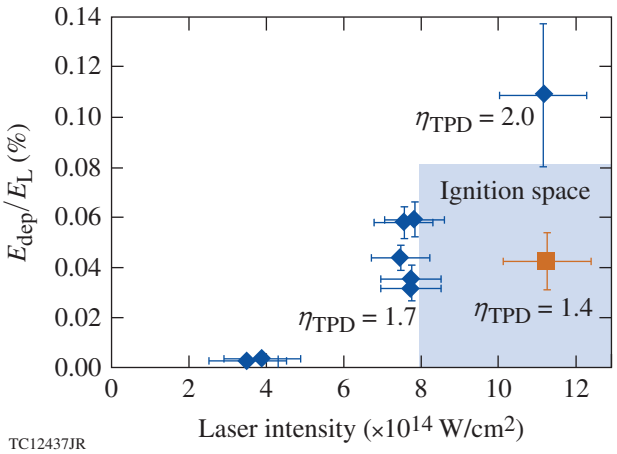

Figure 145.16
Estimated deposited energy from energetic electrons from two-plasmon decay (TPD) as a fraction of the total laser energy versus the polar-angle–averaged, on-target laser intensity during the peak of the laser pulse (measured at the initial target radius) for CH ablators (diamonds) and a target with an outer Si layer (square). The shaded region shows the range of acceptable preheat from fast electrons.

multiplied by this ratio to obtain the hot-electron energy deposited in the shell. Figure 145.16 shows this energy as a fraction of the total laser energy plotted against the on-target intensity (calculated at the initial target radius). The shaded region in the figure shows the acceptable range of intensity and deposited energy based on the analysis presented above. The preheat scales with the calculated values for the threshold parameter, η_{TPD}, consistent with OMEGA implosions. The figure shows that preheat for CH ablators is tolerable at intensities closer to 8×10^{14} W/cm^2, whereas it is clearly at an unacceptable value for ignition at higher intensities. Simulations indicate that with full CBET mitigation, η_{TPD} will increase by nearly 60% to 2.6, possibly resulting in preheat closer to the value at the higher intensity of 1.2×10^{14} W/cm^2. This would result in failure of ignition.

The presence of a mid-*Z* layer such as Si at the quarter-critical surface during the time of TPD production (the latter part of the main pulse) (Fig. 13 in Ref. 15) has been shown to reduce the preheat source in OMEGA implosions.[42] The reduction in the preheat source is primarily from the higher temperature in the corona because of the high atomic number of Si. A similar NIF experiment with an outer 14 μm of Si overlaid on a CH layer is also shown in Fig. 145.16. In this design, Si is present in the quarter-critical surface throughout the implosion. This clearly reduces the shell preheat to tolerable levels. A similar implosion will be repeated after CBET mitigation to study mitigation of fast-electron preheat.

Future Work

Future work related to NIF experiments will focus on continued model validation. As mentioned earlier, quantification of scattered light is important to disentangle the various effects discussed above and could potentially explain the discrepancy in the self-emission trajectories. Further validation requires larger-scale imprint simulations to isolate the effect of imprint. Measurements of imprint in cone-in-shell geometry[43] will be performed over the next year on the NIF. These experiments will also serve as platforms for future studies of imprint and its mitigation when improved beam smoothing[29] is installed on the NIF. As Table 145.I shows, CBET decreases the mass ablation rate and implosion velocity. Mitigation of CBET is important to recover robust ignition designs. As Eq. (2) shows, detuning the wavelengths of the pump and probe beams will detune the resonance and reduce the volume over which CBET can occur, reducing the magnitude of the effect. This will be studied using the available tunable wavelength capability of the NIF: a maximum of ±2.3 Å in the UV.[44] This value is smaller than what is required to recover more than 50% of the CBET energy lost in simulations (≳6 Å in the UV).[44] Simulations predict, however, that differences in the shape, trajectory, and the magnitude of scattered light should be observable in the experiment.[44] Other means to improve mass ablation rates such as Be ablators[45] will be explored in the coming year. Finally, TPD mitigation will be studied with a mid-*Z* layer such as Si after CBET has been mitigated.

The longer-term pre-ignition goal on the NIF is to implode a multilayer target such as the one described in Ref. 21. A mass-equivalent CH layer will replace the cryogenic DT layer in the room-temperature equivalent of the cryogenic target described in Ref. 21. A multilayer target will permit imprint mitigation (through the use of doped ablators such as CHSi or Au layers), the reduction of TPD through the use of a thin Si layer that would be present at the quarter-critical surface only during the latter part of the main pulse (where TPD is evident from fast electrons), and a Be layer to provide an improved mass ablation rate. A high-convergence implosion is not expected from this design since the outer layers of Si radiatively preheat the inner CH layer. This effect is small when a DT layer is used instead of the inner CH layer because of its low opacity. High-convergence direct-drive NIF implosions with CBET and TPD mitigation are possible only in cryogenic DT layered targets.

Ignition attempts require additional investments in hardware on the NIF including improved beam smoothing,[29] custom phase plates,[38] cryogenic target layering, delivery systems, etc. At this time, it is unclear if such an attempt would involve SDD or PDD. A future study will explore the facility and mission impacts of moving some of the NIF beams to enable spherical illumination. The NIF target chamber has ports for such beam placement. The results presented in this work apply to either scheme. Estimating imprint and the effect of laser–plasma interactions at long scale lengths on implosions and their mitigation is a critical component of studying the viability of direct drive as an ignition option.

Conclusions

Results from NIF PDD implosion experiments have been presented. The goal is to test the modeling of energetics and measure the extent of preheat in NIF implosions that have longer coronal density scale lengths than comparable implosions at the Omega Laser Facility. Observables such as the shape of the scattered-light spectrum, time-resolved scattered light, trajectories from backlit images, and the shape of the imploding shell agree very well with simulations. However, the trajectory from self-emission images lags simulations, suggesting a slower trajectory from self-

emission or a thicker shell than simulated. While the cause for this discrepancy is unknown, sensitivity analyses for the various effects that might result in an effectively decompressed shell indicate that errors in energetics modeling, such as those in the CBET model, are likely not the cause. Laser imprint and subsequent Rayleigh–Taylor growth appear to be the dominant source of the observed difference. The CBET model that best reproduces the observations requires the same overall multiplier to the gain factor for both OMEGA and NIF simulations. It is expected that quantifying the scattered light on the NIF will help to identify, if this is indeed the case, and further test model predictability. The fast-electron preheat source in ongoing implosions is at a tolerable level (~0.4% of laser energy at an ignition-relevant intensity of 8×10^{14} W/cm^2 at the initial target radius) corresponding to ~0.06% of the energy deposited in the cold shell. While this is believed to be tolerable for ignition, it is expected that with the mitigation of CBET, the preheat source will increase, leading to more energy deposited in the cold shell. Implosions with mid-Z layers have been shown to reduce the preheat source (by nearly a factor of 3). Future pre-ignition plans on the NIF include continued validation of models through measurements of imprint and mitigation of CBET and TPD. All of these mitigation strategies will be studied in an integrated room-temperature implosion involving a target with multiple layers.

ACKNOWLEDGMENT

This material is based upon work supported by the Department of Energy National Nuclear Security Administration under Award Number DE-NA0001944, the University of Rochester, and the New York State Energy Research and Development Authority. The support of DOE does not constitute an endorsement by DOE of the views expressed in this article.

REFERENCES

1. J. Nuckolls *et al*., Nature **239**, 139 (1972).
2. S. W. Haan *et al*., Phys. Plasmas **18**, 051001 (2011); P. Y. Chang, R. Betti, B. K. Spears, K. S. Anderson, J. Edwards, M. Fatenejad, J. D. Lindl, R. L. McCrory, R. Nora, and D. Shvarts, Phys. Rev. Lett. **104**, 135002 (2010).
3. M. C. Herrmann, M. Tabak, and J. D. Lindl, Nucl. Fusion **41**, 99 (2001).
4. Lord Rayleigh, Proc. London Math Soc. **XIV**, 170 (1883); G. Taylor, Proc. R. Soc. London Ser. A **201**, 192 (1950).
5. S. X. Hu, L. A. Collins, V. N. Goncharov, J. D. Kress, R. L. McCrory, and S. Skupsky, Phys. Rev. E **92**, 043104 (2015).
6. C. J. Randall, J. R. Albritton, and J. J. Thomson, Phys. Fluids **24**, 1474 (1981).
7. I. V. Igumenshchev, W. Seka, D. H. Edgell, D. T. Michel, D. H. Froula, V. N. Goncharov, R. S. Craxton, L. Divol, R. Epstein, R. Follett, J. H. Kelly, T. Z. Kosc, A. V. Maximov, R. L. McCrory, D. D. Meyerhofer, P. Michel, J. F. Myatt, T. C. Sangster, A. Shvydky, S. Skupsky, and C. Stoeckl, Phys. Plasmas **19**, 056314 (2012).
8. J. Delettrez, R. Epstein, M. C. Richardson, P. A. Jaanimagi, and B. L. Henke, Phys. Rev. A **36**, 3926 (1987).
9. P. B. Radha, V. N. Goncharov, T. J. B. Collins, J. A. Delettrez, Y. Elbaz, V. Yu. Glebov, R. L. Keck, D. E. Keller, J. P. Knauer, J. A. Marozas, F. J. Marshall, P. W. McKenty, D. D. Meyerhofer, S. P. Regan, T. C. Sangster, D. Shvarts, S. Skupsky, Y. Srebro, R. P. J. Town, and C. Stoeckl, Phys. Plasmas **12**, 032702 (2005).
10. T. R. Boehly, D. L. Brown, R. S. Craxton, R. L. Keck, J. P. Knauer, J. H. Kelly, T. J. Kessler, S. A. Kumpan, S. J. Loucks, S. A. Letzring, F. J. Marshall, R. L. McCrory, S. F. B. Morse, W. Seka, J. M. Soures, and C. P. Verdon, Opt. Commun. **133**, 495 (1997).
11. J. D. Lindl and E. I. Moses, Phys. Plasmas **18**, 050901 (2011).
12. V. N. Goncharov, O. V. Gotchev, E. Vianello, T. R. Boehly, J. P. Knauer, P. W. McKenty, P. B. Radha, S. P. Regan, T. C. Sangster, S. Skupsky, V. A. Smalyuk, R. Betti, R. L. McCrory, D. D. Meyerhofer, and C. Cherfils-Clérouin, Phys. Plasmas **13**, 012702 (2006).
13. A. Simon, R. W. Short, E. A. Williams, and T. Dewandre, Phys. Fluids **26**, 3107 (1983).
14. S. Skupsky, J. A. Marozas, R. S. Craxton, R. Betti, T. J. B. Collins, J. A. Delettrez, V. N. Goncharov, P. W. McKenty, P. B. Radha, T. R. Boehly, J. P. Knauer, F. J. Marshall, D. R. Harding, J. D. Kilkenny, D. D. Meyerhofer, T. C. Sangster, and R. L. McCrory, Phys. Plasmas **11**, 2763 (2004).
15. M. Hohenberger, P. B. Radha, J. F. Myatt, S. LePape, J. A. Marozas, F. J. Marshall, D. T. Michel, S. P. Regan, W. Seka, A. Shvydky, T. C. Sangster, J. W. Bates, R. Betti, T. R. Boehly, M. J. Bonino, D. T. Casey, T. J. B. Collins, R. S. Craxton, J. A. Delettrez, D. H. Edgell, R. Epstein, G. Fiksel, P. Fitzsimmons, J. A. Frenje, D. H. Froula, V. N. Goncharov, D. R. Harding, D. H. Kalantar, M. Karasik, T. J. Kessler, J. D. Kilkenny, J. P. Knauer, C. Kurz, M. Lafon, K. N. LaFortune, B. J. MacGowan, A. J. Mackinnon, A. G. MacPhee, R. L. McCrory, P. W. McKenty, J. F. Meeker, D. D. Meyerhofer, S. R. Nagel, A. Nikroo, S. Obenschain, R. D. Petrasso, J. E. Ralph, H. G. Rinderknecht, M. J. Rosenberg, A. J. Schmitt, R. J. Wallace, J. Weaver, C. Widmayer, S. Skupsky, A. A. Solodov, C. Stoeckl, B. Yaakobi, and J. D. Zuegel, Phys. Plasmas **22**, 056308 (2015).
16. P. B. Radha, J. A. Marozas, F. J. Marshall, A. Shvydky, T. J. B. Collins, V. N. Goncharov, R. L. McCrory, P. W. McKenty, D. D. Meyerhofer, T. C. Sangster, and S. Skupsky, Phys. Plasmas **19**, 082704 (2012).
17. P. B. Radha, C. Stoeckl, V. N. Goncharov, J. A. Delettrez, D. H. Edgell, J. A. Frenje, I. V. Igumenshchev, J. P. Knauer, J. A. Marozas, R. L. McCrory, D. D. Meyerhofer, R. D. Petrasso, S. P. Regan, T. C. Sangster, W. Seka, and S. Skupsky, Phys. Plasmas **18**, 012705 (2011).
18. C. D. Zhou and R. Betti, Phys. Plasmas **14**, 072703 (2007).
19. L Divol, Lawrence Livermore National Laboratory, private communication (2012); D. A. Callahan *et al*., J. Phys.: Conf. Ser. **112**, 022021 (2008).
20. J. A. Marozas, S. P. Regan, J. H. Kelly, D. D. Meyerhofer, W. Seka, and S. Skupsky, J. Opt. Soc. Am. B **19**, 7 (2002).

21. V. N. Goncharov, T. C. Sangster, R. Betti, T. R. Boehly, M. J. Bonino, T. J. B. Collins, R. S. Craxton, J. A. Delettrez, D. H. Edgell, R. Epstein, R. K. Follet, C. J. Forrest, D. H. Froula, V. Yu. Glebov, D. R. Harding, R. J. Henchen, S. X. Hu, I. V. Igumenshchev, R. Janezic, J. H. Kelly, T. J. Kessler, T. Z. Kosc, S. J. Loucks, J. A. Marozas, F. J. Marshall, A. V. Maximov, R. L. McCrory, P. W. McKenty, D. D. Meyerhofer, D. T. Michel, J. F. Myatt, R. Nora, P. B. Radha, S. P. Regan, W. Seka, W. T. Shmayda, R. W. Short, A. Shvydky, S. Skupsky, C. Stoeckl, B. Yaakobi, J. A. Frenje, M. Gatu-Johnson, R. D. Petrasso, and D. T. Casey, Phys. Plasmas **21**, 056315 (2014).

22. J. A. Marozas, F. J. Marshall, R. S. Craxton, I. V. Igumenshchev, S. Skupsky, M. J. Bonino, T. J. B. Collins, R. Epstein, V. Yu. Glebov, D. Jacobs-Perkins, J. P. Knauer, R. L. McCrory, P. W. McKenty, D. D. Meyerhofer, S. G. Noyes, P. B. Radha, T. C. Sangster, W. Seka, and V. A. Smalyuk, Phys. Plasmas **13**, 056311 (2006).

23. D. Cao, G. Moses, and J. Delettrez, Phys. Plasmas **22**, 082308 (2015).

24. D. H. Edgell, P. B. Radha, V. N. Goncharov, I. V. Igumenshchev, J. A. Marozas, J. F. Myatt, W. Seka, and D. H. Froula, Bull. Am. Phys. Soc. **57**, 343 (2012).

25. D. E. Bower, T. J. McCarville, S. S. Alvarez, L. E. Ault, M. D. Brown, M. P. Chrisp, C. M. Damian, W. J. DeHope, D. H. Froula, S. H. Glenzer, S. E. Grace, K. Gu, F. R. Holdener, C. K. Huffer, J. H. Kamperschroer, T. M. Kelleher, J. R. Kimbrough, R. Kirkwood, D. W. Kurita, A. P. Lee, F. D. Lee, I. T. Lewis, F. J. Lopez, B. J. MacGowan, M. W. Poole, M. A. Rhodes, M. B. Schneider, N. R. Sewall, F. Y. Shimamoto, S. J. Shiromizu, D. Voloshin, A. L. Warrick, C. R. Wendland, and B. K. Young, Rev. Sci. Instrum. **75**, 4177 (2004); J. D. Moody *et al*., Rev. Sci. Instrum. **81**, 10D921 (2010); P. Datte *et al*., Proc. SPIE **8850**, 885003 (2013).

26. D. T. Michel, C. Sorce, R. Epstein, N. Whiting, I. V. Igumenshchev, R. Jungquist, and D. H. Froula, Rev. Sci. Instrum. **83**, 10E530 (2012).

27. F. J. Marshall, P. W. McKenty, J. A. Delettrez, R. Epstein, J. P. Knauer, V. A. Smalyuk, J. A. Frenje, C. K. Li, R. D. Petrasso, F. H. Séguin, and R. C. Mancini, Phys. Rev. Lett. **102**, 185004 (2009).

28. J. J. MacFarlane *et al*., High Energy Density Phys. **3**, 181 (2007).

29. *LLE Review Quarterly Report* **91**, 116, Laboratory for Laser Energetics, University of Rochester, Rochester, NY, LLE Document No. DOE/SF/19460-458, NTIS Order No. PB2006-106662 (2002). Copies may be obtained from the National Technical Information Service, Springfield, VA 22161.

30. G. Fiksel, S. X. Hu, V. N. Goncharov, D. D. Meyerhofer, T. C. Sangster, V. A. Smalyuk, B. Yaakobi, M. J. Bonino, and R. Jungquist, Phys. Plasmas **19**, 062704 (2012).

31. A. N. Mostovych, D. G. Colombant, M. Karasik, J. P. Knauer, A. J. Schmitt, and J. L. Weaver, Phys. Rev. Lett. **100**, 075002 (2008).

32. R. C. Malone, R. L. McCrory, and R. L. Morse, Phys. Rev. Lett. **34**, 721 (1975); J. Delettrez, Can. J. Phys. **64**, 932 (1986).

33. M. Hohenberger, F. Albert, N. E. Palmer, J. J. Lee, T. Döppner, L. Divol, E. L. Dewald, B. Bachmann, A. G. MacPhee, G. LaCaille, D. K. Bradley, and C. Stoeckl, Rev. Sci. Instrum. **85**, 11D501 (2014).

34. B. Yaakobi, A. A. Solodov, J. F. Myatt, J. A. Delettrez, C. Stoeckl, and D. H. Froula, Phys. Plasmas **20**, 092706 (2013).

35. J. A. Delettrez, T. J. B. Collins, and C. Ye, Bull. Am. Phys. Soc. **59**, 150 (2014).

36. T. J. Murphy, N. S. Krasheninnikova, G. A. Kyrala, P. A. Bradley, J. A. Baumgaertel, J. A. Cobble, P. Hakel, S. C. Hsu, J. L. Kline, D. S. Montgomery, K. A. D. Obrey, R. C. Shah, I. L. Tregillis, M. J. Schmitt, R. J. Kanzleiter, S. H. Batha, R. J. Wallace, S. D. Bhandarkar, P. Fitzsimmons, M. L. Hoppe, A. Nikroo, M. Hohenberger, P. W. McKenty, H. G. Rinderknecht, M. J. Rosenberg, and R. D. Petrasso, Phys. Plasmas **22**, 092707 (2015); N. S. Krasheninnikova *et al*., Phys. Plasmas **21**, 042703 (2014).

37. T. J. Murphy, Los Alamos National Laboratory, private communication (2015).

38. F. Weilacher, P. B. Radha, T. J. B. Collins, and J. A. Marozas, Phys. Plasmas **22**, 032701 (2015); D. Cao, J. A. Marozas, T. J. B. Collins, P. B. Radha, and P. W. McKenty, Bull. Am. Phys. Soc. **60**, 29 (2015).

39. A. R. Christopherson, R. Betti, W. Theobald, and J. Howard, the Ninth International Conference on Inertial Fusion Sciences and Applications (IFSA 2015), Seattle, WA, 20–25 September 2015 (Paper Th.O.2.2).

40. *LLE Review Quarterly Report* **130**, 72, Laboratory for Laser Energetics, University of Rochester, Rochester, NY, LLE Document No. DOE/NA/28302-1058 (2012).

41. *LLE Review Quarterly Report* **79**, 121, Laboratory for Laser Energetics, University of Rochester, Rochester, NY, LLE Document No. DOE/SF/19460-317, NTIS Order No. DE2002762802 (1999). Copies may be obtained from the National Technical Information Service, Springfield, VA 22161.

42. W. Seka, D. H. Edgell, J. F. Myatt, A. V. Maximov, R. W. Short, V. N. Goncharov, and H. A. Baldis, Phys. Plasmas **16**, 052701 (2009).

43. M. Hohenberger, A. Shvydky, P. B. Radha, M. J. Rosenberg, V. N. Goncharov, F. J. Marshall, J. P. Knauer, S. P. Regan, T. C. Sangster, A. Nikroo, and R. J. Wallace, Bull. Am. Phys. Soc. **60**, 164 (2015); A. Shvydky, M. Hohenberger, P. B. Radha, M. J. Rosenberg, R. S. Craxton, V. N. Goncharov, J. A. Marozas, F. J. Marshall, P. W. McKenty, S. P. Regan, and T. C. Sangster, Bull. Am. Phys. Soc. **60**, 118 (2015).

44. J. A. Marozas, T. J. B. Collins, J. D. Zuegel, P. B. Radha, F. J. Marshall, and W. Seka, presented at the 44th Annual Anomalous Absorption Conference, Estes Park, CO, 8–13 June 2014.

45. D. T. Michel, V. N. Goncharov, I. V. Igumenshchev, R. Epstein, and D. H. Froula, Phys. Rev. Lett. **111**, 245005 (2013).

Hydrodynamic Simulations of Long-Scale-Length Plasmas for Two-Plasmon–Decay Planar-Target Experiments at the National Ignition Facility

Introduction

Coronal plasmas of direct-drive–ignition designs with a baseline plastic ablator are characterized by long density scale lengths $L_n \sim 500$ to 600 μm. Understanding and controlling the impact of laser–plasma interaction (LPI) instabilities in such plasmas are key requirements of inertial confinement fusion (ICF) research. One of the instabilities driven by multiple laser beams that can exceed the instability threshold is two-plasmon decay (TPD).[1–4] In TPD, the overlapping intense laser beams excite large-amplitude electron plasma waves in the region near the quarter-critical density (n_{qc}) surface, leading to extra laser absorption and hot-electron production. The extra absorption at n_{qc} may reduce, however, the laser intensity reaching critical density, thereby decreasing the hydroefficiency. The hot-electron generation from TPD may negatively affect target compression because of the possible preheat of the imploding shell, which must remain on a low adiabat for efficient compression. Other LPI instabilities, such as multibeam stimulated Raman scattering (SRS), can also lead to anomalous laser-energy dissipation before the n_{qc} surface and/or hot-electron generation.

To support direct-drive ICF experiments at the National Ignition Facility (NIF) in its indirect-drive beam configuration, the polar-direct-drive (PDD) concept was proposed.[5] The impact of laser parametric instabilities on the PDD implosions has been recently tested in experiments on the NIF.[6] To investigate the scaling of TPD-induced hot electrons to the laser intensity and plasma conditions, a series of planar experiments has also been conducted at the Omega Laser Facility.[7] The plasma parameters at the n_{qc} surface achieved in those experiments (as predicted by simulations using the code *DRACO*[8]) are summarized in Table 145.II. The coronal plasma parameters in the NIF PDD-ignition design developed at the Laboratory for Laser Energetics[9] are also shown. Table 145.II shows that all parameters in the previous experiments [the overlapped laser intensity (I), density scale length (L_n), and electron temperature (T_e) at the n_{qc} surface] are still ~1.5 to 2× below that in the ignition design. The empirical TPD threshold parameter $\eta = I_{14}L_{n,\mu m}/(230\,T_{e,keV})$, often used to evaluate the effect of TPD,[2,10] is ~2× less than in the ignition design. Importantly, cross-beam energy transfer (CBET) reduces the laser beam energy, reaching the n_{qc} surface in current NIF implosion experiments, so that current implosion experiments do not achieve ignition-relevant coronal plasma conditions.

In this article, hydrodynamic simulations using *DRACO* are presented to show that coronal plasma conditions in the ignition PDD design can be approached in planar-target experiments on the NIF (Table 145.II). Since planar targets exhibit a very high absorption efficiency, CBET seeded by backscattered light represents a negligible source of losses in laser energy. It is speculated that because of the characteristics of the NIF beam overlap on the target, the TPD instability will be able to share decay waves most effectively along the polar axis and around the equatorial region of a PDD implosion. Two planar-target simulations that differ by the NIF beam irradiation geometry are presented: (1) irradiation by the NIF inner-cone beams only (23.5° and 30° incidence angle with respect to target normal) and (2) irradiation by the outer-cone beams (44.5° and 50°). The higher-angle cones approximate irradiation conditions near the equator of a PDD implosion, while the lower-angle cones correspond to those near the poles.

Table 145.II: Plasma parameters at the n_{qc} surface and two-plasmon−decay (TPD) threshold in OMEGA and NIF experiments, ignition NIF PDD design, and planar targets in this article, as predicted by *DRACO* simulations.

Parameters at n_{qc} surface	OMEGA	Current NIF PDD	Ignition NIF PDD	Planar NIF
I (W/cm^2)	$<4 \times 10^{14}$	$<4.5 \times 10^{14}$	8 to 10×10^{14}	6 to 8×10^{14}
L_n (μm)	<350 μm	<350 μm	600 μm	550 to 600 μm
T_e (keV)	<2.5 keV	<3.5 keV	5 keV	3.2 keV
η	<2.4	<2	4.7	4.5 to 5.5

Proposed Experimental Configuration

The planar-target design is shown schematically in Fig. 145.17. The target is an ~5-mm-diam, ~500-μm-thick plastic CH disk. A 30-μm-thick, ~4-mm-diam Mo disk is buried 40 μm behind the target's front surface. The target is oriented in the equatorial plane of the NIF chamber and irradiated by a subset of NIF beams from the south pole. Hot electrons generated by the LPI instability in the coronal plasma flow into the target. Time-resolved K_α line emission and the hard x-ray bremsstrahlung from Mo are used as the main hot-electron diagnostics. The Mo thickness is equal to the range of electrons of a typical energy of ~120 keV. Hot electrons that are not stopped in Mo are slowed down in the back CH, so that electron recirculation is minimal in this experiment. The front CH layer is chosen to be thick enough to avoid a burnthrough to the Mo layer, while sufficiently thin to reduce collisional energy losses of hot electrons on the way toward the Mo. For the proposed target thickness, the laser-induced shock does not reach the back of the target, and the target is not accelerated when the laser pulse is on. The simulations use laser pulses with a 2-ns linear power rise from zero to the maximum value and flattop after that, with a total duration of 5.5 to 7.5 ns.

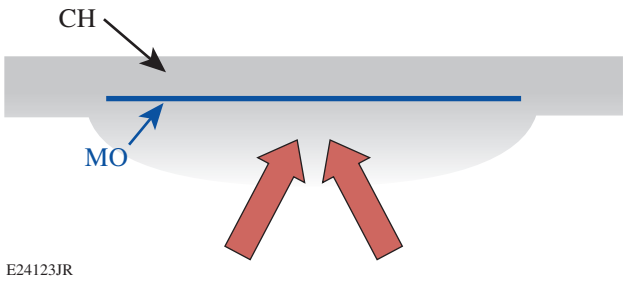

Figure 145.17
The proposed target design.

The measurements can be performed using the NIF x-ray spectrometer[11] to measure the time-resolved Mo K_α emission and the filter-fluorescer x-ray diagnostic[12] to measure the time-resolved hard x-ray emission. NIF optical spectrometers can measure the half-frequency $(\omega_L/2)$ harmonic of the incident light, which is a characteristic signature of TPD, and SRS spectra.

DRACO Simulations

The simulations were performed using the Eulerian version of *DRACO*[8] in cylindrically symmetric geometry. *DRACO* includes a full three-dimensional (3-D) laser ray trace, a flux-limited heat-conduction model (with a flux limiter $f = 0.1$), multigroup diffusive radiation transport, and *SESAME* equation of state. For the low-Z plastic CH ablator, the Astrophysics Opacity Table was applied; the average-ion model, which is a collisional-radiative-equilibrium model, was used for the high-Z Mo.

The simulations used the actual measured focal-spot shapes of the indirect-drive NIF beams. The beams are used at best focus and pointed at the averaged-over-time longitudinal position of the n_{qc} surface—320 μm in front of the target surface. The simulations are designed to have similar plasma parameters at the n_{qc} surface, with flattop total powers of 17 TW and 15 TW, durations of 5.5 ns and 7.5 ns in the inner- (32 beams at 23.5° and 30°) and outer-cone beam (64 beams at 44.5° and 50°) simulations, respectively. The duration of the flattop used in the inner-cone beam simulation is chosen to be the longest allowable while still avoiding laser damage on the NIF.

Figure 145.18 presents the electron density and electron temperature in the coronal plasma at $t = 4.5$ ns in the inner-cone

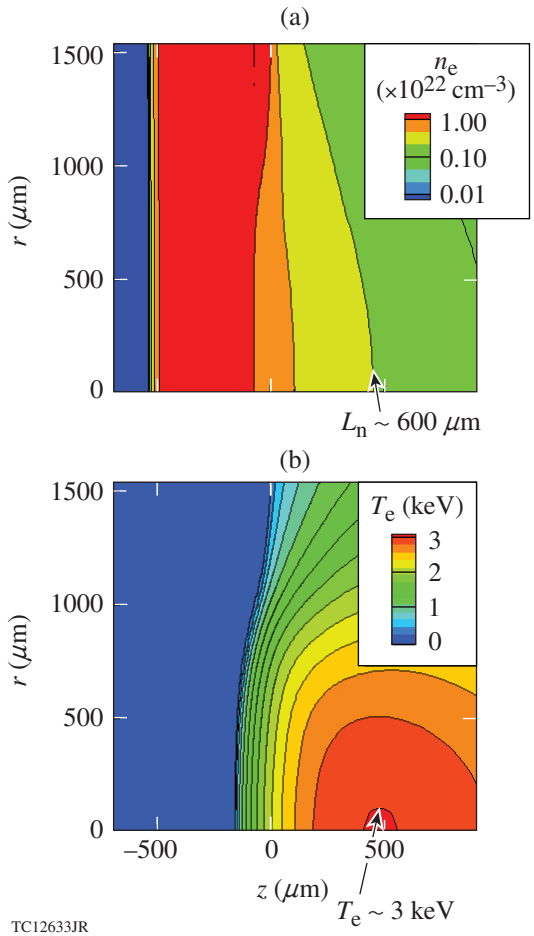

Figure 145.18
The (a) electron density and (b) electron temperature in the coronal plasma at $t = 4.5$ ns in the inner-cone beam simulation.

beam simulation. The outer-cone beam simulation predicts similar results (with a slightly higher peak temperature of 3.15 keV) and is not shown.

Figure 145.19 shows the time evolution of the plasma parameters at the n_{qc} surface and TPD threshold parameter at $r = 0$ in both simulations. The density scale length and electron temperature are almost stationary at $t > 2.5$ ns with $L_n = 500$ to 600 μm and $T_e \sim 3$ to 3.3 keV. Laser intensity slowly decreases with time, with $I = 5$ to 6.5×10^{14} W/cm^2 in the inner-cone beam and $I = 6$ to 8×10^{14} W/cm^2 in the outer-cone beam simulation. Notably, the empirical TPD threshold is greatly exceeded in these simulations—$\eta \sim 4$ to 5.

Discussion and Conclusions

Overall, a similar evolution of the plasma parameters at the n_{qc} surface is predicted by *DRACO* simulations for the inner- and outer-cone beams. Planar-target experiments on the NIF, therefore, can study the effect of a beam's incidence angle on TPD instability and hot-electron generation. Simulations of TPD using the 3-D laser–plasma interaction code *LPSE*[13] have been performed using the NIF irradiation geometry and plasma parameters at the n_{qc} surface predicted by *DRACO*. *LPSE* models the TPD instability in a small volume of plasma (200 μm × 30 μm × 30 μm) close to the n_{qc} surface. *LPSE* simulations confirm the onset of TPD instability when the TPD threshold (η) exceeds unity in *DRACO* simulations for both irradiation geometries. The mechanisms of saturation of the TPD instability (such as pump depletion) are currently under implementation in *LPSE*. *LPSE* will be used to study hot-electron production and laser absorption at the nonlinear stage of TPD.

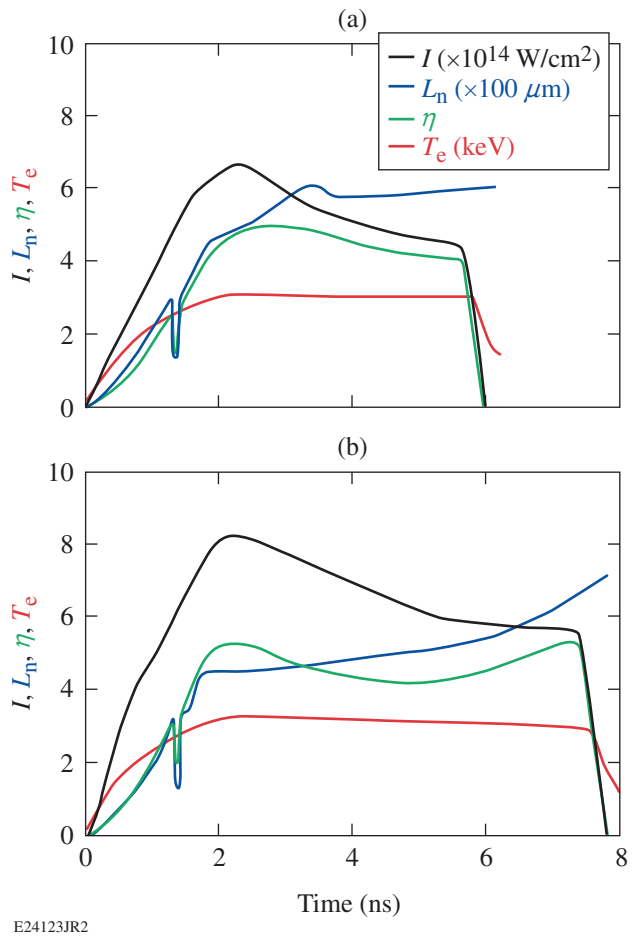

Figure 145.19
Time evolution of the plasma parameters at the n_{qc} surface and TPD threshold parameter at $r = 0$ in the (a) inner- and (b) outer-cone beam simulations.

Table 145.II shows that the plasma parameters at the n_{qc} surface in the present simulations are closer to the PDD-ignition design than in the OMEGA and current NIF PDD implosion experiments, with the exception of the electron temperature. In particular, the plasma density scale length is as long as that in the ignition design. A relatively low temperature is explained by higher transversal thermoconduction losses in planar experiments compared to those in spherical implosions. The laser power can be further increased, provided the optics' damage threshold is not exceeded. This can allow one to study TPD at higher overlapped laser intensity (equal or exceeding that in the ignition design) and electron temperature at the n_{qc} surface. The power can be increased by up to a factor of 2 in the outer-beam configuration. The power can also be increased at the expense of decreased pulse duration in the inner-beam configuration.

In conclusion, hydrodynamic simulations suggest that planar-target experiments on the NIF can be a powerful tool in the study of TPD and other LPI processes in the plasma conditions relevant to the ignition direct-drive designs. While current NIF PDD experiments suffer from CBET, which reduces the laser absorption, planar NIF experiments can provide a first look at the effect of TPD in NIF PDD implosions when CBET has been mitigated. Subsequently, the NIF planar platform can be used to study TPD mitigation strategies by using different ablator materials.

ACKNOWLEDGMENT

This material is based upon work supported by the Department of Energy National Nuclear Security Administration under Award Number DE-NA0001944, the University of Rochester, and the New York State Energy Research and Development Authority. The support of DOE does not constitute an endorsement by DOE of the views expressed in this article.

REFERENCES

1. M. N. Rosenbluth, Phys. Rev. Lett. **29**, 565 (1972).

2. A. Simon, R. W. Short, E. A. Williams, and T. Dewandre, Phys. Fluids **26**, 3107 (1983).

3. D. T. Michel, A. V. Maximov, R. W. Short, S. X. Hu, J. F. Myatt, W.Seka, A. A. Solodov, B. Yaakobi, and D. H. Froula, Phys. Rev. Lett. **109**, 155007 (2012).

4. J. Zhang, J. F. Myatt, R. W. Short, A. V. Maximov, H. X. Vu, D. F. DuBois, and D. A. Russell, Phys. Rev. Lett. **113**, 105001 (2014).

5. S. Skupsky, J. A. Marozas, R. S. Craxton, R. Betti, T. J. B. Collins, J. A. Delettrez, V. N. Goncharov, P. W. McKenty, P. B. Radha, T. R. Boehly, J. P. Knauer, F. J. Marshall, D. R. Harding, J. D. Kilkenny, D.D. Meyerhofer, T. C. Sangster, and R. L. McCrory, Phys. Plasmas **11**, 2763 (2004).

6. M. Hohenberger, P. B. Radha, J. F. Myatt, S. LePape, J. A. Marozas, F. J. Marshall, D. T. Michel, S. P. Regan, W. Seka, A. Shvydky, T. C. Sangster, J. W. Bates, R. Betti, T. R. Boehly, M. J. Bonino, D. T. Casey, T. J. B. Collins, R. S. Craxton, J. A. Delettrez, D. H. Edgell, R. Epstein, G. Fiksel, P. Fitzsimmons, J. A. Frenje, D. H. Froula, V. N. Goncharov, D. R. Harding, D. H. Kalantar, M. Karasik, T. J. Kessler, J. D. Kilkenny, J. P. Knauer, C. Kurz, M. Lafon, K. N. LaFortune, B. J. MacGowan, A. J. Mackinnon, A. G. MacPhee, R. L. McCrory, P. W. McKenty, J. F. Meeker, D. D. Meyerhofer, S. R. Nagel, A. Nikroo, S. Obenschain, R. D. Petrasso, J. E. Ralph, H. G. Rinderknecht, M. J. Rosenberg, A. J. Schmitt, R. J. Wallace, J. Weaver, C. Widmayer, S. Skupsky, A. A. Solodov, C. Stoeckl, B. Yaakobi, and J. D. Zuegel, Phys. Plasmas **22**, 056308 (2015).

7. B. Yaakobi, P.-Y. Chang, A. A. Solodov, C. Stoeckl, D. H. Edgell, R. S. Craxton, S. X. Hu, J. F. Myatt, F. J. Marshall, W. Seka, and D. H. Froula, Phys. Plasmas **19**, 012704 (2012).

8. P. B. Radha, T. J. B. Collins, J. A. Delettrez, Y. Elbaz, R. Epstein, V. Yu. Glebov, V. N. Goncharov, R. L. Keck, J. P. Knauer, J. A. Marozas, F. J. Marshall, R. L. McCrory, P. W. McKenty, D. D. Meyerhofer, S. P. Regan, T. C. Sangster, W. Seka, D. Shvarts, S. Skupsky, Y. Srebro, and C. Stoeckl, Phys. Plasmas **12**, 056307 (2005).

9. T. J. B. Collins, J. A. Marozas, K. S. Anderson, R. Betti, R. S. Craxton, J. A. Delettrez, V. N. Goncharov, D. R. Harding, F. J. Marshall, R. L. McCrory, D. D. Meyerhofer, P. W. McKenty, P. B. Radha, A. Shvydky, S. Skupsky, and J. D. Zuegel, Phys. Plasmas **19**, 056308 (2012).

10. W. Seka, D. H. Edgell, J. F. Myatt, A. V. Maximov, R. W. Short, V. N. Goncharov, and H. A. Baldis, Phys. Plasmas **16**, 052701 (2009).

11. S. P. Regan, K. B. Fournier, M. J. Bedzyk, A. Agliata, S. L. Ayers, M. A. Barrios, P. M. Bell, D. K. Bradley, H. Chen, J. A. Emig, R. K. Jungquist, G. E. Kemp, J. D. Kilkenny, D. D. Meyerhofer, F. Perez, J. Pino, T. C. Sangster, and M. J. Shoup III, SPIE Optics and Photonics 2014, San Diego, CA, 17–21 August 2014 (Paper 9211-15).

12. M. Hohenberger, F. Albert, N. E. Palmer, J. J. Lee, T. Döppner, L. Divol, E. L. Dewald, B. Bachmann, A. G. MacPhee, G. LaCaille, D. K. Bradley, and C. Stoeckl, Rev. Sci. Instrum. **85**, 11D501 (2014).

13. J. F. Myatt, J. G. Shaw, V. N. Goncharov, J. Zhang, A. V. Maximov, R. W. Short, R. K. Follett, W. Seka, D. H. Edgell, and D. H. Froula, "Laser–Plasma Interaction in Direct-Drive Inertial Confinement Fusion," submitted to the Journal of Physics: Conference Series.

First-Principles Investigations on Ionization and Thermal Conductivity of Polystyrene (CH) for Inertial Confinement Fusion Applications

Introduction

Controlled inertial confinement fusion (ICF) has been pursued in laboratories for decades, in both indirect-drive[1–3] and direct-drive[4–6] schemes. A typical ICF target consists of layered solid deuterium–tritium (DT) covered with an ablator layer.[7] The ablator layer is used to convert the laser and/or x-ray energy to the kinetic energy of the imploding shell (besides compressing it) by the rocket effect through the ablation process. Polystyrene (CH) is often chosen as the ablator material[7] since it is inexpensive and easy to make. Upon x-ray or laser ablation, the CH ablator can be shocked to pressures up to tens of Mbars. The target convergence can further bring the CH-layer pressure to Gbars, or even hundreds of Gbars at peak compression. Besides ICF applications, CH is also often used as an effective ablator for high-energy-density–physics (HEDP) experiments.[8–10] The properties of CH plasmas under such high-energy-density conditions are essential for understanding ICF and HEDP experiments involving CH ablators.

Because of its importance to ICF, the plasma properties of polystyrene have been extensively studied in both experiment and theory. For example, the principal Hugoniot of CH has been measured using gas-gun experiments[11] and laser/x-ray–launched shocks.[12–16] The measured pressures, temperatures, and reflectivity of shocked CH compare well with state-of-the-art calculations using first-principles methods[17–19] along the principal Hugoniot. The original *SESAME* model (Table 7593 for CH) gave a reasonable Hugoniot in the pressure range that experiments explored, while it overestimated the Hugoniot temperatures.[18,19] Off the principal Hugoniot, we calculated the equations of state over a wide range of CH-plasma conditions and constructed a first-principles equation-of-state (FPEOS) table of CH for ICF applications. The FPEOS of CH has shown significant differences for warm-dense-plasma conditions[19] when compared to the original *SESAME* model. Its effect on ICF implosions has been examined in hydrodynamic simulations: a smaller mass ablation rate was predicted with the CH FPEOS. This prompts us to consider other plasma properties such as ionization and thermal conductivity that can be self-consistently extracted from such first-principles calculations for ICF and HEDP applications.

Thermal conductivity (κ) is an important plasma property that is needed in ICF simulations because it determines the heat transport in ICF plasmas and affects the hydrodynamic instability growth in ICF implosions.[20] In traditional ICF simulations, plasma-physics models of thermal conductivity were adopted in hydrocodes. For example, the Spitzer model[21] has been extensively used for classical plasmas. However, such an analytical model breaks down in warm-dense-plasma conditions since the Spitzer Coulomb logarithm becomes negative for low-temperature and high-density plasmas. To overcome this difficulty of computing κ for warm dense plasmas, the Lee–More model[22] was developed in the 1980s with the first-order approximation to the Boltzmann equation. The Purgatorio model[23] and the SCAALP model,[24] developed about a decade ago, are both based on the average atom model. In the past, quantum-molecular dynamics (QMD) calculations of κ have been performed for ICF-relevant materials of deuterium[25–29] and CH/CH_2 (Refs. 30–32). These first-principles calculations have indicated a larger κ for warm dense D_2 and CH plasmas than the predictions of the Lee–More model that was widely adopted in hydrocodes for ICF simulations. These QMD calculations, however, have been performed for only a few specific density−temperature conditions of CH plasmas. To test whether or not such an enhanced κ of CH will affect ICF simulations, one must extend such QMD calculations to a wide range of plasma conditions, similar to the deuterium case in Ref. 29. In this article, we report on such an endeavor to "gauge" the global behavior of CH thermal conductivity from direct QMD calculations of κ for a wide range of CH plasma conditions. The obtained analytical form of κ, fitted with the generalized QMD Coulomb logarithm, has then been used in hydrodynamic simulations to explore its effect in ICF implosions. Our results show that the κ_{QMD} simulations give an ~20% variation in neutron yield and peak hot-spot pressure when compared to the use of the traditional Lee–More model.

A brief description of the QMD method is presented that combines the orbital-based Kohn–Sham molecular dynamics (KSMD) method with the orbital-free molecular dynamics (OFMD). Since all physics models of the thermal conductivity invoked the use of an effective ionic charge in single-fluid ICF simulations, we first present the OFMD calculations of the average ionization $\left(\langle Z\rangle \text{ and } \langle Z^2\rangle\right)$ of CH over a wide range of plasma densities and temperatures. The obtained $\langle Z\rangle$ and $\langle Z^2\rangle$ are then fitted with a Saha-type model, while the KSMD-derived thermal conductivities of CH are compared with the Lee–More model and fitted with the generalized Coulomb logarithm $[(\ln\Lambda)_{\mathrm{QMD}}]$. The κ_{QMD} effects on ICF implosions for both OMEGA and National Ignition Facility (NIF) targets are presented, followed by the conclusions.

The Quantum-Molecular Dynamics Method

The QMD method is an effective first-principles method for simulating warm dense plasmas,[33–36] where quantum mechanics is used to describe the dynamics of electrons in combination with classical molecular dynamics for the ion motion. To make the quantum-mechanical computations of a many-electron system feasible, the traditional QMD method is based on the density functional theory (DFT).[37–39] Depending on the choice of DFT implementation, the QMD method can be either orbital based or orbital free. For instance, the KSMD method uses the plane-wave basis in a finite-temperature DFT format, which has been implemented in the Vienna *ab-initio* simulation package (VASP),[40–42] while the OFMD method[43] represents the electronic free energy as a direct function of the electronic density through a semiclassical expansion of the Mermin functional. The KSMD method can handle dense plasmas, but only up to the Fermi temperature; the large number of basis functions needed for high-T plasmas renders KSMD as computationally impractical. In contrast, the OFMD method is suitable for high-T plasma simulations. Combining the two first-principles methods of KSMD and OFMD, we are able to simulate a wide range of plasma conditions. Since both methods have been documented elsewhere, only a brief description follows.

1. KSMD

The KSMD method implemented in VASP is based on the finite-temperature density functional theory (FTDFT). To be specific, the electrons are treated quantum-mechanically by plane-wave FTDFT calculations using the Perdew–Burke–Ernzerhof exchange-correlation functional[44] in the generalized gradient approximation. The electron–ion interaction is modeled by a projector-augmented wave (PAW) pseudopotential. The system was assumed to be in local thermodynamical equilibrium with equal electron and ion temperatures ($T_{\mathrm{e}} = T_{\mathrm{i}}$). The ion temperature was kept constant through simple velocity scaling during a molecular-dynamics simulation.

A periodically replicated cubic cell is used with equal numbers of C and H atoms. The plasma density and the number of atoms determine the volume of the cell. For the present simulations of densities below $\rho = 17.5$ g/cm^3, we have employed 250 atoms in total, while a total of 432 atoms were used for densities of $\rho \geq 25$ g/cm^3. For each molecular-dynamics (MD) step, a set of electronic-state functions for each k point is self-consistently determined for an ionic configuration. Under the Born–Oppenheimer approximation, the ions are moved classically with a velocity Verlet algorithm, according to the combined ionic and electronic forces. Repeating the two steps propagates the system in time, resulting in a set of self-consistent ion configurations and electronic-state functions. These trajectories provide a consistent set of static, dynamic, and optical properties of the simulated CH plasmas.

The Γ-point sampling of the first Brillion zone in the cubic cell was employed and tested with a $2 \times 2 \times 2$ Monkhorst–Pack k-point grid. It was found that the resulting thermal conductivity varies <5%. To converge the plasma property calculations, the plane-wave cutoff energy was set to $E_{\max} = 1000$ eV and the PAW potentials were adopted with tight cores (core radii of 1.1 and 0.8 atomic units for C and H, respectively). A large number of energy bands (up to $N_{\mathrm{b}} = 11{,}000$) have been included to ensure that the population of the highest energy band is $<10^{-4}$. For the lowest temperature, 500 bands and a time step of $\Delta t = 0.5$ fs were used, while at the highest temperature, a larger number of bands (11,000) and a small time step of $\Delta t = 0.011$ fs were used.

To calculate the electronic thermal conductivity of CH plasmas, the linear response of the plasma to an electric field $\mathbf{E}$ and a temperature gradient ∇T are considered, which induce the electric current $\mathbf{j}_{\mathrm{e}}$ and the heat flux $\mathbf{j}_q$:

$$\mathbf{j}_{\mathrm{e}} = \left(eL_{11}\mathbf{E} - \frac{L_{12}\nabla T}{T}\right)\Big/ e\,, \tag{1}$$

$$\mathbf{j}_q = \left(eL_{21}\mathbf{E} - \frac{L_{22}\nabla T}{T}\right)\Big/ e\,. \tag{2}$$

For plasmas having no electric current ($\mathbf{j}_{\mathrm{e}} = 0$), the above equations in combination with the definition of $\mathbf{j}_q = -\kappa\nabla T$ give the thermal conductivity

$$\kappa = \frac{1}{T}\left(L_{22} - \frac{L_{12}^2}{L_{11}}\right) \tag{3}$$

with the Onsager coefficients given by $L_{ij} \equiv L_{ij}(0)$. The frequency-dependent Onsager coefficients can be calculated using the Kubo–Greenwood formalism[45,46]

$$L_{ij}(\omega) = \sum_{mn} \frac{2\pi(-e)^{4-i-j}}{3Vm_e^2\omega} \mathrm{F}_{mn} \left| D_{mn} \right|^2 \times \left(\frac{E_m + E_n}{2} - \mathrm{H}\right)^{i+j-2} \delta(E_m - E_n - \hbar\omega), \tag{4}$$

where V is the atomic volume, E_m (E_n) is the energy of the mth (nth) state, and H is the enthalpy (per atom) of the system. F_{mn} is the difference between the Fermi–Dirac distributions for the involved states m and n at temperature T. The velocity matrix elements D_{mn} can be evaluated from the VASP wave functions. In practical calculations, the δ function in Eq. (4) is approximated by a Gaussian function of width ΔE ($\simeq$0.1 to 0.5 eV). The resulting κ was averaged over at least five snapshots of uncorrelated configurations along the MD trajectories. The convergence of κ required a much larger number of energy bands (~2 to 3×) than for the MD simulation.

2. OFMD

The development of OFMD has been documented elsewhere.[43] In the OFMD method, the free energy is approximated by a direct function of the electronic density through a semiclassical expansion of the Mermin functional. The leading- and next-to-leading-order expansions, in terms of the Planck constant h, give the well-known finite-temperature Thomas–Fermi model. To preserve the electronic density beyond the cutoff radius, the OFMD method has introduced a norm-conserving regularization by imposing an analytical form to the electronic density within the cutoff volume. The local-density approximation (LDA) has been used for the electron exchange correlation functional in our OFMD simulations. The time steps used in these calculations vary from 2.4×10^{-2} fs to 4.8×10^{-3} fs, depending on the density and temperature of the CH plasma. The pressures calculated from both KSMD and OFMD methods at the temperature "boundary" of $T \simeq T_F$ are matched well (within <1%).

Since the OFMD method is not based on the plane-wave orbital expansion, it does not give wave functions as in KSMD; therefore, the transport properties of plasmas at high temperatures cannot be extracted directly from the current OFMD simulations. The OFMD method is used to calculate the static plasma properties such as pressure and internal energy. The OFMD simulations can be used to estimate the average ionization in CH plasmas. It is noted that all electrons (core and valence) are considered in the OFMD method. Although there is no operator for ionization in a quantum many-body system, the concept of average ionization ($\langle Z \rangle$ and $\langle Z^2 \rangle$) is extensively adopted in plasma physics models. To fit our KSMD-calculated thermal-conductivity results with a generalized Coulomb logarithm for its use in hydrocodes, we must apply the OFMD calculations to obtain $\langle Z \rangle$ and $\langle Z^2 \rangle$ for a wide range of plasma conditions.

The OFMD calculations give the total pressure of CH plasmas. As described in previous references,[30,47] one can use the orbital-free average atom model in conjunction with the pressure-matching mixing rule to calculate the average charge states for C and H atoms, respectively. For the case of LDA exchange correlation, the pressure matching is equivalent to equalizing the free-electron density of C and H atoms. Once the effective charge states Z_C and Z_H are obtained, the average ionization quantities of $\langle Z \rangle$ and $\langle Z^2 \rangle$ of CH plasmas can be computed as follows (as defined in our hydrocodes):

$$\langle Z \rangle = (Z_C + Z_H)/2, \tag{5}$$

$$\langle Z^2 \rangle = (Z_C^2 + Z_H^2)/2, \tag{6}$$

for an equal mixture of C and H atoms. The effective charge extensively used in hydrocodes is $Z_{eff} = \langle Z^2 \rangle / \langle Z \rangle$.

Results and Discussions

1. The Average Ionization $\langle Z \rangle$ and $\langle Z^2 \rangle$ of CH

As described above, the OFMD method was used to estimate the average ionization of $\langle Z \rangle$ and $\langle Z^2 \rangle$ for CH plasmas of densities varying from $\rho = 0.01$ g/cm^3 to $\rho = 100$ g/cm^3 and temperatures of $T \simeq 10.8$ to 344.7 eV. As an example, Fig. 145.20 shows the comparison of $\langle Z \rangle$ as a function of CH density between the OFMD prediction and the Astrophysics Opacity Table (AOT)[48] for two plasma temperatures of $T \simeq 10.8$ eV and $T \simeq 86.2$ eV. It is noted that the AOT model, usually patched with cold opacity in the warm-dense-plasma regime, is currently adopted in our hydrocodes for ICF simulations.[49] Figure 145.20 shows that at relatively low densities ($\rho < 1$ g/cm^3), the AOT model gives similar values of $\langle Z \rangle$ as the OFMD calculation for both temperatures, while significant differences are seen for higher densities at both temperatures. For instance, at $T \simeq 86.2$ eV

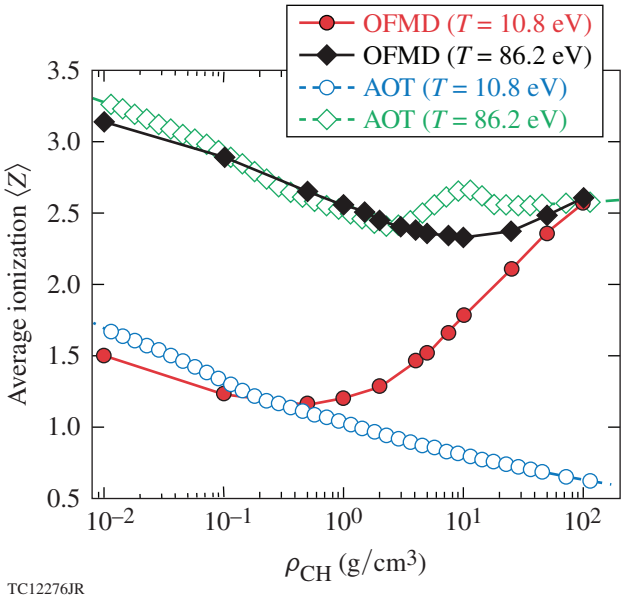

Figure 145.20
The orbital-free molecular dynamics (OFMD)–predicted average ionization $\langle Z\rangle$ as a function of CH density for two plasma temperatures of $T \simeq 10.8$ eV and $T \simeq 86.2$ eV, which are compared with the model predictions (open symbols) by the Astrophysics Opacity Table (AOT) currently used in our hydrocodes.

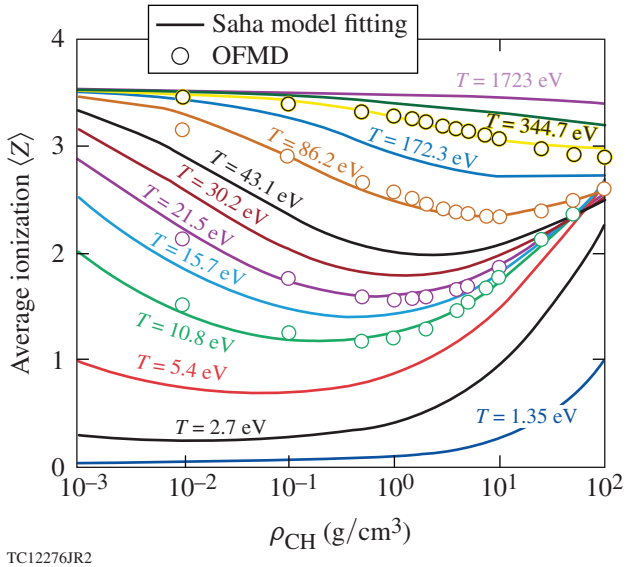

Figure 145.21
The OFMD-predicted average ionization $\langle Z\rangle$ as a function of CH density for plasma temperatures varying from $T \simeq 10.8$ eV to $T \simeq 344.7$ eV, which are fitted with the "Saha-type" ionization model described by Eq. (7).

there are discrepancies in $\langle Z\rangle$ between AOT and OFMD for densities around $\rho = 10$ g/cm^3. Drastic differences are found for the case of a lower temperature at $T \simeq 10.8$ eV: the cold-opacity–patched AOT model does not give the correct behavior of pressure ionization when the CH density increases, which is in contrast to the OFMD prediction. Since low-temperature CH plasma conditions ($T \leq 10$ eV) are often encountered in ICF implosions,[19] it is important that the correct $\langle Z\rangle$ be used for the thermal conductivity models in hydrocodes.

As discussed above, the average ionization of CH plasmas was calculated over a wide range of densities for four different temperatures of $T \simeq 10.8$ eV, 21.6 eV, 86.2 eV, and 344.7 eV. The resulting $\langle Z\rangle$ and $\langle Z^2\rangle$ are plotted in Figs. 145.21 and 145.22 as open symbols. To use these average-ionization quantities in hydrocodes for ICF simulations, a "Saha-type" ionization model for CH plasmas was derived in which the average-ionization fraction ξ is defined as

$$\frac{\xi^2}{1-\xi} = \frac{\alpha_0}{n_i \Lambda_e^3} \exp\left[-\frac{f_Z(\rho,T)}{kT}\right], \qquad (7)$$

where the ion density is defined as $n_i = \rho / A_{CH}$, the electron's thermal de Brogile wavelength is $\Lambda_e = h/\sqrt{2\pi m_e kT}$, with the

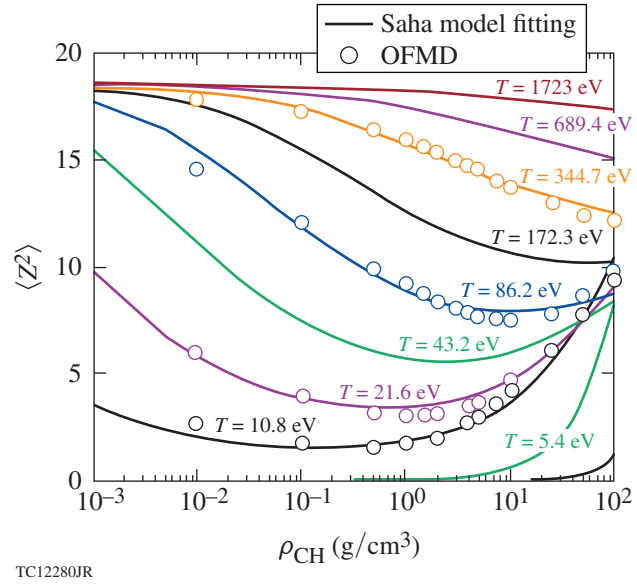

Figure 145.22
The OFMD-predicted average ionization square $\langle Z^2\rangle$ as a function of CH density for plasma temperatures varying from $T \simeq 10.8$ eV to $T \simeq 344.7$ eV, which are fitted with the Saha-type ionization model described by Eq. (9).

Planck constant h and the electron mass m_e, and the density/temperature–dependent average-ionization potential has the following form (kT in eV):

$$f_Z(\rho,T) = \alpha_1 + \alpha_2 \times kT \times \left[\left(1+\sqrt{3\Gamma_0}\right)^{1/4} - 1\right] + \alpha_3 \times (kT)^{0.9} + kT \times \left(\frac{\alpha_4}{r_0} + \frac{\alpha_5}{r_0^2} + \frac{\alpha_6}{r_0^3}\right) \quad (8)$$

with seven fitting parameters α_i. In Eq. (8), the second term accounts for the continuum lowering in the plasma similar to the Stewart–Pyatt form,[50] while the last term is for the pressure ionization. In Eq. (8), the ion–ion interdistance r_0 in terms of the Bohr radius α_B is defined as $n_i = \rho/A_{CH}$ and $r_0 = \left(1/\alpha_B\right)\left(3/4\pi n_i\right)^{1/3}$ with the ion density n_i. The average atomic weight $A_{CH} = \left(A_C + A_H\right)/2$ is used for CH. The quantity Γ_0 is proportional to the ion–ion coupling parameter, i.e., $\Gamma_0 = 1/r_0 kT$. Finally, the average ionization is expressed as $\langle Z\rangle = Z_{max} \times \xi$ with the maximum ionization of $Z_{max} = 3.5$ for the equal mixture of C and H. Performing a least-square fitting to the OFMD data with the above Saha model, we determined the following fitting parameters: $\alpha_0 = 87.222$, $\alpha_1 = 10.866$, $\alpha_2 = -28.412$, $\alpha_3 = 17.915$, $\alpha_4 = -2.422$, $\alpha_5 = 0.595$, and $\alpha_6 = -2.369 \times 10^{-2}$. The fitting is shown by lines in Fig. 145.21 for different temperatures varying from $T \simeq 1.35$ eV to $T \simeq 1723$ eV.

For the average ionization square $\langle Z^2\rangle$, we adopted a similar model to fit the OFMD data, $\langle Z^2\rangle = Z_{max}^2 \times \zeta$ with $Z_{max}^2 = 18.5$ for CH, and ζ is determined as

$$\frac{\zeta^2}{1-\zeta} = \frac{\beta_0}{n_i \Lambda_e^3} \exp\left[-\frac{f_{Z^2}(\rho,T)}{kT}\right] \quad (9)$$

with a different fitting function

$$f_{Z^2}(\rho,T) = \beta_1 + \beta_2 \times kT \times \left[\left(1+\sqrt{3\Gamma_0}\right)^{2/5} - 1\right] + \beta_3 \times (kT)^{3/4} + kT \times \left(\frac{\beta_4}{\sqrt{r_0}} + \frac{\beta_5}{r_0} + \frac{\beta_6}{r_0^{3/2}} + \frac{\beta_7}{r_0^2}\right). \quad (10)$$

The best fit to the OFMD results yielded the following parameters: $\beta_0 = 2.055 \times 10^{-3}$, $\beta_1 = 27.851$, $\beta_2 = -5.087$, $\beta_3 = 6.018$, $\beta_4 = -7.908$, $\beta_5 = 4.421$, $\beta_6 = -2.893$, and $\beta_7 = 0.961$. The model fitting of $\langle Z^2\rangle$ is illustrated in Fig. 145.22 by colored lines, which all compared well with the OFMD results. With a fit for both $\langle Z\rangle$ and $\langle Z^2\rangle$, we can now derive the effective charge of CH plasmas by $Z_{eff} = \langle Z^2\rangle/\langle Z\rangle$ over a wide range of plasma conditions.

2. Thermal Conductivity κ_{QMD} of CH

Using the KSMD calculations with Eq. (3), we have calculated the thermal conductivity of CH plasmas for densities ranging from $\rho = 0.5$ g/cm^3 to $\rho = 100$ g/cm^3. For each density point, the κ_{QMD} calculations have been performed to the highest temperature approaching $T \simeq T_F$ [the Fermi temperature $T_F = \hbar^2/2mk \times \left(3\pi^2 n_e\right)^{2/3}$]. To test the effects of κ_{QMD} on ICF implosions, these results must be fitted in an analytical form. Similar to what we did for the deuterium case,[29] the following function is used for the fitting (in a similar format of κ_{LILAC} currently used in our hydrocode *LILAC*):[51]

$$\kappa_{QMD} = \frac{20 \times (2/\pi)^{3/2} k^{7/2} T^{5/2}}{\sqrt{m_e}\, e^4 Z_{eff}} \times \frac{0.095 \times \left(Z_{eff} + 0.24\right)}{1 + 0.24\, Z_{eff}} \times \frac{1}{(\ln\Lambda)_{QMD}}, \quad (11)$$

with the same Spitzer prefactor as used in κ_{LILAC}. Z_{eff} is the effective charge of CH plasmas that was determined in **The Average Ionization $\langle Z\rangle$ and $\langle Z^2\rangle$ of CH**, p. 21. The generalized QMD Coulomb logarithm is a sixth-order polynomial function of ion–ion coupling and electron degeneracy parameters (Γ_i, θ_e), which has the following form:

$$(\ln\Lambda)_{QMD} = \exp\left\{\gamma_0 + \sum_{j=1}^{6}\left[\gamma_j (\ln\Gamma_i)^j + \sigma_j (\ln\theta_e)^j\right]\right\}, \quad (12)$$

with $\Gamma_i = \langle Z^2\rangle e^2/r_S kT$ and $\theta_e = T/T_F$, in which the Wigner–Seitz radius is defined as $r_S = r_0 \times \alpha_B$ and the free-electron density of $n_e = n_i \times \langle Z\rangle$. Using a multivariable least-square fitting to the κ_{QMD} data, we can determine the parameters γ_j and σ_j. To smoothly merge the κ_{QMD} results to the classical ideal plasma conditions ($\Gamma_i \ll 1$ and $\theta_e \gg 1$), we have added high-temperature κ_{LILAC} points into the dataset for the global fitting. The resulting fitting parameters are $\gamma_0 = -0.482$, $\gamma_1 = -0.150$ or $+0.275$, $\gamma_2 = +0.193$, $\gamma_3 = +8.364 \times 10^{-3}$, $\gamma_4 = -5.287 \times 10^{-3}$, $\gamma_5 = -3.191 \times 10^{-4}$, $\gamma_6 = +2.666 \times 10^{-5}$, $\sigma_1 = +1.00$ or $+1.20$, $\sigma_2 = -0.225$, $\sigma_3 = -4.652 \times 10^{-3}$, $\sigma_4 = +3.805 \times 10^{-3}$, $\sigma_5 = -7.643 \times 10^{-5}$, and $\sigma_6 = -1.391 \times 10^{-5}$. The choice for the two values of γ_1 and σ_1, either $(\gamma_1, \sigma_1) = (-0.15, 1.0)$ or $(\gamma_1, \sigma_1) = (0.275, 1.2)$, is to minimize the Coulomb logarithm for a better fit to the QMD results. The fitting results of $(\ln\Lambda)_{QMD}$ are plotted in Figs. 145.23(a) and 145.23(b) as functions of $\ln(\Gamma_i)$ and $\ln(\theta_e)$, respectively. Overall, the global fitting with the above parameters gives only a small error of 5% or less.

Figures 145.24 and 145.25 compare the QMD-based thermal conductivities of CH plasmas with other models. The "hybrid" Lee–More model (κ_{LILAC}), which combined the Spitzer prefactor with the Lee–More Coulomb logarithm, is currently adopted in our hydrocode *LILAC*. The two others are the Ichimaru model[52] for dense plasmas and the Hubbard model[53] for fully degenerate electron gases. Figure 145.24 compares κ_{QMD} with the different model predictions as a function of plasma temperature for CH densities of $\rho = 1.05$ g/cm^3 (solid density) and $\rho = 4.0$ g/cm^3 (shocked CH). It is seen that κ_{QMD} is generally larger than κ_{LILAC} by a factor of ~2 to 10 at $T < 20$ eV. As indicated in Fig. 145.24(b), the Hubbard model gives reasonably good results in the low-T regime, where the electron degeneracy effect dominates transport behavior, while the Ichimaru model gives the correct trend for plasma temperatures approaching T_F and above. As seen in Fig. 145.23,

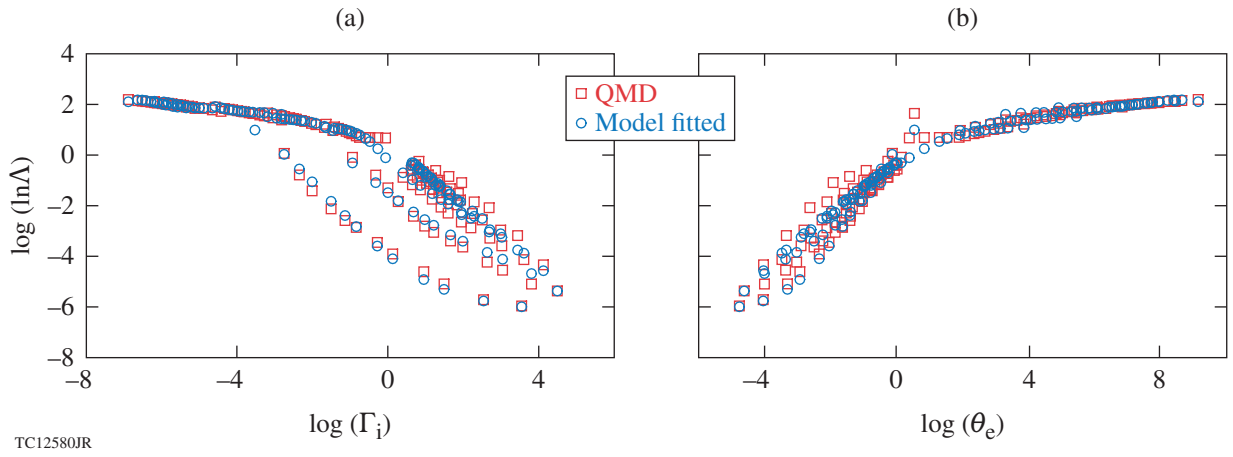

Figure 145.23
The generalized Coulomb logarithm, derived from QMD calculations of thermal conductivity, is fitted with a polynomial function of (a) the ion–ion coupling parameter (Γ_i) and (b) the electron degeneracy parameter (θ_e) of CH plasmas [Eq. (12)].

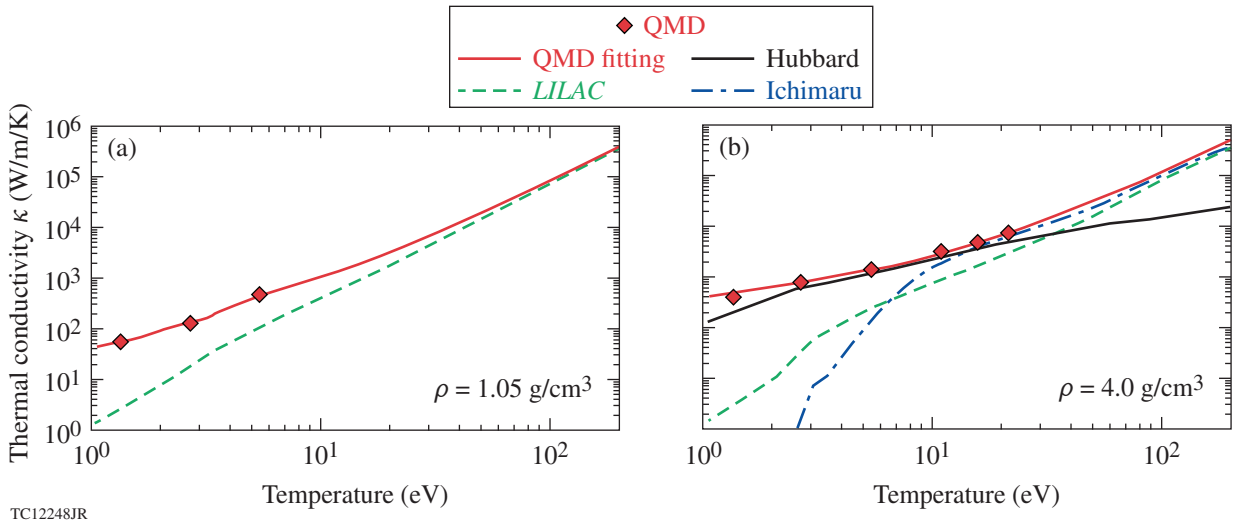

Figure 145.24
Comparison of thermal conductivities of CH plasmas as functions of temperature between QMD calculations and different thermal-conductivity models, for CH densities of (a) $\rho = 1.05$ g/cm^3 and (b) $\rho = 4.0$ g/cm^3. The hybrid *LILAC* model (green dashed lines) used in our hydrocodes adopted the Lee–More model for the Coulomb logarithm with a Spitzer prefactor. The Hubbard model was based on fully degenerate electron gas, while the Ichimaru model considered microfield corrections in dense plasmas.

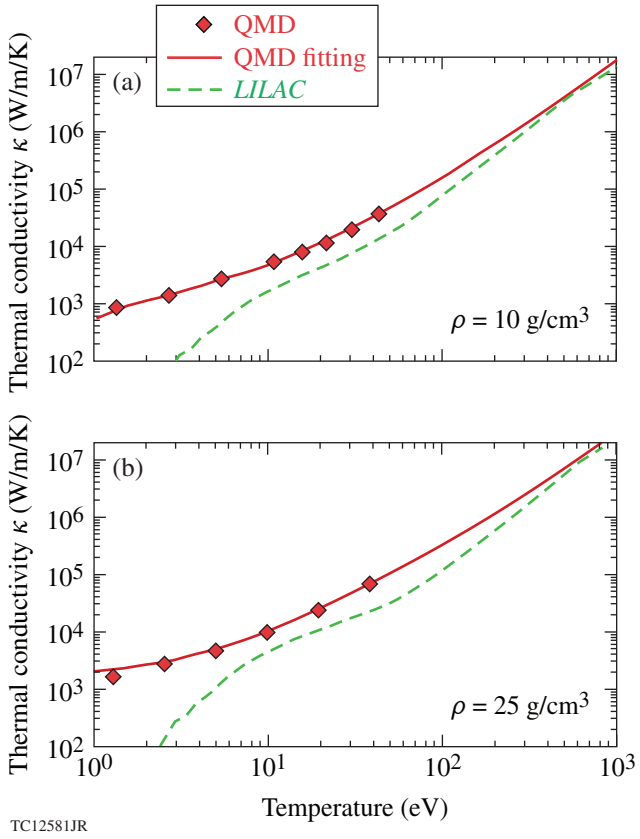

Figure 145.25
Similar to Fig. 145.24 but for CH densities of (a) ρ = 10 g/cm^3 and (b) ρ = 25 g/cm^3.

strongly coupled and degenerate plasmas ($\Gamma_i > 1$ and $\theta_e < 1$) lead to a smaller effective Coulomb logarithm that characterizes the electron collisions in plasmas, while the Lee–More model usually sets a minimum floor of $(\ln\Lambda)_{min} = 2$. The decrease in $(\ln\Lambda)_{QMD}$ means a larger mean free path for electrons, thereby leading to higher thermal conductivity in QMD calculations that account for coupling and degeneracy effects in warm dense CH plasmas. Figures 145.25(a) and 145.25(b) show similar comparisons for higher CH densities at ρ = 10 g/cm^3 and ρ = 25 g/cm^3, respectively. Overall, it is seen that our current hybrid Lee–More model (κ_{LILAC}) underestimates the electronic thermal conductivity when compared with κ_{QMD} in the warm dense plasma regime. The enhancement of κ in the warm dense CH plasmas may have implications in ICF simulations.

The Effect of κ_{QMD} on ICF Simulations

With the implementation of both Z_{eff} and κ_{QMD} into the hydrocode *LILAC* through the fitting formulas discussed above, their effects on ICF simulations may be examined. We first simulate a typical cryogenic DT implosion on OMEGA. Figure 145.26 shows the triple-picket laser pulse used for the implosion, while the inset illustrates the target dimensions. The cryogenic DT target on OMEGA has a 40-μm-thick DT ice layer covered by a 7.5-μm-thick deuterated-plastic (CD) ablator. The total target radius is ~432.5 μm. In the simulations a density scaling to obtain κ_{QMD} for CD from the above-derived κ_{QMD} for CH is used. The triple-picket pulse shape has been used extensively for implosions on OMEGA,[54–56] which enables one to better control shock timing.[57,58]

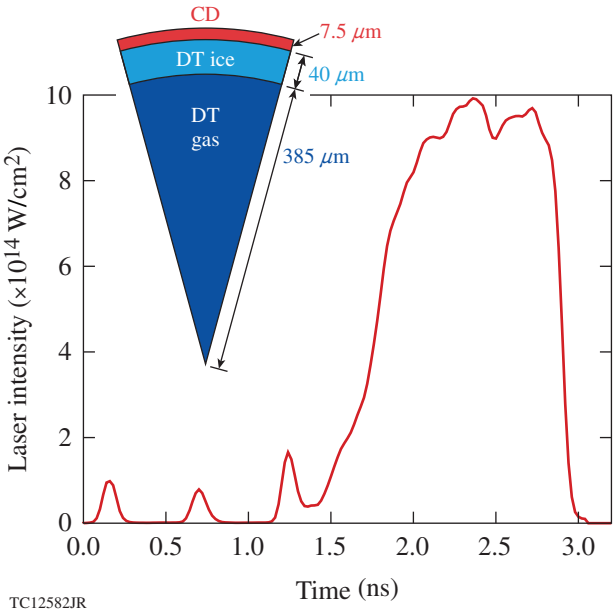

Figure 145.26
The pulse shape and target dimension for a typical cryogenic DT target implosion on OMEGA.

The 1-D *LILAC* hydro simulation results are displayed in Fig. 145.27. Figure 145.27(a) compares density profiles between the κ_{QMD} simulation and the traditional κ_{LILAC} simulation at the end of the laser pulse (t = 2.96 ns). At this time the thin CD layer has been ablated away from the shell. The density of the imploding DT shell is plotted as a function of target radius. One sees that the κ_{QMD} simulation (solid red line) predicts the DT shell being behind the κ_{LILAC} case (DT shell is moving inward); the κ_{QMD} simulation also gives a slightly lower density than the κ_{LILAC} simulation. In the two simulations, we have kept all inputs the same except for the different thermal-conductivity model. Namely, we have employed the FPEOS for both CH[19] and DT,[59] the first-principles opacity table for DT,[49] and a flux-limiter model for thermal transport. The larger value of κ_{QMD} causes more heat to flow into the high-density CD layer, while

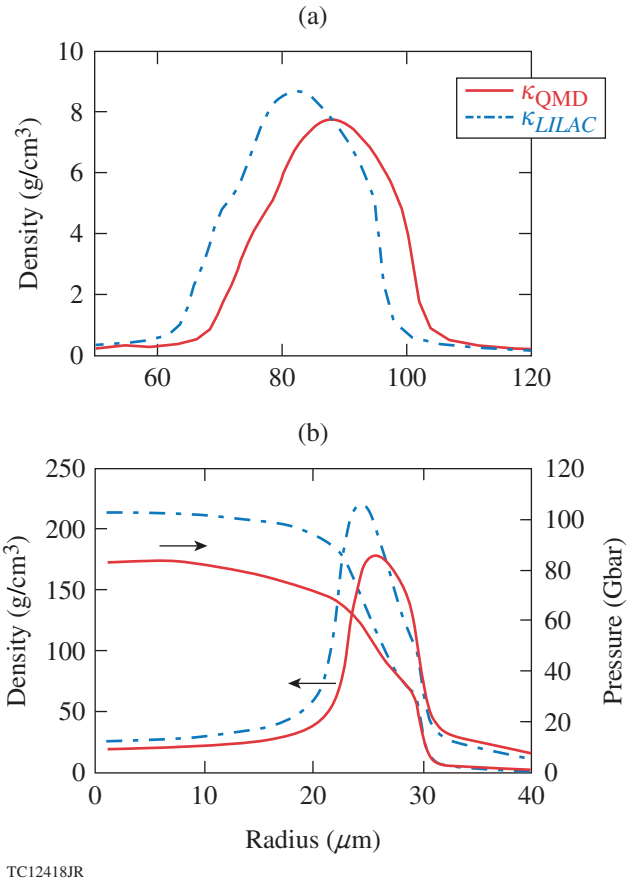

Figure 145.27
Comparison of density profiles and hot-spot pressures predicted by two hydrodynamic simulations using the new κ_{QMD} (red solid lines) and the traditional κ_{LILAC} (blue dashed–dotted lines), respectively. (a) The end of the pulse ($t = 2.96$ ns) and (b) the implosion reaching its peak neutron production ($t = 3.14$ ns). The overall target performances are compared in Table 145.III.

the electron temperature is reduced somewhat between the ablation front and the conduction zone when compared to the κ_{LILAC} case. This reduces the ablation efficiency, thereby leading to a slightly slower implosion. When the DT shell stagnates at $t = 3.14$ ns, the two simulations lead to certain differences in target performance. The comparisons are made in Fig. 145.27(b) for both peak densities in the shell and pressures in the hot spot. The peak density drops from $\rho_p \simeq 220$ g/cm^3 predicted by the κ_{LILAC} simulation to $\rho_p \simeq 180$ g/cm^3 in the κ_{QMD} simulation. Also, the hot-spot peak pressure decreases from $P \simeq 105$ Gbar (κ_{LILAC}) to $P \simeq 84$ Gbar (κ_{QMD}). Table 145.III summarizes the overall comparison in target performance from the two simulations with a variation in yield of ~20%.

The effects of κ_{QMD} are tested for a symmetric direct-drive–ignition design on the NIF, as seen in Figs. 145.28 and 145.29. The pulse shape is shown in Fig. 145.28, which is hydro-equivalently scaled from the above OMEGA target. It consists of a 180-μm-thick DT layer with a 35-μm CD ablator. The target diameter is about 3.43 mm, illustrated by the inset in Fig. 145.28. Results from the two simulations are shown in Fig. 145.29 for comparison. Figure 145.29(a) displays the DT shell's density as a function of target radius for both κ_{LILAC} (blue dashed–dotted line) and κ_{QMD} (red solid line) simulations. Similar to what was found for the implosion case on OMEGA, the NIF simulation using κ_{QMD} also indicates a slight slowdown in the implosion. This causes the difference seen in Fig. 145.29(b) at the start of the ignition burn. The comparison in target performance is summarized in Table 145.IV.

Table 145.III: Comparison of target performance of a typical cryogenic DT implosion on OMEGA simulated with κ_{QMD} versus κ_{LILAC} of CD. The subscript "n" represents neutron-averaged quantities.

OMEGA	κ_{LILAC}	κ_{QMD}
Yield	1.9×10^{14}	1.6×10^{14}
P_{peak}	105 Gbar	84 Gbar
$\langle T_i \rangle_n$	4.17 keV	4.07 keV
$\langle P \rangle_n$	78 Gbar	72 Gbar
$\langle \rho R \rangle_n$	213 mg/cm^2	208 mg/cm^2

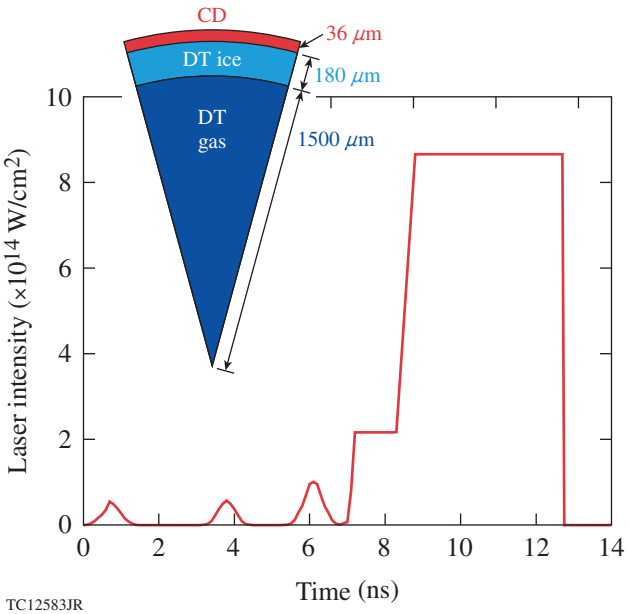

Figure 145.28
The pulse shape and target dimension for a symmetrical ignition design on the NIF.

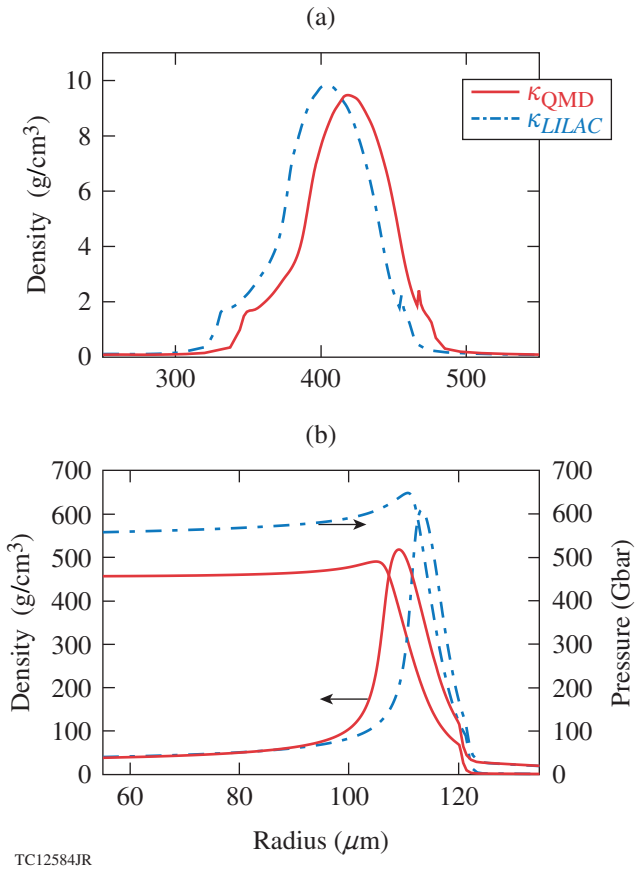

Figure 145.29
Simulation comparison of the NIF design in Fig. 145.28 using the new κ_{QMD} (red solid lines) and the traditional κ_{LILAC} (blue dashed–dotted lines), respectively. (a) The predicted density profiles at the peak velocity (t = 13 ns) and (b) hot-spot pressure and peak shell density compared for the two cases at t = 14 ns. The overall target performance is compared in Table 145.IV.

Table 145.IV: Comparison of a NIF ignition design simulated with κ_{QMD} versus κ_{LILAC} for CD.

NIF	κ_{LILAC}	κ_{QMD}
$\langle \rho R \rangle_n$	0.814 g/cm^2	0.786 g/cm^2
$\langle T_i \rangle_n$	20.8 keV	19.1 keV
$\langle P \rangle_n$	629 Gbar	546 Gbar
$\langle \rho \rangle_{peak}$	639.6 g/cm^3	586.6 g/cm^3
$R_{hot\ spot}$	74.1 μm	78.5 μm
$C_{hot\ spot}$	23.2	21.8
Yield	1.85×10^{19}	1.62×10^{19}
Gain	35	30

The target performance is overall degraded in the κ_{QMD} simulation when compared with the predictions from the traditional κ_{LILAC} simulation. The κ_{QMD} simulation predicts that the hot-spot radius $R_{hot\ spot}$ is slightly bigger and the hot-spot convergence ratio $C_{hot\ spot}$ decreases relative to the κ_{LILAC} case. The final gain is reduced by ~15% in the κ_{QMD} simulation.

Conclusion

Combining the first-principles methods of KSMD and OFMD, the ionization and thermal conductivity of CH plasmas for a wide range of ICF plasma conditions were investigated. The derived average ionization from OFMD calculations has large discrepancies with respect to the astrophysics model predictions in warm dense CH plasmas. The global behavior of $\langle Z \rangle$ and $\langle Z^2 \rangle$ has been fitted with a proposed Saha-type ionization model, which takes the continuum lowering and pressure ionization into account. The derived effective charge $Z_{eff} = \langle Z^2 \rangle / \langle Z \rangle$ is then applied to the global fitting of thermal conductivities κ_{QMD} of CH plasmas, using a generalized Coulomb logarithm $(\ln\Lambda)_{QMD}$. The QMD-based models of Z_{eff} and κ_{QMD} are implemented into our hydrocode for ICF simulations. Compared with the traditional simulations using AOT-based Z_{eff} and κ_{LILAC}, the new simulations with QMD-based Z_{eff} and κ_{QMD} have shown a 15% to ~20% reduction in target performance (yield and energy gain) for both OMEGA and NIF implosions. It is anticipated that these plasma properties of CH, derived from first-principles calculations, will improve the predictions of ICF implosions and other HEDP experiments involving CH ablators. It may also further stimulate the ongoing experimental efforts to measure thermal conductivity in high-energy-density plasmas.[60]

ACKNOWLEDGMENT

This material is based upon work supported by the Department of Energy National Nuclear Security Administration under Award Number DE-NA0001944, the University of Rochester, and the New York State Energy Research and Development Authority. The support of DOE does not constitute an endorsement by DOE of the views expressed in this article. This work was also supported by Scientific Campaign 10 at the Los Alamos National Laboratory, operated by Los Alamos National Security, LLC, for the National Nuclear Security Administration of the U.S. Department of Energy under Contract No. DE-AC52-06NA25396.

REFERENCES

1. S. W. Haan *et al.*, Phys. Plasmas **18**, 051001 (2011).

2. M. J. Edwards, J. D. Lindl, B. K. Spears, S. V. Weber, L. J. Atherton, D. L. Bleuel, D. K. Bradley, D. A. Callahan, C. J. Cerjan, D. Clark, G. W. Collins, J. E. Fair, R. J. Fortner, S. H. Glenzer, S. W. Haan, B. A. Hammel, A. V. Hamza, S. P. Hatchett, N. Izumi, B. Jacoby, O. S. Jones, J. A. Koch, B. J. Kozioziemski, O. L. Landen, R. Lerche, B. J. MacGowan, A. J. MacKinnon, E. R. Mapoles, M. M. Marinak,

M. Moran, E. I. Moses, D. H. Munro, D. H. Schneider, S. M. Sepke, D. A. Shaughnessy, P. T. Springer, R. Tommasini, L. Bernstein, W. Stoeffl, R. Betti, T. R. Boehly, T. C. Sangster, V. Yu. Glebov, P. W. McKenty, S. P. Regan, D. H. Edgell, J. P. Knauer, C. Stoeckl, D. R. Harding, S. Batha, G. Grim, H. W. Herrmann, G. Kyrala, M. Wilke, D. C. Wilson, J. Frenje, R. Petrasso, K. Moreno, H. Huang, K. C. Chen, E. Giraldez, J. D. Kilkenny, M. Mauldin, N. Hein, M. Hoppe, A. Nikroo, and R. J. Leeper, Phys. Plasmas **18**, 051003 (2011).

3. C. Cherfils-Clérouin *et al*., J. Phys.: Conf. Ser. **244**, 022009 (2010).

4. D. D. Meyerhofer, R. L. McCrory, R. Betti, T. R. Boehly, D. T. Casey, T. J. B. Collins, R. S. Craxton, J. A. Delettrez, D. H. Edgell, R. Epstein, K. A. Fletcher, J. A. Frenje, V. Yu. Glebov, V. N. Goncharov, D. R. Harding, S. X. Hu, I. V. Igumenshchev, J. P. Knauer, C. K. Li, J. A. Marozas, F. J. Marshall, P. W. McKenty, P. M. Nilson, S. P. Padalino, R. D. Petrasso, P. B. Radha, S. P. Regan, T. C. Sangster, F. H. Séguin, W. Seka, R. W. Short, D. Shvarts, S. Skupsky, J. M. Soures, C. Stoeckl, W. Theobald, and B. Yaakobi, Nucl. Fusion **51**, 053010 (2011).

5. R. L. McCrory, R. Betti, T. R. Boehly, D. T. Casey, T. J. B. Collins, R. S. Craxton, J. A. Delettrez, D. H. Edgell, R. Epstein, J. A. Frenje, D. H. Froula, M. Gatu-Johnson, V. Yu. Glebov, V. N. Goncharov, D. R. Harding, M. Hohenberger, S. X. Hu, I. V. Igumenshchev, T. J. Kessler, J. P. Knauer, C. K. Li, J. A. Marozas, F. J. Marshall, P. W. McKenty, D. D. Meyerhofer, D. T. Michel, J. F. Myatt, P. M. Nilson, S. J. Padalino, R. D. Petrasso, P. B. Radha, S. P. Regan, T. C. Sangster, F. H. Séguin, W. Seka, R. W. Short, A. Shvydky, S. Skupsky, J. M. Soures, C. Stoeckl, W. Theobald, B. Yaakobi, and J. D. Zuegel, Nucl. Fusion **53**, 113021 (2013).

6. R. S. Craxton, K. S. Anderson, T. R. Boehly, V. N. Goncharov, D. R. Harding, J. P. Knauer, R. L. McCrory, P. W. McKenty, D. D. Meyerhofer, J. F. Myatt, A. J. Schmitt, J. D. Sethian, R. W. Short, S. Skupsky, W. Theobald, W. L. Kruer, K. Tanaka, R. Betti, T. J. B. Collins, J. A. Delettrez, S. X. Hu, J. A. Marozas, A. V. Maximov, D. T. Michel, P. B. Radha, S. P. Regan, T. C. Sangster, W. Seka, A. A. Solodov, J. M. Soures, C. Stoeckl, and J. D. Zuegel, Phys. Plasmas **22**, 110501 (2015).

7. S. W. Haan, H. Huang, M. A. Johnson, M. Stadermann, S. Baxamusa, S. Bhandarkar, D. S. Clark, V. Smalyuk, and H. F. Robey, Phys. Plasmas **22**, 032708 (2015); T. C. Sangster, V. N. Goncharov, R. Betti, T. R. Boehly, D. T. Casey, T. J. B. Collins, R. S. Craxton, J. A. Delettrez, D. H. Edgell, R. Epstein, K. A. Fletcher, J. A. Frenje, V. Yu. Glebov, D. R. Harding, S. X. Hu, I. V. Igumenshchev, J. P. Knauer, S. J. Loucks, C. K. Li, J. A. Marozas, F. J. Marshall, R. L. McCrory, P. W. McKenty, D. D. Meyerhofer, P. M. Nilson, S. P. Padalino, R. D. Petrasso, P. B. Radha, S. P. Regan, F. H. Seguin, W. Seka, R. W. Short, D. Shvarts, S. Skupsky, V. A. Smalyuk, J. M. Soures, C. Stoeckl, W. Theobald, and B. Yaakobi, Phys. Plasmas **17**, 056312 (2010).

8. S. H. Glenzer and R. Redmer, Rev. Mod. Phys. **81**, 1625 (2009).

9. A. L. Kritcher *et al*., Phys. Rev. Lett. **107**, 015002 (2011).

10. L. B. Fletcher *et al*., Phys. Rev. Lett. **112**, 145004 (2014).

11. S. P. Marsh, ed. *LASL Shock Hugoniot Data*, Los Alamos Series on Dynamic Material Properties (University of California Press, Berkeley, CA, 1980).

12. R. Cauble *et al*., Phys. Plasmas **4**, 1857 (1997).

13. N. Ozaki *et al*., Phys. Plasmas **16**, 062702 (2009).

14. M. Koenig *et al*., Phys. Plasmas **10**, 3026 (2003).

15. M. A. Barrios, D. G. Hicks, T. R. Boehly, D. E. Fratanduono, J. H. Eggert, P. M. Celliers, G. W. Collins, and D. D. Meyerhofer, Phys. Plasmas **17**, 056307 (2010).

16. S. Hamel, L. X. Benedict, P. M. Celliers, M. A. Barrios, T. R. Boehly, G. W. Collins, T. Döppner, J. H. Eggert, D. R. Farley, D. G. Hicks, J. L. Kline, A. Lazicki, S. LePape, A. J. Mackinnon, J. D. Moody, H. F. Robey, E. Schwegler, and P. A. Sterne, Phys. Rev. B **86**, 094113 (2012).

17. C. Wang, X.-T. He, and P. Zhang, Phys. Plasmas **18**, 082707 (2011).

18. S. X. Hu, T. R. Boehly, and L. A. Collins, Phys. Rev. E **89**, 063104 (2014).

19. S. X. Hu, L. A. Collins, V. N. Goncharov, J. D. Kress, R. L. McCrory, and S. Skupsky, Phys. Rev. E **92**, 043104 (2015).

20. B. A. Hammel *et al*., High Energy Density Phys. **6**, 171 (2010).

21. L. Spitzer, Jr. and R. Härm, Phys. Rev. **89**, 977 (1953).

22. Y. T. Lee and R. M. More, Phys. Fluids **27**, 1273 (1984).

23. B. Wilson *et al*., J. Quant. Spectrosc. Radiat. Transf. **99**, 658 (2006).

24. G. Faussurier *et al*., Phys. Plasmas **17**, 052707 (2010); J. Clérouin *et al*., Phys. Rev. E **82**, 046402 (2010).

25. V. Recoules *et al*., Phys. Rev. Lett. **102**, 075002 (2009).

26. F. Lambert *et al*., Phys. Plasmas **18**, 056306 (2011).

27. B. Holst, M. French, and R. Redmer, Phys. Rev. B **83**, 235120 (2011).

28. C. Wang *et al*., Phys. Rev. E **88**, 013106 (2013).

29. S. X. Hu, L. A. Collins, T. R. Boehly, J. D. Kress, V. N. Goncharov, and S. Skupsky, Phys. Rev. E **89**, 043105 (2014).

30. F. Lambert and V. Recoules, Phys. Rev. E **86**, 026405 (2012).

31. C. E. Starrett *et al*., Phys. Plasmas **19**, 102709 (2012).

32. D. V. Knyazev and P. R. Levashov, Phys. Plasmas **22**, 053303 (2015).

33. L. Collins *et al*., Phys. Rev. E **52**, 6202 (1995).

34. J. G. Clérouin and S. Bernard, Phys. Rev. E **56**, 3534 (1997).

35. L. A. Collins *et al*., Phys. Rev. B **63**, 184110 (2001).

36. M. P. Desjarlais, Phys. Rev. B **68**, 064204 (2003).

37. P. Hohenberg and W. Kohn, Phys. Rev. **136**, B864 (1964).

38. W. Kohn and L. J. Sham, Phys. Rev. **140**, A1133 (1965).

39. N. D. Mermin, Phys. Rev. **137**, A1441 (1965).

40. G. Kresse and J. Hafner, Phys. Rev. B **47**, 558 (1993).

41. G. Kresse and J. Hafner, Phys. Rev. B **49**, 14,251 (1994).

42. G. Kresse and J. Furthmüller, Phys. Rev. B **54**, 11,169 (1996).

43. F. Lambert, J. Clérouin, and G. Zérah, Phys. Rev. E **73**, 016403 (2006).

44. J. P. Perdew, K. Burke, and M. Ernzerhof, Phys. Rev. Lett. **77**, 3865 (1996); **78**, 1396(E) (1997).

45. R. Kubo, J. Phys. Soc. Jpn. **12**, 570 (1957).

46. D. A. Greenwood, Proc. Phys. Soc. Lond. **71**, 585 (1958).

47. F. Lambert *et al*., Phys. Rev. E **77**, 026402 (2008).

48. W. F. Huebner *et al*., Los Alamos National Laboratory, Los Alamos, NM, Report LA-6760-M (1977).

49. S. X. Hu, L. A. Collins, V. N. Goncharov, T. R. Boehly, R. Epstein, R. L. McCrory, and S. Skupsky, Phys. Rev. E **90**, 033111 (2014).

50. J. C. Stewart and K. D. Pyatt, Jr., Astrophys. J. **144**, 1203 (1966).

51. J. Delettrez, R. Epstein, M. C. Richardson, P. A. Jaanimagi, and B. L. Henke, Phys. Rev. A **36**, 3926 (1987).

52. S. Ichimaru and S. Tanaka, Phys. Rev. A **32**, 1790 (1985); H. Kitamura and S. Ichimaru, Phys. Rev. E **51**, 6004 (1995).

53. W. B. Hubbard, Astrophys. J. **146**, 858 (1966).

54. V. N. Goncharov, T. C. Sangster, T. R. Boehly, S. X. Hu, I. V. Igumenshchev, F. J. Marshall, R. L. McCrory, D. D. Meyerhofer, P. B. Radha, W. Seka, S. Skupsky, C. Stoeckl, D. T. Casey, J. A. Frenje, and R. D. Petrasso, Phys. Rev. Lett. **104**, 165001 (2010).

55. S. X. Hu, V. N. Goncharov, P. B. Radha, J. A. Marozas, S. Skupsky, T. R. Boehly, T. C. Sangster, D. D. Meyerhofer, and R. L. McCrory, Phys. Plasmas **17**, 102706 (2010).

56. T. C. Sangster, V. N. Goncharov, R. Betti, P. B. Radha, T. R. Boehly, D. T. Casey, T. J. B. Collins, R. S. Craxton, J. A. Delettrez, D. H. Edgell, R. Epstein, C. J. Forrest, J. A. Frenje, D. H. Froula, M. Gatu-Johnson, V. Yu. Glebov, D. R. Harding, M. Hohenberger, S. X. Hu, I. V. Igumenshchev, R. Janezic, J. H. Kelly, T. J. Kessler, C. Kingsley, T. Z. Kosc, J. P. Knauer, S. J. Loucks, J. A. Marozas, F. J. Marshall, A. V. Maximov, R. L. McCrory, P. W. McKenty, D. D. Meyerhofer, D. T. Michel, J. F. Myatt, R. D. Petrasso, S. P. Regan, W. Seka, W. T. Shmayda, R. W. Short, A. Shvydky, S. Skupsky, J. M. Soures, C. Stoeckl, W. Theobald, V. Versteeg, B. Yaakobi, and J. D. Zuegel, Phys. Plasmas **20**, 056317 (2013).

57. T. R. Boehly, V. N. Goncharov, W. Seka, S. X. Hu, J. A. Marozas, D. D. Meyerhofer, P. M. Celliers, D. G. Hicks, M. A. Barrios, D. Fratanduono, and G. W. Collins, Phys. Plasmas **18**, 092706 (2011).

58. H. F. Robey, J. D. Moody, P. M. Celliers, J. S. Ross, J. Ralph, S. Le Pape, L. Berzak Hopkins, T. Parham, J. Sater, E. R. Mapoles, D. M. Holunga, C. F. Walters, B. J. Haid, B. J. Kozioziemski, R. J. Dylla-Spears, K. G. Krauter, G. Frieders, G. Ross, M. W. Bowers, D. J. Strozzi, B. E. Yoxall, A. V. Hamza, B. Dzenitis, S. D. Bhandarkar, B. Young, B. M. Van Wonterghem, L. J. Atherton, O. L. Landen, M. J. Edwards, and T. R. Boehly, Phys. Rev. Lett. **111**, 065003 (2013).

59. S. X. Hu, B. Militzer, V. N. Goncharov, and S. Skupsky, Phys. Rev. Lett. **104**, 235003 (2010); S. X. Hu, B. Militzer, V. N. Goncharov, and S. Skupsky, Phys. Rev. B **84**, 224109 (2011).

60. Y. Ping, A. Fernandez-Panella, H. Sio, A. Correa, R. Shepherd, O. Landen, R. A. London, P. A. Sterne, H. D. Whitley, D. Fratanduono, T. R. Boehly, and G. W. Collins, Phys. Plasmas **22**, 092701 (2015).

Demonstrating Ignition Hydrodynamic Equivalence in Direct-Drive Cryogenic Implosions on OMEGA

Introduction

The main approach to ignition by means of inertial confinement fusion (ICF)[1,2] currently pursued at the National Ignition Facility (NIF)[3] is x-ray (or indirect) drive, where the laser energy absorbed in a high-Z hohlraum is re-emitted in the form of x rays that drive the fuel capsule. In the other ICF approach—direct drive—the target is driven by laser irradiation directly coupled to the plasma blowing off the imploding capsule. The main advantage of the indirect-drive approach is reduced sensitivity of drive uniformity to short-scale beam nonuniformities. The main advantage of direct drive is a higher coupling efficiency (by factor of 3 to 5) of laser energy into kinetic energy of the shell (hydrodynamic efficiency) compared to that of x-ray drive. The OMEGA Laser System[4] and the KrF laser NIKE at the Naval Research Laboratory[5] have been the principal facilities for direct-drive experiments in the U.S.

Significant progress has been made over the last several decades in beam smoothing. This includes distributed phase plates (DPP's),[6] polarization smoothing with birefringent wedges,[7] smoothing by spectral dispersion (SSD),[8] and induced spatial incoherence.[9] In addition to these improvements, implementing adiabat shaping techniques[10,11] to significantly reduce Rayleigh–Taylor (RT) instability[12,13] growth during shell acceleration and demonstrating imprint mitigation with mid-Z–doped ablators[14] and high-Z target overcoats[15] make the direct-drive approach very attractive. The progress in direct-drive research and the challenges in achieving ignition on the NIF using x-ray drive suggests that direct drive as a viable alternative for developing a burning-plasma platform in the laboratory be considered.

Compared to x-ray drive, direct-drive targets couple a larger fraction of laser energy into shell kinetic energy and internal energy of the neutron-producing central region of the target (hot spot) at peak fuel compression. Larger hot-spot energy relaxes the requirement on shell convergence and hot-spot pressure in an igniting target. This can be shown with the help of a commonly used ignition condition according to which plasma self-heating is initiated by both PdV work and alpha-particle deposition inside the hot spot, given the product of areal density and ion temperature satisfies[1,2,16,17]

$$(\rho R)_{\rm hs} \times T \gtrsim 0.3\ {\rm g/cm}^2 \times 5\ {\rm keV}\,, \tag{1}$$

where ρ, $R_{\rm hs}$, and T are the hot-spot density, radius, and temperature, respectively. Substituting expressions for the pressure $\rho_{\rm hs} = (1 + Z)\ \rho T/m_{\rm i}$ (Z is the average ion charge and $m_{\rm i}$ is the average ion mass) and internal energy $E_{\rm hs} = 3/2\ p_{\rm hs}V_{\rm hs}$ ($V_{\rm hs}$ is the neutron-averaged hot-spot volume) into Eq. (1) gives a minimum pressure requirement (threshold) for ignition,

$$p_{\rm hs} > p_{\rm thr} = 250\ {\rm Gbar}\left(\frac{E_{\rm hs}}{10\ {\rm kJ}}\right)^{-1/2},\ \text{or}$$

$$\overline{P} = \frac{p_{\rm hs}}{p_{\rm thr}} = \left(\frac{p_{\rm hs}}{250\ {\rm Gbar}}\right)\sqrt{\frac{E_{\rm hs}}{10\ {\rm kJ}}} > 1\,, \tag{2}$$

where $\overline{P}$ is the ignition pressure parameter.

Figure 145.30 shows the dependence of the threshold pressure $p_{\rm thr}$ on the hot-spot internal energy. Spherically symmetric direct-drive cryogenic designs on OMEGA couple up

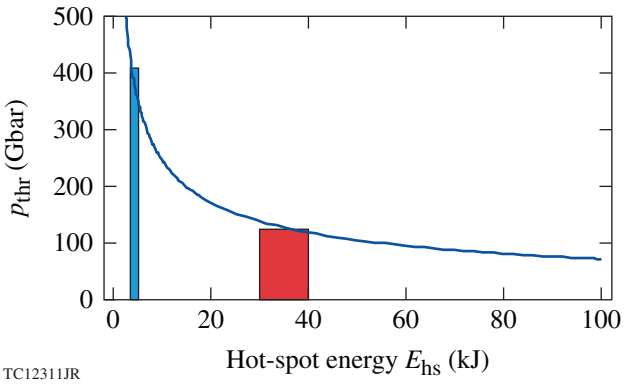

Figure 145.30
Threshold hot-spot pressure $p_{\rm thr}$ as a function of the hot-spot internal energy. A typical hot-spot energy in an indirect- and a direct-drive implosion for a National Ignition Facility (NIF)—scale laser energy is shown by the blue- and red-shaded regions, respectively.

to 0.44 kJ (out of 26-kJ incident laser energy) into the hot-spot internal energy. Hydrodynamically scaled to the NIF, with a laser energy of 1.5 MJ to 1.8 MJ, these designs are predicted to couple 5× to 10× more energy into the hot spot (25 kJ to 40 kJ, depending on laser coupling efficiency; see the red-shaded region in Fig. 145.30) compared to that of indirect drive (4 kJ to 5 kJ; see the blue-shaded region in Fig. 145.30), resulting in 2.5× to 3× lower hot-spot pressures required for ignition (~120 Gbar to 150 Gbar for direct drive versus 350 Gbar to 400 Gbar for indirect drive). The required hot-spot size also becomes smaller with a reduction in $E_{\rm hs}$. According to Eq. (2) the hot-spot size scales as a square root of the internal energy, leading to a hot-spot size that is a factor of 2.5 to 3 larger in a direct-drive implosion compared to an x-ray-drive implosion.

OMEGA Cryogenic Implosions

To separate 1-D factors limiting the target performance (drive efficiency, adiabat, etc.) from 3-D effects, a series of dedicated experiments was performed on OMEGA with the purpose of improving the accuracy of 1-D code predictions. To identify critical implosion parameters, the 1-D scaling laws for peak pressure, hot-spot energy, and the ignition-pressure parameter are written in terms of implosion velocity $v_{\rm imp}$ (defined as the peak mass-averaged shell velocity), the drive (ablation) pressure $p_{\rm abl}$, and in-flight shell adiabat α (Ref. 18),

$$p_{\rm hs}^{\rm 1\text{-}D} \sim \frac{p_{\rm abl}^{1/3}\, v_{\rm imp}^{10/3}}{\alpha},$$

$$E_{\rm hs}^{\rm 1\text{-}D} \sim E_{\rm kin}\frac{v_{\rm imp}^{4/3}}{\alpha^{2/5} p_{\rm abl}^{4/15}},$$

$$\bar{P}_{\rm 1\text{-}D} \sim \frac{\sqrt{E_{\rm kin}}\, v_{\rm imp}^{4}\, p_{\rm abl}^{1/5}}{\alpha^{6/5}}. \qquad (3)$$

The implosion velocity and shell kinetic energy $E_{\rm kin}$ are inferred in an experiment by measuring the ablation-front trajectory and mass ablation rate using self-emission imaging.[19] The ablation pressure is inferred from simulations that match the measured ablation-front trajectory, mass ablation rate, bang time,[20] and scattered-light power and spectrum.[21] Finally, the shock-induced adiabat is inferred by measuring shock velocities early in the pulse using VISAR (velocity interferometer system for any reflector).[22] An additional fuel-adiabat increase caused by hot-electron preheat is estimated by measuring the hard x-ray signal[23] and areal density[24,25] in mid- to high-adiabat implosions (the areal density in 1-D, for a given laser energy, depends mainly on the shell adiabat,[26] $\rho R \sim \alpha^{-0.5}$). The estimate of the shell-preheat effect based on the areal-density measurement is valid only for implosions with $\alpha \gtrsim 3.5$ since shell integrity and fuel compression in lower-adiabat implosions are compromised because of the short-scale mix. A detailed comparison of 1-D simulation results using the hydrocode *LILAC*[27] with the data[18] shows good agreement between the two for a variety of target designs and drive conditions. One-dimensional simulations include the nonlocal thermal-transport model,[28] the ray-based cross-beam energy transfer (CBET) model,[29] and first-principle equation-of-state models[30] for both DT ice and the CD ablator.

An analysis of direct-drive implosions on OMEGA has shown that coupling losses caused by CBET[29] significantly reduce the ablation pressure (as much as 40% on OMEGA and up to 60% on the NIF-scale targets), implosion velocity, and shell kinetic energy. Including such losses, a demonstration of the hydrodynamic equivalence of implosions on OMEGA to ignition designs on the NIF requires that the shell's in-flight aspect ratio exceed the current stability threshold level (~22) (Ref. 18). One of the CBET mitigation strategies[31] involves using laser illumination with a laser-beam diameter smaller than the initial shell diameter. This, as demonstrated both theoretically and experimentally, recovers some coupling losses and increases the ablation pressure. Since the effect of CBET is small early in the implosion, when the density scale length and laser intensity are small, beam-zooming schemes[32] can be considered when the beam's focal spot at an early time is at the initial target radius (to maximize the illumination uniformity), then reduced down to 0.6× to 0.7× of the size at the beginning of the main drive.

While the implementation of zooming on OMGEA is still a few years away, a test of the CBET reduction strategy was performed using "static" DPP's, which produces focal spots smaller than the initial target size throughout the entire drive pulse. New distributed phase plates (called SG5, after the super-Gaussian order of the focal-spot profile being close to 5) were designed and installed on OMEGA with the purpose of studying CBET mitigation techniques. These plates have a lower focal-spot nonuniformity level compared to the existing DPP's (so-called SG4). The focal-spot radius was fixed at $R_{\rm b} = 410\ \mu$m (95% of laser energy is encircled within radius $R_{\rm b}$). The ratio of $R_{\rm b}$ to target radius ($R_{\rm t}$) was changed by varying $R_{\rm t}$ from 400 μm to 500 μm. Also, on-target UV energy (available to implode larger targets) was increased by implementing multiple-pulse driver lines (MPD) on OMEGA. In the MPD mode, SSD is turned off during the main pulse, making it possible to increase the UV energy from 26 kJ up to 29 kJ. In this configuration, however, the focal spot becomes slightly elliptical (or more accurately, the 2-D super-Gaussian fit of the focal-spot profile has an azimuthal variation in

the super-Gaussian order). The azimuthally averaged focal-spot profile has $n_{SG} = 6.14$ and $R_b = 388\ \mu$m. Using the MPD configuration for larger targets with $R_t = 450\ \mu$m, 480 μm, and 500 μm and the SSD driver for targets with $R_t = 400\ \mu$m, 430 μm, and 450 μm, the ratio R_b/R_t changed from 1.025 to 0.78. According to simulation results (that matched the observables), the smallest target ($R_t = 400\ \mu$m) has a $v_{imp} = 3.5$ to 3.6×10^7 cm/s and hydrodynamic efficiency (the ratio of the shell's kinetic energy to the total laser energy) of $f_{hydro} = 3.5\%$, while the largest target has a similar implosion velocity, $v_{imp} = 3.6$ to 3.7×10^7 cm/s, but more than twice the hydroefficiency, $f_{hydro} = 7.2\%$. Such an increase in hydroefficiency is caused partially by smaller refraction losses experienced by a larger target (smaller R_b/R_t and larger density scale length) and partially by reduced CBET losses. To quantify each effect, a simulation was performed with $R_t = 500\ \mu$m, where R_b was increased to match R_t. In such a simulation, the implosion velocity was dropped by 17% to $v_{imp} = 3 \times 10^7$ cm/s and the shell's hydrodynamic efficiency was reduced by 20% down to $f_{hydro} = 5.8\%$.

Figure 145.31 shows target performance for different target diameters. The hot-spot pressure is inferred[33] by using the measured neutron yield, burn duration Δt_{burn} (using both neutron time-of-flight and framing-camera measurements of x-ray burn duration), neutron-averaged ion temperature $(T_i)_n$, and hot-spot size R_{17} (defined as the radius of 17% of the peak-emission contour for x rays in the 4-keV to 7-keV energy range) at bang time using a time-resolved Kirkpatrick–Baez framing camera.[34] Assuming an isobaric hot spot and fitting the burn history to a Gaussian with full width at half maximum (FWHM) = Δt_{burn}, the maximum burn rate N_{max} relates to neutron yield Y as $N_{max} = 2Y\sqrt{\ln 2/\pi}\,/\Delta t_{burn}$, where $N_{max} = n_T n_D T^2 \int_{V_{hs}} dV\langle\sigma v\rangle/T^2$. Therefore, pressure at bang time can be determined using

$$p_{hs} \simeq \left[8Y\sqrt{\ln 2/\pi}\,\Big/\left(f_D f_T \Delta t_{burn}\int_{V_{hs}} dV\langle\sigma v\rangle/T^2\right)\right]^{1/2}, \quad (4)$$

where $\langle\sigma v\rangle$ is the cross section for D−T reactions, and f_D and f_T are the fractions of D and T in the fuel, respectively. In evaluating the spatial integral in Eq. (4) the following spatial profile for the ion temperature (obtained using simulation results) is assumed:

$$T(r) = T_c\left[1 - \left(r/R_{hs}\right)^2\left(1 - 0.15^{3/2}\right)\right]^{2/3},$$

where T_c is the maximum hot-spot temperature, determined by matching

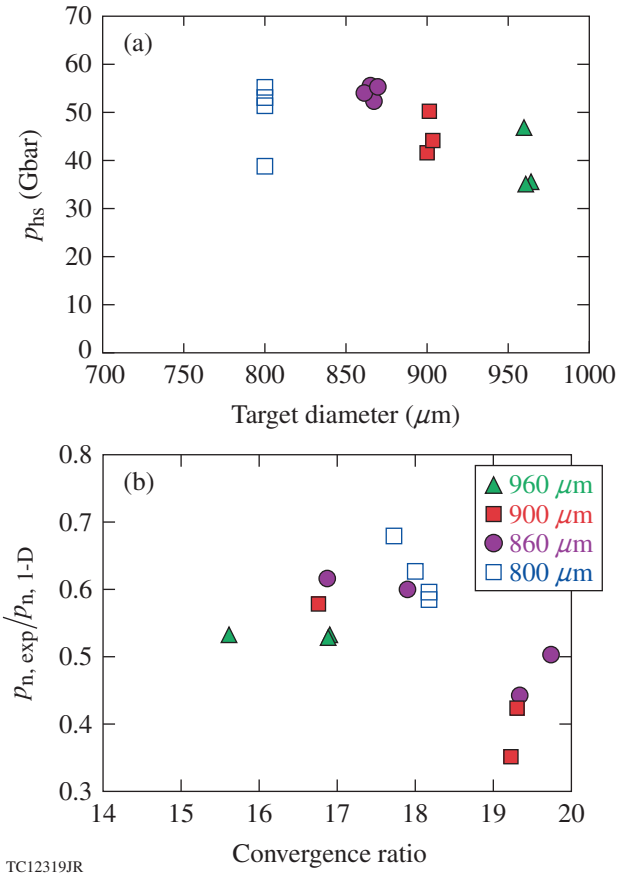

Figure 145.31
(a) Hot-spot pressure, inferred from experimental observables, as a function of target size. (b) Inferred hot-spot pressure normalized to 1-D code predictions versus the predicted shell convergence at 1-D bang time.

$$\left(\int_{V_{hs}} dV\langle\sigma v\rangle/T\right)\Big/\left(\int_{V_{hs}} dV\langle\sigma v\rangle/T^2\right)$$

with the measured $(T_i)_n$, and, as follows from code predictions, R_{hs} and measured R_{17} are related using $R_{hs} = 1.06\ R_{17}$.

The following two conclusions can be made based on results shown in Fig. 145.31: first, the hot-spot pressure (both absolute and relative to 1-D predictions) degrades with the target size; second, there is a threshold of the shell's convergence ratio, $CR^{1\text{-}D} \simeq 18$, beyond which the hot-spot pressure normalized to the 1-D prediction drops from between 0.5 to 0.7 to between 0.3 to 0.5.

To understand these trends, one must consider the effects of shell nonuniformity. The evolution of long-wavelength nonuniformities seeded by target offset, beam geometry, beam power

imbalance, and mispointing is studied using the 3-D hydrocode *ASTER*.[35] This code includes 3-D hydrodynamics, ion and electron thermal conduction (the flux-limited Spitzer model), the CBET model, bremsstrahlung radiation losses, and nuclear reactivities. A simplified 3-D model of laser deposition is used, assuming a spherical symmetry of the plasma corona in the laser-deposition region, when performing ray tracing of individual beams (this approximation is justified because of strong lateral thermal-conduction smoothing in the high-temperature corona in direct-drive implosions). The beam power, timing, and pointing, however, can vary from beam to beam.

Simulations of cryogenic implosions on OMEGA show that the bubbles (areas of low-density material from the central region that protrude into the higher-density shell) developed because of the RT growth of long-wavelength perturbations ($\ell \lesssim 5$) during shell deceleration, increasing the volume of the central region V_{cntr} and reducing the hot-spot pressure $\left(p_{\text{hs}} \sim 1/V_{\text{cntr}}^{5/3}\right)$ and neutron yield. As the shell converges further, the bubbles eventually break out of the shell, quenching hot-spot confinement and neutron yield. This is shown in Fig. 145.32. Since the burn truncates earlier because of the 3-D effects, the inferred hot-spot pressure reduces as a result of two effects: sampling and an increased volume V_{cntr} of the central region surrounded by the cold shell. Shifting the peak burn to an earlier time because of the nonuniformity growth samples earlier stages of hot-spot formation when shell convergence and the central pressure have not yet reached the peak values. The 3-D effects also increase the central region volume, preventing the fuel material from stagnating and effectively converting the shell kinetic energy into the internal energy of the hot spot. To account for the first effect (early pressure sampling), Fig. 145.33 plots the inferred hot-spot pressure normalized to the predicted pressure at the observed (earlier) bang time as a function of 1-D shell convergence calculated at the experimental bang time. Figure 145.33 shows that implosions with a fuel adiabat $\alpha > 3.5$ proceed close to 1-D predictions up to a shell convergence of CR ~ 17. Further shell convergence does not lead to additional *PdV* work on the hot spot because of the RT growth of low-ℓ modes. An additional limitation on target performance at a lower fuel adiabat is caused by compromised shell integrity resulting from short-wavelength nonuniformity growth during shell acceleration.

In summary, the cryogenic campaign with a reduced beam radius relative to the target radius $\left(R_{\text{b}}/R_{\text{t}} < 1\right)$, performed on OMEGA to reduce CBET losses, demonstrated increased laser coupling and hydrodynamic efficiency. This coupling enhancement, however, did not improve the target performance. Numerical simulations indicate that long-wavelength nonuni-

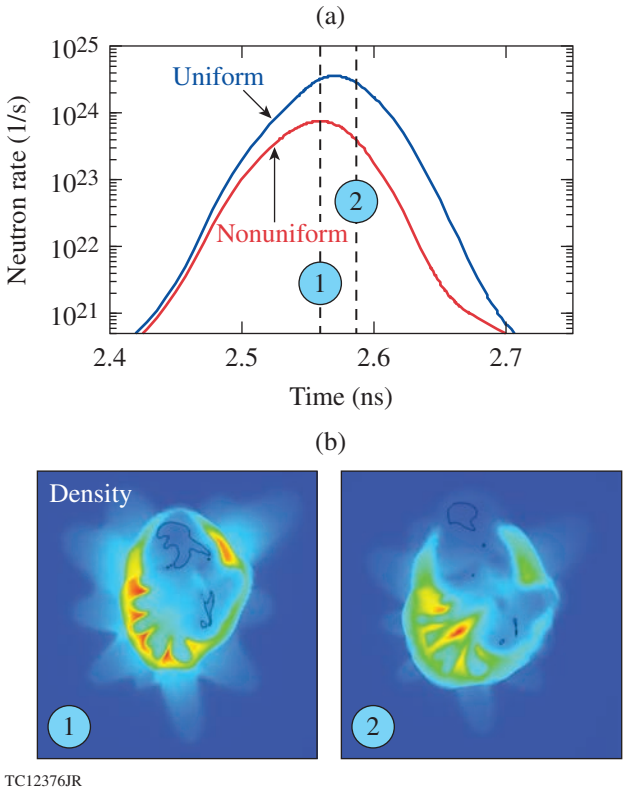

Figure 145.32
(a) Neutron-production rate calculated using the code *ASTER* without (blue solid line) and with (red solid line) the effects of long-wavelength nonuniformity growth. (b) Simulated shell density maps at times indicated by (1) and (2).

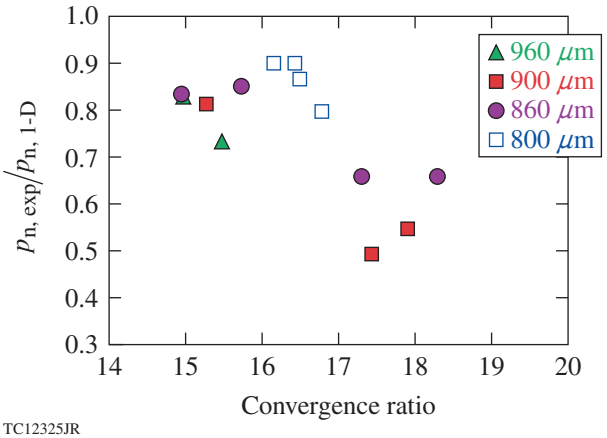

Figure 145.33
Inferred hot-spot pressure normalized to the 1-D predictions calculated at the experimental bang time versus 1-D shell convergence at the experimental bang time.

formities caused by target offset and power imbalance lead to an increased target central volume and early burn truncation. This effect is exacerbated by reduction in beam overlap when target size increases relative to beam size. Demonstrating hydrodynamic equivalence on OMEGA will require minimizing large-wavelength uniformities seeded by power imbalance and target offset and reusing target debris accumulated during cryogenic target production.

ACKNOWLEDGMENT

This material is based upon work supported by the Department of Energy National Nuclear Security Administration under Award Number DE-NA0001944, the University of Rochester, and the New York State Energy Research and Development Authority. The support of DOE does not constitute an endorsement by DOE of the views expressed in this article.

REFERENCES

1. J. D. Lindl, *Inertial Confinement Fusion: The Quest for Ignition and Energy Gain Using Indirect Drive* (Springer-Verlag, New York, 1998).
2. S. Atzeni and J. Meyer-ter-Vehn, *The Physics of Inertial Fusion: Beam Plasma Interaction, Hydrodynamics, Hot Dense Matter*, International Series of Monographs on Physics (Clarendon Press, Oxford, 2004).
3. J. Paisner *et al*., Laser Focus World **30**, 75 (1994).
4. T. R. Boehly, D. L. Brown, R. S. Craxton, R. L. Keck, J. P. Knauer, J. H. Kelly, T. J. Kessler, S. A. Kumpan, S. J. Loucks, S. A. Letzring, F. J. Marshall, R. L. McCrory, S. F. B. Morse, W. Seka, J. M. Soures, and C. P. Verdon, Opt. Commun. **133**, 495 (1997).
5. S. P. Obenschain *et al*., Phys. Plasmas **3**, 2098 (1996).
6. T. J. Kessler, Y. Lin, J. J. Armstrong, and B. Velazquez, Proc. SPIE **1870**, 95 (1993).
7. T. R. Boehly, V. A. Smalyuk, D. D. Meyerhofer, J. P. Knauer, D. K. Bradley, R. S. Craxton, M. J. Guardalben, S. Skupsky, and T. J. Kessler, J. Appl. Phys. **85**, 3444 (1999).
8. S. Skupsky, R. W. Short, T. Kessler, R. S. Craxton, S. Letzring, and J. M. Soures, J. Appl. Phys. **66**, 3456 (1989).
9. R. H. Lehmberg and J. Goldhar, Fusion Technol. **11**, 532 (1987).
10. V. N. Goncharov, J. P. Knauer, P. W. McKenty, P. B. Radha, T. C. Sangster, S. Skupsky, R. Betti, R. L. McCrory, and D. D. Meyerhofer, Phys. Plasmas **10**, 1906 (2003).
11. V. N. Goncharov, T. C. Sangster, T. R. Boehly, S. X. Hu, I. V. Igumenshchev, F. J. Marshall, R. L. McCrory, D. D. Meyerhofer, P. B. Radha, W. Seka, S. Skupsky, C. Stoeckl, D. T. Casey, J. A. Frenje, and R. D. Petrasso, Phys. Rev. Lett. **104**, 165001 (2010).
12. S. Chandrasekhar, in *Hydrodynamic and Hydromagnetic Stability*, International Series of Monographs on Physics (Clarendon Press, Oxford, 1961), p. 428.
13. J. Sanz, Phys. Rev. Lett. **73**, 2700 (1994); V. N. Goncharov, R. Betti, R. L. McCrory, P. Sorotokin, and C. P. Verdon, Phys. Plasmas **3**, 1402 (1996).
14. S. X. Hu, G. Fiksel, V. N. Goncharov, S. Skupsky, D. D. Meyerhofer, and V. A. Smalyuk, Phys. Rev. Lett. **108**, 195003 (2012).
15. S. P. Obenschain *et al*., Phys. Plasmas **9**, 2234 (2002).
16. R. Betti, P. Y. Chang, B. K. Spears, K. S. Anderson, J. Edwards, M. Fatenejad, J. D. Lindl, R. L. McCrory, R. Nora, and D. Shvarts, Phys. Plasmas **17**, 058102 (2010).
17. R. Betti, K. Anderson, V. N. Goncharov, R. L. McCrory, D. D. Meyerhofer, S. Skupsky, and R. P. J. Town, Phys. Plasmas **9**, 2277 (2002).
18. V. N. Goncharov, T. C. Sangster, R. Betti, T. R. Boehly, M. J. Bonino, T. J. B. Collins, R. S. Craxton, J. A. Delettrez, D. H. Edgell, R. Epstein, R. K. Follet, C. J. Forrest, D. H. Froula, V. Yu. Glebov, D. R. Harding, R. J. Henchen, S. X. Hu, I. V. Igumenshchev, R. Janezic, J. H. Kelly, T. J. Kessler, T. Z. Kosc, S. J. Loucks, J. A. Marozas, F. J. Marshall, A. V. Maximov, R. L. McCrory, P. W. McKenty, D. D. Meyerhofer, D. T. Michel, J. F. Myatt, R. Nora, P. B. Radha, S. P. Regan, W. Seka, W. T. Shmayda, R. W. Short, A. Shvydky, S. Skupsky, C. Stoeckl, B. Yaakobi, J. A. Frenje, M. Gatu-Johnson, R. D. Petrasso, and D. T. Casey, Phys. Plasmas **21**, 056315 (2014).
19. D. T. Michel, C. Sorce, R. Epstein, N. Whiting, I. V. Igumenshchev, R. Jungquist, and D. H. Froula, Rev. Sci. Instrum. **83**, 10E530 (2012).
20. C. Stoeckl, V. Yu. Glebov, S. Roberts, T. C. Sangster, R. A. Lerche, R. L. Griffith, and C. Sorce, Rev. Sci. Instrum. **74**, 1713 (2003).
21. W. Seka, D. H. Edgell, J. P. Knauer, J. F. Myatt, A. V. Maximov, R. W. Short, T. C. Sangster, C. Stoeckl, R. E. Bahr, R. S. Craxton, J. A. Delettrez, V. N. Goncharov, I. V. Igumenshchev, and D. Shvarts, Phys. Plasmas **15**, 056312 (2008).
22. L. M. Barker and R. E. Hollenbach, J. Appl. Phys. **43**, 4669 (1972).
23. C. Stoeckl, V. Yu. Glebov, D. D. Meyerhofer, W. Seka, B. Yaakobi, R. P. J. Town, and J. D. Zuegel, Rev. Sci. Instrum. **72**, 1197 (2001).
24. J. A. Frenje, C. K. Li, F. H. Séguin, D. T. Casey, R. D. Petrasso, T. C. Sangster, R. Betti, V. Yu. Glebov, and D. D. Meyerhofer, Phys. Plasmas **16**, 042704 (2009).
25. C. J. Forrest, P. B. Radha, V. Yu. Glebov, V. N. Goncharov, J. P. Knauer, A. Pruyne, M. Romanofsky, T. C. Sangster, M. J. Shoup III, C. Stoeckl, D. T. Casey, M. Gatu-Johnson, and S. Gardner, Rev. Sci. Instrum. **83**, 10D919 (2012).
26. R. Betti and C. Zhou, Phys. Plasmas **12**, 110702 (2005).
27. J. Delettrez, R. Epstein, M. C. Richardson, P. A. Jaanimagi, and B. L. Henke, Phys. Rev. A **36**, 3926 (1987).
28. V. N. Goncharov, T. C. Sangster, P. B. Radha, R. Betti, T. R. Boehly, T. J. B. Collins, R. S. Craxton, J. A. Delettrez, R. Epstein, V. Yu. Glebov, S. X. Hu, I. V. Igumenshchev, J. P. Knauer, S. J. Loucks, J. A. Marozas, F. J. Marshall, R. L. McCrory, P. W. McKenty, D. D.

Meyerhofer, S. P. Regan, W. Seka, S. Skupsky, V. A. Smalyuk, J. M. Soures, C. Stoeckl, D. Shvarts, J. A. Frenje, R. D. Petrasso, C. K. Li, F. Séguin, W. Manheimer, and D. G. Colombant, Phys. Plasmas **15**, 056310 (2008).

29. I. V. Igumenshchev, D. H. Edgell, V. N. Goncharov, J. A. Delettrez, A. V. Maximov, J. F. Myatt, W. Seka, A. Shvydky, S. Skupsky, and C. Stoeckl, Phys. Plasmas **17**, 122708 (2010).

30. S. X. Hu, B. Militzer, V. N. Goncharov, and S. Skupsky, Phys. Rev. Lett. **104**, 235003 (2010); S. X. Hu, L. A. Collins, V. N. Goncharov, J. D. Kress, R. L. McCrory, and S. Skupsky, Phys. Rev. E **92**, 043104 (2015).

31. I. V. Igumenshchev, D. H. Froula, D. H. Edgell, V. N. Goncharov, T. J. Kessler, F. J. Marshall, R. L. McCrory, P. W. McKenty, D. D. Meyerhofer, D. T. Michel, T. C. Sangster, W. Seka, and S. Skupsky, Phys. Rev. Lett. **110**, 145001 (2013).

32. D. H. Froula, T. J. Kessler, I. V. Igumenshchev, R. Betti, V. N. Goncharov, H. Huang, S. X. Hu, E. Hill, J. H. Kelly, D. D. Meyerhofer, A. Shvydky, and J. D. Zuegel, Phys. Plasmas **20**, 082704 (2013).

33. C. Cerjan, P. T. Springer, and S. M. Sepke, Phys. Plasmas **20**, 056319 (2013).

34. F. J. Marshall, V. N. Goncharov, V. Yu. Glebov, S. P. Regan, T. C. Sangster, and C. Stoeckl, the Ninth International Conference on Inertial Fusion Sciences and Applications (IFSA 2015), Seattle, WA, 20–25 September 2015 (Paper Th.Po.17).

35. I. V. Igumenshchev, V. N. Goncharov, F. J. Marshall, J. P. Knauer, D. H. Froula, and S. P. Regan, "Three-Dimensional Modeling of Direct-Drive Cryogenic Implosions," submitted to Physics of Plasmas.

A Neutron Temporal Diagnostic for High-Yield DT Cryogenic Implosions on OMEGA

Introduction

The temporal history of the neutron production in inertial confinement fusion (ICF) experiments[1] is an important diagnostic signature. In ICF experiments, shells filled with deuterium (D_2) or a deuterium–tritium (DT) mixture are compressed by either direct laser illumination,[2] soft x-ray radiation in a laser-heated hohlraum,[3] or strong magnetic fields[4] to conditions under which thermonuclear fusion occurs. The temporal width of the neutron signal is usually of the order of 100 ps. Experimental signatures from the temporal history of the neutron production are the rising edge of the measured neutron rate, which is influenced by the shock transit through the capsule;[5] the peak of the neutron rate (bang time),[6] a measure of the energy absorbed in the imploding shell; and the trailing edge of the neutron rate that encodes information about material mixing during the stagnation phase of the implosion.[7]

Time-resolved neutron measurements on ICF experiments generally use either a scintillator to convert the neutron energy into visible light[8] or chemical-vapor–deposition (CVD) diamond detectors,[9] which convert the neutron energy directly into an electrical charge. The light from the scintillator is either converted into an electrical signal using a fast photomultiplier tube (PMT) or recorded on a fast optical streak camera.[10,11] The PMT or CVD-based neutron bang-time diagnostics[12–16] do not have the temporal resolution to resolve the details of the neutron pulse; they measure solely the neutron bang time. Only the streak-camera–based neutron temporal diagnostics (NTD's)[10,11] are capable of resolving the details of the neutron temporal history.

High-performance, layered cryogenic DT implosions[17] on the OMEGA laser[18] at the Laboratory for Laser Energetics (LLE) present a particular challenge in measuring the neutron history because of the high-DT neutron yields (~5×10^{13}) and a short neutron-production width (of the order of ~50 ps). The size of the cryogenic target shroud system[11] prevents the placement of the scintillator of the NTD system sufficiently close to the target to minimize Doppler broadening of the neutron pulse, which severely compromises the time resolution of the NTD.[10] A dedicated cryogenic-compatible neutron temporal diagnostic (cryoNTD) was developed at LLE to provide high-resolution neutron-emission measurements for D_2-filled cryogenic implosions,[11] but the placement of the streak camera close to the target chamber prevents recording data at high-DT yields because of the excessive neutron background. This article describes the setup of a new NTD system at LLE designed for high-performance, layered DT cryogenic implosions mounted in port P11 of the OMEGA target chamber (P11-NTD). The next section presents the setup of this system. The scintillator can be inserted as close as 9 cm from the target in cryogenic experiments without interfering with the cryogenic target systems. The streak camera is placed in a well-shielded location >10 m from the target, with an ~16-m-long optical relay system transporting the optical signal from the scintillator to the streak camera. The remaining sections report on the performance of the shielding setup, present the temporal impulse-response calibration procedure of the P11-NTD system, and analyze the first experimental results.

Setup of the Detector System

A CAD drawing of the P11-NTD system setup is shown in Fig. 145.34. The front-end scintillator insertion mechanism is a re-entrant into the OMEGA target chamber. A 6-mm-diam, 1-mm-thick plastic scintillator (Bicron BC422) (Ref. 19) is placed in a tungsten-alloy–shielded nose cone,[10] which can be inserted between 2 cm and 25 cm from the target. The first section of the optical relay system is housed inside the front end. The second section of the optical relay, the Target Bay wall periscope, is mounted to the OMEGA Target Bay shield wall. The optical path then leads from the OMEGA building into the OMEGA EP plenum, where the Rochester Optical Streak System (ROSS)[20] camera is mounted on an optical table.

1. Neutron Shielding

Historically, the streak camera of an NTD system has been placed close to the target chamber to minimize the length of the optical relay system.[10,11] This approach works very well for moderate yields (<1×10^{13} neutrons) but does not provide enough shielding to suppress the backgrounds for the high-DT neutron yields (up to 5×10^{13}) produced in cryogenic DT

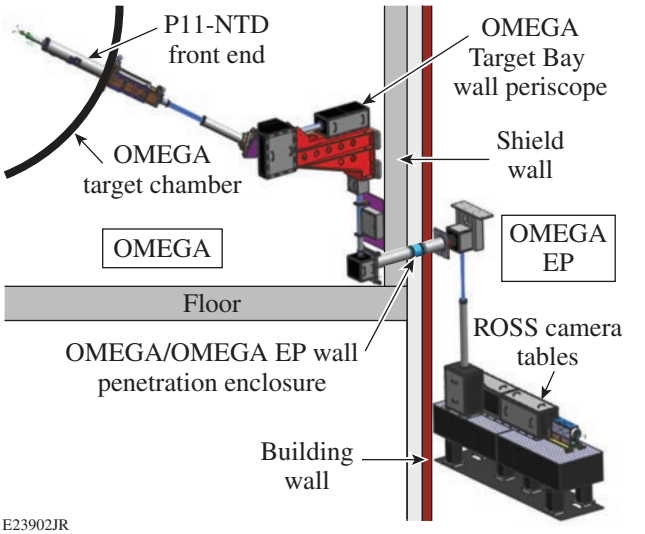

Figure 145.34
A CAD drawing of the P11-NTD (neutron-temporal-diagnostic) detector system integrated into the Omega Laser Facility. A front-end system re-entrant into the target chamber positions the scintillator distances between 2 to 25 cm from the target. An optical relay partially housed in the Target Bay wall periscope structure transports the scintillator light through a penetration in the OMEGA shield wall to a ROSS streak camera in the OMEGA EP plenum.

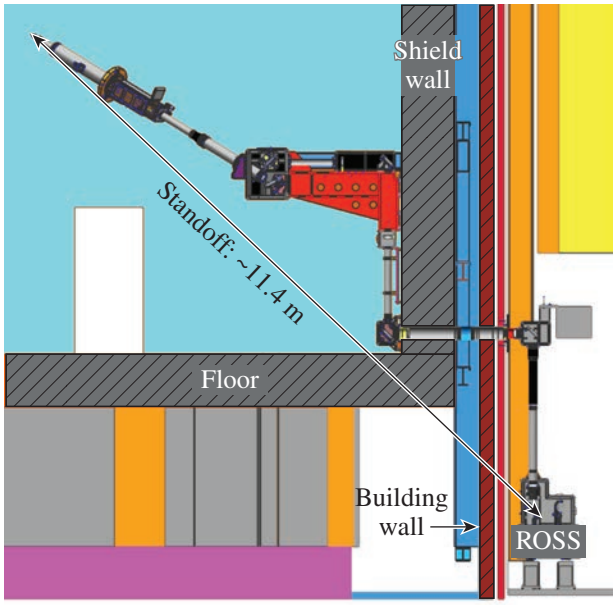

Figure 145.35
A CAD drawing of the P11-NTD shielding setup. The ROSS streak camera is placed 11.4 m from the target. The 60-cm-thick OMEGA target area floor and 80-cm-thick Target Bay shield wall provide most of the neutron shielding.

implosions on OMEGA.[17] To improve the shielding, the streak camera for the P11-NTD was placed behind the primary shield wall of the OMEGA target area in the OMEGA EP plenum (see Fig. 145.35). This location provides a standoff distance to the target of ~11.4 m, with ~1.7 m of concrete in the direct line of sight, which penetrates the OMEGA Target Bay floor, the OMEGA Target Bay retaining wall, and a brick facing wall. It is well known that the performance of a neutron shielding system depends not only on the shielding thickness in the direct line of sight, but also on the number and area of openings such as doors and holes in the shielded volume, which allow scattered neutrons to escape the target area.[21] Since there is a large ~1-m-diam hole under the target chamber, an ~1-m-diam beam tube that carries the OMEGA EP laser pulse from OMEGA EP to OMEGA for joint experiments,[22] and a number of doors into the room under the target area, the performance of this shielding will be worse than a simple estimate using the thickness of the direct line of sight would indicate.

2. Optical System

With the location of the streak camera in a separate building, a relatively complex 16.2-m-long optical path had to be designed. The light collection and transfer system (Fig. 145.36) transports the light from the scintillator to the input plane of ROSS. A fast three-element *f*/2 lens system collects the light from the scintillator with high efficiency. An optical system using a movable

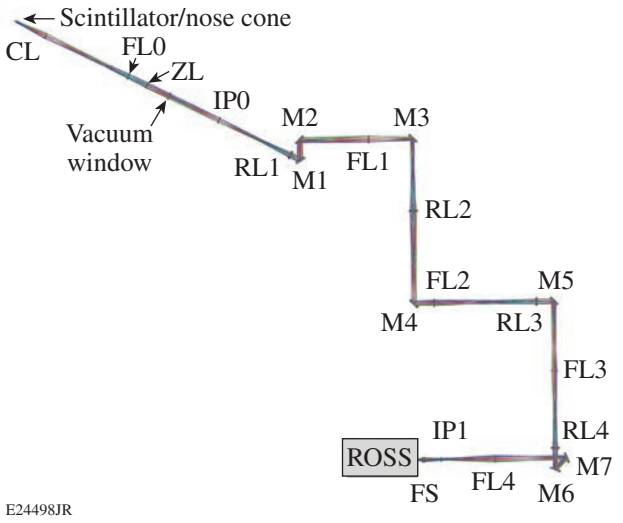

Figure 145.36
A drawing of the optical layout of the relay optics. A fast three-element *f*/2 lens system collects (CL) the light from the scintillator. A zoom (ZL) and field lens (FL0) relay the light through the vacuum window to an intermediate image plane (IP0). A four-stage optical relay, each consisting of an achromatic relay lens (RL1–4) and a field lens (FL1–4), transports the light from the first intermediate image using seven mirrors (M1–M7) to a second image plane (IP1). A three-element focus lens system (FS) focuses the light onto the slit of the streak camera.

zoom lens and a field lens relays the light from the scintillator to an intermediate image plane outside the target chamber. The location of the zoom lens is adjusted to keep the location of the intermediate image plane fixed. A four-stage optical relay, each consisting of an achromatic relay lens and a field lens, transports the light from the first intermediate image plane to an image plane close to the ROSS camera on the optical table in the OMEGA EP building. A three-element achromatic *f*/4 lens system focuses the light from the last image plane onto the photocathode of the ROSS. Since the optical path is not a straight line, seven turning mirrors were required to relay the light from the target chamber through the OMEGA shield wall into the OMEGA EP building. High-quality broadband antireflective (AR) coatings were used on the lenses with a typical loss of ~0.3% per surface, at normal incidence and dielectric high-reflective (HR) coatings were used on the mirrors with a reflectivity of >98.5% over the full spectral width of the scintillator emission from ~350 nm to 450 nm (Ref. 19). The total transmission of the system was estimated to be ~55%, with ~20% losses in the lens material, ~25% in the AR coatings as a result of the incident angular range, and ~10% in the HR coatings.

Even though the optical system is corrected for chromatic aberrations, the chromatic velocity dispersion caused by the change in index of refraction with wavelength will introduce a broadening of the impulse response. Using published values for the index of refraction[23] of the glasses used in the optical system, this effect was estimated for the optical ray passing through the center of all optics to broaden the full width at half maximum (FWHM) of the instrument response by ~8 ps given the spectrum of the scintillator light emission. This value should be considered an upper limit since most of the light passes through thinner glass than the center ray and consequently experiences less chromatic velocity dispersion.

In addition to the signal from the scintillator, light from the OMEGA fiducial system is delivered via an optical fiber and imaged onto the streak camera using an optical system internal to the ROSS camera. The OMEGA fiducial consists of a series of eight pulses spaced 548 ps apart and is amplified separately from the main laser pulse, split, and distributed to various diagnostic instruments for precision timing. This fiducial is also recorded on the P510 ultraviolet streak camera,[24] which measures the laser pulse shape. The common optical fiducial serves as a reference for both the neutron signal and the laser pulse, thereby enabling accurate timing of the NTD signal.

A similar system to the one that images the OMEGA fiducial on the photocathode is used to image the light from a 2-GHz comb generator onto the ROSS photocathode. The signal from this comb generator can be used to linearize the sweep speed of the streak camera.

Shielding Performance

Figure 145.37(a) shows the charge-coupled–device (CCD) image recorded by the P11-NTD diagnostics from a high-yield DT cryo shot (2.6×10^{13} neutrons). Four of the eight fiducial pulses are visible at the top of the image and six of the pulses from the 2-GHz comb generator are seen at the bottom. The CCD image shows very little background compared to the CCD image recorded with the previous-generation NTD system, called H5-NTD [see Fig. 145.38(a)], at the same yield level. The H5-NTD diagnostic also uses a ROSS streak camera, which is mounted ~3 m from the target in the Target Bay, shielded by 50 cm of CH in the direct line of sight and 10 cm of CH in all other directions. Figures 145.37(b) and 145.38(b) show the respective horizontal lineouts through the signals summed over the whole vertical width. Since the scintillator has a very fast rise time of <20 ps and a decay time of ~1.2 ns, the neutron-

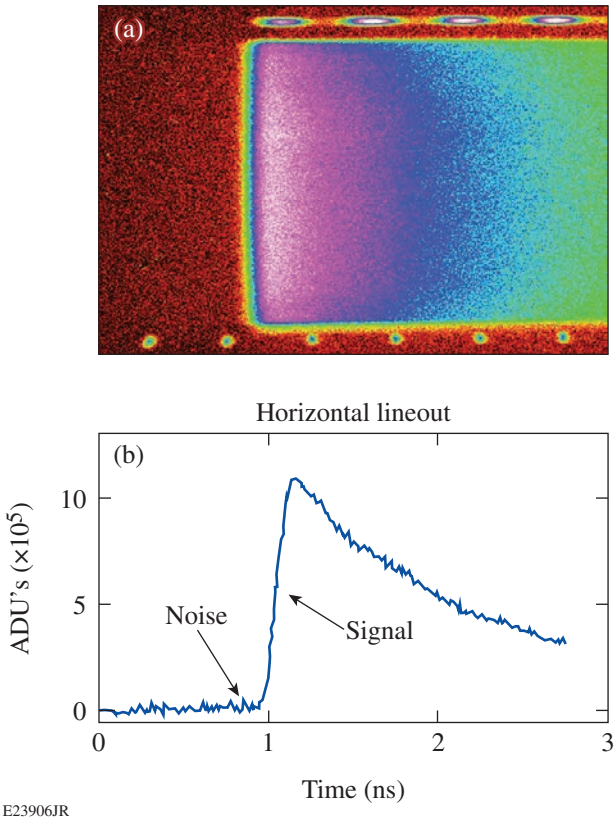

Figure 145.37
(a) A charge-coupled–device (CCD) image from P11-NTD from a high-yield DT cryo shot (2.6×10^{13} neutrons) and (b) a horizontal lineout through the signal summed over the whole vertical width in analog digital units (ADU's).

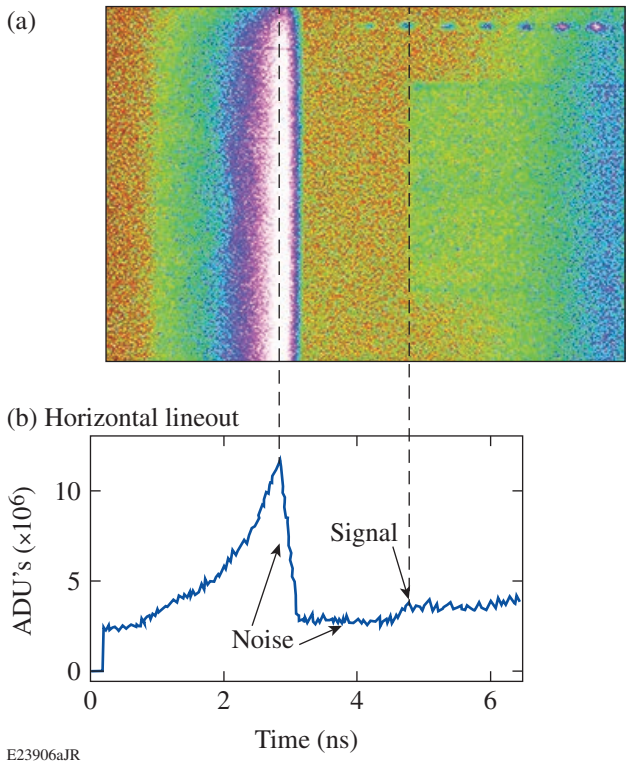

Figure 145.38

(a) A CCD image from H5-NTD from a high-yield DT cryo shot (2.6×10^{13} neutrons) and (b) horizontal lineout through the signal summed over the entire vertical width.

production history information is encoded in the leading edge of the pulse. The most-prominent feature of the background on the H5-NTD signal is a spike at ~2.5 ns, which is most likely caused by scattered neutron background present during the retrace of the streak, which starts a few microseconds after the sweep. The signal-to-noise on the P11-NTD system is ~50, which is an ~200× improvement over H5-NTD with a signal-to-noise ratio of ~0.25 at this yield level. As expected, this improvement is less than the difference the line-of-sight shielding and solid angle (10× improvement resulting from distance) would indicate.

Impulse-Response Calibration

The impulse response of the full P11-NTD including the scintillator, optical transport, and streak camera was measured using x rays from a target illuminated by a short laser pulse (10 ps) from OMEGA EP (see Fig. 145.39). The shielding from the 2-mm-thick tungsten alloy nose cone allows only hard x rays (>200 keV) to interact with the scintillator. Hard x rays are a reasonable substitute for neutrons to generate light in the scintillator because they interact mostly via Compton scattering in the CH scintillator substrate, which generates fast electrons.

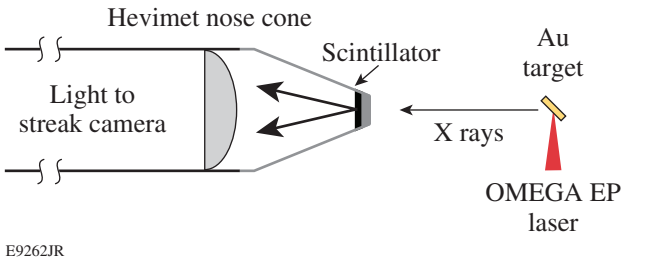

Figure 145.39

Setup of the calibration of the P11-NTD impulse response using x rays from an Au target illuminated by a short OMEGA EP laser pulse (10 ps). The 2-mm-thick Hevimet nose cone allows only hard x rays (>200 keV) to interact with the scintillator.

These >100-keV electrons generate electron-hole pairs similar to the MeV protons produced by the elastic scattering from an incident neutron. Even though the electron-hole pair density for the fast electron is significantly lower than that for a proton because of the difference in stopping power, it is a better substitute for neutron interaction relative to the excitation of the scintillator by UV irradiation, which interacts mostly with the dyes in the scintillator.[25]

For calibration, the OMEGA EP laser was defocused to spot sizes between 150 and 175 μm and the pulse energy was reduced to ~400 J to optimize the signal on the P11-NTD streak camera. The target was an Au foil of $500 \times 500 \times 10$-μm size. Figure 145.40(a) shows the temporal history of the signal from four laser shots with different focal-spot conditions for a 3-ns streak-camera sweep window. This signal is obtained by removing the effect of the long scintillator decay from the recorded signal using a "physical-modeling" approach for the deconvolution.[11] The signal n_i at the pixel location i is given as the recorded signal s_i minus the sum of all earlier neutron signals, which decay exponentially at the scintillator fall time τ, with Δt_p as the time separation of two pixels:

$$n_i = s_i - \sum_{j=0}^{i-1} n_j \exp\left[\frac{(i-j)\times \Delta t_p}{\tau}\right]. \quad (1)$$

The signals from the x-ray calibration show a stable center section of approximately Gaussian shape with a FWHM of ~50±2 ps, as well as a shoulder (at the start of the signal) and a tail, which both vary with focus condition [see Fig. 145.40(a)]. The shoulder ahead of the main pulse is most likely caused by Cherenkov radiation from MeV Compton-scattered electrons in the *f*/2 collection system since a MeV electron gains ~20 ps/cm on light in glass. The tail after the pulse could be from subrela-

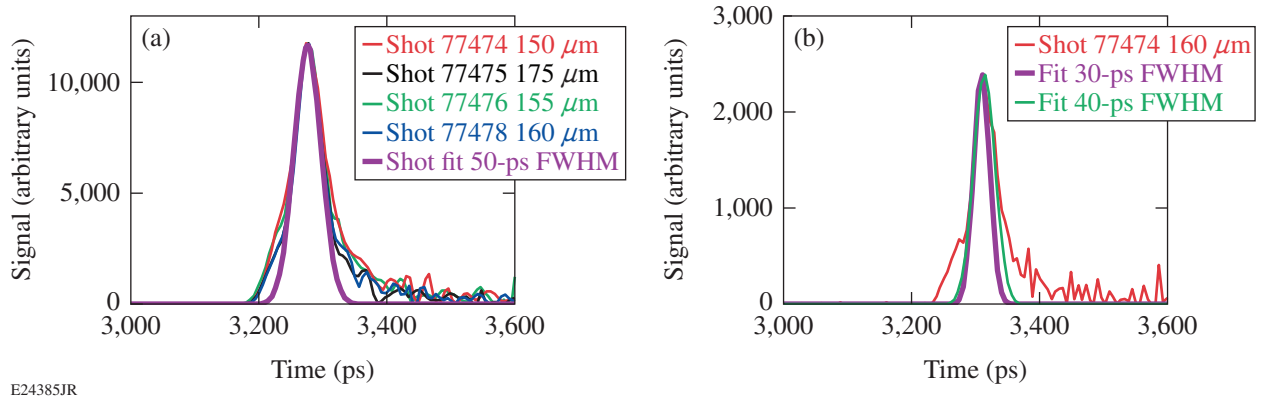

Figure 145.40
(a) Unfolded P11-NTD signals from the impulse response calibrations with a 3-ns sweep window at different focus conditions of the short-pulse laser. A 50-ps FWHM Gaussian fit matches the central part of the signal well. (b) Unfolded P11-NTD signals from the impulse response calibrations with a 1.5-ns sweep window; both a 30-ps and a 40-ps Gaussian are shown.

tivistic electrons generated in the laser–target interaction hitting the high-Z nose cone, generating hard x-ray bremsstrahlung. Both of these effects should scale with laser intensity since the slope of the electron energy distribution should be steeper for a lower laser intensity, which corresponds to a lower number of high- and medium-energy electrons.

A single shot was taken with a faster sweep speed corresponding to a 1.5-ns sweep window [see Fig. 145.40(b)]. Because of the degraded signal-to-noise, a stable fit of a Gaussian to the peak of the signal is no longer possible; several different fits with 30- to 40-ps FHWM are consistent with the data.

To infer the impulse response of the P11-NTD system, the width of the x-ray pulse must be subtracted. Since there is no independent measurement of the x-ray pulse duration, simple estimates must be used. A good estimate of the minimum x-ray pulse duration is ~15 ps because the laser pulse is ~10 ps long and the hot electrons generated in the laser–target interaction typically have a lifetime of a few picoseconds.[26] The maximum pulse duration cannot be longer than the shortest measured pulse duration with the 1.5-ns sweep of ~35 ps. Consequently, a reasonable estimate of the x-ray pulse duration is 25±10 ps. Subtracting the x-ray pulse in quadrature from the measured FWHM of the signal yields an impulse response of ~40±10 ps for the 3-ns sweep window and ~25±10 ps for the 1.5-ns sweep window, respectively.

Data Analysis

Figure 145.41 shows the inferred neutron rate from the deconvolved P11-NTD signal recorded on a recent DT cryogenic implosion on OMEGA with a neutron yield of ~4×10^{13}. The measured neutron temporal history is broadened by several

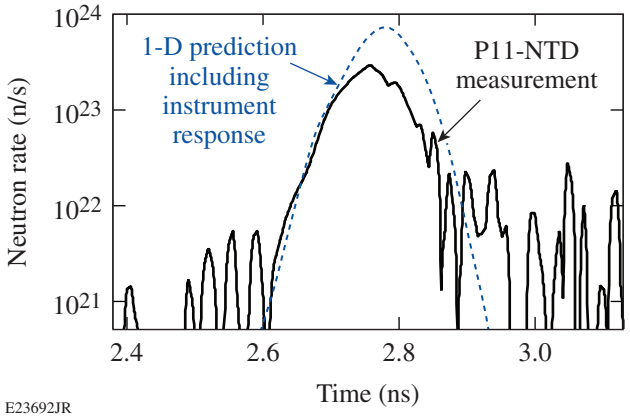

Figure 145.41
Unfolded P11-NTD signal from a high-yield cryo shot (neutron yield of ~4×10^{13}), compared to results from 1-D *LILAC* hydro simulations.

different mechanisms, which must be subtracted to measure the actual width of the neutron pulse from the target. Broadening the neutron energy spectrum caused by the high temperature of the thermonuclear plasma leads to an arrival time spread in the scintillator for DT neutrons:[10]

$$\Delta t_T^{\mathrm{DT}} = 122\sqrt{T} \times d\,, \tag{2}$$

where Δt_T^{DT} is the FWHM of the spread in picoseconds, d is the target-to-detector distance in meters, and T is the neutron-averaged ion temperature in keV. For a 10-cm distance of the P11-NTD scintillator to the target, this effect broadens the signal by ~25 ps at a 4-keV ion temperature, which is typical for most of the high-yield cryo implosions on OMEGA. Additionally, the finite neutron transit time through the scintil-

lator $\Delta t_s = \Delta x / v_n$ broadens the signal by $\Delta t_s^{DT} = 20$ ps for a scintillator thickness of $\Delta x = 1$ mm and a DT neutron speed of $v_n = 5.12$ cm/ns. Since the shape of the neutron rate is not far from a Gaussian, the impulse response of the instrument, the thermal broadening, and the transit time spread can be subtracted from the measured FWHM of the signal in quadrature to infer the actual neutron pulse width. For a measured FWHM of the neutron signal of 82±2 ps, the resultant neutron pulse width is calculated to be 65±6 ps.

An alternative method of interpreting the experimental data is to convolve the calculated neutron rate from a simulation with the experimental broadening and compare it to the measured signal. Figure 145.41 compares the results of a 1-D *LILAC* simulation of the cryogenic implosion[17] convolved with the experimental broadening and the P11-NTD data. Since the absolute timing of the NTD instruments is typically of the order of 50 ps (Ref. 11), the simulation data were shifted by ~20 ps to better align with the rising edge of the experimental data. The simulation matches the experimental data very well on the rising edge over more than one order of magnitude in neutron rate. The experimental and simulated neutron rates start to deviate from each other close to the peak of the neutron pulse, with the experimental rate significantly lower than the simulation. This deviation is believed to be caused by 3-D effects, which mix cold material into the hot core plasma, quenching the neutron-production rate earlier than expected in the 1-D simulations.[7]

Summary and Outlook

A new neutron temporal diagnostic (P11-NTD) has been developed to measure the temporal history of the neutron production in high-yield, high-performance cryogenic DT implosions on OMEGA. The ROSS streak camera recording system was placed ~11 m from target chamber center behind the primary shield wall, which reduced the neutron background by a factor of ~200. The remote location of the streak camera required the construction of a complex 16.2-m-long image relay to transport the light from the scintillator to the streak camera. The impulse response of the P11-NTD system was measured using hard x rays generated from the interaction of the 10-ps OMEGA EP laser pulse with an Au target. With the standard 3-ns sweep window an impulse response of ~40±10 ps was inferred, which makes it possible to measure ~65-ps FWHM neutron pulses with an accuracy of ~10%. Preliminary measurements of the impulse response of the system using a 1.5-ns sweep window showed an improved impulse response of ~25±10 ps, which would enable the P11-NTD to measure ~50-ps FWHM neutron pulses with ~10% accuracy once this mode of operation is fully validated.

The technique of placing the streak camera of a NTD system outside the bioshield could be relatively easily adapted to larger ICF facilities like the National Ignition Facility (NIF)[27] or Laser Mégajoule (LMJ).[28] With a typical distance of the shield wall of ~15 m from the target, an NTD on these facilities would need an ~20-m-long optical relay, which could be designed without compromising the temporal resolution. Given the much-higher neutron yields at the NIF or LMJ, the constraints on the optical transmission of the relay system are significantly relaxed and a narrowband (2- to 10-nm) optical filter at the peak of the scintillator emission spectrum could be used to minimize the chromatic group velocity dispersion.

ACKNOWLEDGMENT

This material is based upon work supported by the Department of Energy National Nuclear Security Administration under Award Number DE-NA0001944, the University of Rochester, and the New York State Energy Research and Development Authority. The support of DOE does not constitute an endorsement by DOE of the views expressed in this article.

REFERENCES:

1. J. H. Nuckolls, Phys. Today **35**, 24 (1982).
2. R. S. Craxton, K. S. Anderson, T. R. Boehly, V. N. Goncharov, D. R. Harding, J. P. Knauer, R. L. McCrory, P. W. McKenty, D. D. Meyerhofer, J. F. Myatt, A. J. Schmitt, J. D. Sethian, R. W. Short, S. Skupsky, W. Theobald, W. L. Kruer, K. Tanaka, R. Betti, T. J. B. Collins, J. A. Delettrez, S. X. Hu, J. A. Marozas, A. V. Maximov, D. T. Michel, P. B. Radha, S. P. Regan, T. C. Sangster, W. Seka, A. A. Solodov, J. M. Soures, C. Stoeckl, and J. D. Zuegel, Phys. Plasmas **22**, 110501 (2015).
3 O. A. Hurricane, D. A. Callahan, D. T. Casey, E. L. Dewald, T. R. Dittrich, T. Döppner, M. A. Barrios Garcia, D. E. Hinkel, L. F. Berzak Hopkins, P. Kervin, J. L. Kline, S. Le Pape, T. Ma, A. G. MacPhee, J. L. Milovich, J. Moody, A. E. Pak, P. K. Patel, H.-S. Park, B. A. Remington, H. F. Robey, J. D. Salmonson, P. T. Springer, R. Tommasini, L. R. Benedetti, J. A. Caggiano, P. Celliers, C. Cerjan, R. Dylla-Spears, D. Edgell, M. J. Edwards, D. Fittinghoff, G. P. Grim, N. Guler, N. Izumi, J. A. Frenje, M. Gatu Johnson, S. Haan, R. Hatarik, H. Herrmann, S. Khan, J. Knauer, B. J. Kozioziemski, A. L. Kritcher, G. Kyrala, S. A. Maclaren, F. E. Merrill, P. Michel, J. Ralph, J. S. Ross, J. R. Rygg, M. B. Schneider, B. K. Spears, K. Widmann, and C. B. Yeamans, Phys. Plasmas **21**, 056314 (2014).
4. M. R. Gomez *et al*., Phys. Plasmas **22**, 056306 (2015).
5. J. A. Frenje, C. K. Li, F. H. Séguin, J. Deciantis, S. Kurebayashi, J. R. Rygg, R. D. Petrasso, J. Delettrez, V. Yu. Glebov, C. Stoeckl, F. J. Marshall, D. D. Meyerhofer, T. C. Sangster, V. A. Smalyuk, and J. M. Soures, Phys. Plasmas **11**, 2798 (2004).
6. I. V. Igumenshchev, W. Seka, D. H. Edgell, D. T. Michel, D. H. Froula, V. N. Goncharov, R. S. Craxton, L. Divol, R. Epstein, R. Follett, J. H. Kelly, T. Z. Kosc, A. V. Maximov, R. L. McCrory, D. D. Meyerhofer, P. Michel, J. F. Myatt, T. C. Sangster, A. Shvydky, S. Skupsky, and C. Stoeckl, Phys. Plasmas **19**, 056314 (2012).

7. P. B. Radha, T. J. B. Collins, J. A. Delettrez, Y. Elbaz, R. Epstein, V. Yu. Glebov, V. N. Goncharov, R. L. Keck, J. P. Knauer, J. A. Marozas, F. J. Marshall, R. L. McCrory, P. W. McKenty, D. D. Meyerhofer, S. P. Regan, T. C. Sangster, W. Seka, D. Shvarts, S. Skupsky, Y. Srebro, and C. Stoeckl, Phys. Plasmas **12**, 056307 (2005).

8. G. F. Knoll, *Radiation Detection and Measurement*, 4th ed. (John Wiley, Hoboken, NJ, 2010).

9. G. J. Schmid, R. L. Griffith, N. Izumi, J. A. Koch, R. A. Lerche, M. J. Moran, T. W. Phillips, R. E. Turner, V. Yu. Glebov, T. C. Sangster, and C. Stoeckl, Rev. Sci. Instrum. **74**, 1828 (2003).

10. R. A. Lerche, D. W. Phillion, and G. L. Tietbohl, Rev. Sci. Instrum. **66**, 933 (1995).

11. C. Stoeckl, V. Yu. Glebov, S. Roberts, T. C. Sangster, R. A. Lerche, R. L. Griffith, and C. Sorce, Rev. Sci. Instrum. **74**, 1713 (2003).

12. R. A. Lerche *et al*., Rev. Sci. Instrum. **59**, 1697 (1988).

13. J-P. Garçonnet *et al*., Rev. Sci. Instrum. **63**, 4871 (1992).

14. C. Stoeckl, V. Yu. Glebov, J. D. Zuegel, D. D. Meyerhofer, and R. A. Lerche, Rev. Sci. Instrum. **73**, 3796 (2002).

15. V. Yu. Glebov, D. D. Meyerhofer, T. C. Sangster, C. Stoeckl, S. Roberts, C. A. Barrera, J. R. Celeste, C. J. Cerjan, L. S. Dauffy, D. C. Eder, R. L. Griffith, S. W. Haan, B. A. Hammel, S. P. Hatchett, N. Izumi, J. R. Kimbrough, J. A. Koch, O. L. Landen, R. A. Lerche, B. J. MacGowan, M. J. Moran, E. W. Ng, T. W. Phillips, P. M. Song, R. Tommasini, B. K. Young, S. E. Caldwell, G. P. Grim, S. C. Evans, J. M. Mack, T. Sedillo, M. D. Wilke, D. C. Wilson, C. S. Young, D. Casey, J. A. Frenje, C. K. Li, R. D. Petrasso, F. H. Séguin, J. L. Bourgade, L. Disdier, M. Houry, I. Lantuejoul, O. Landoas, G. A. Chandler, G. W. Cooper, R. J. Lepeer, R. E. Olson, C. L. Ruiz, M. A. Sweeney, S. P. Padalino, C. Horsfield, and B. A. Davis, Rev. Sci. Instrum. **77**, 10E715 (2006).

16. Q. Tang *et al*., Rev. Sci. Instrum. **85**, 046108 (2014).

17. V. N. Goncharov, T. C. Sangster, R. Betti, T. R. Boehly, M. J. Bonino, T. J. B. Collins, R. S. Craxton, J. A. Delettrez, D. H. Edgell, R. Epstein, R. K. Follet, C. J. Forrest, D. H. Froula, V. Yu. Glebov, D. R. Harding, R. J. Henchen, S. X. Hu, I. V. Igumenshchev, R. Janezic, J. H. Kelly, T. J. Kessler, T. Z. Kosc, S. J. Loucks, J. A. Marozas, F. J. Marshall, A. V. Maximov, R. L. McCrory, P. W. McKenty, D. D. Meyerhofer, D. T. Michel, J. F. Myatt, R. Nora, P. B. Radha, S. P. Regan, W. Seka, W. T. Shmayda, R. W. Short, A. Shvydky, S. Skupsky, C. Stoeckl, B. Yaakobi, J. A. Frenje, M. Gatu-Johnson, R. D. Petrasso, and D. T. Casey, Phys. Plasmas **21**, 056315 (2014).

18. T. R. Boehly, D. L. Brown, R. S. Craxton, R. L. Keck, J. P. Knauer, J. H. Kelly, T. J. Kessler, S. A. Kumpan, S. J. Loucks, S. A. Letzring, F. J. Marshall, R. L. McCrory, S. F. B. Morse, W. Seka, J. M. Soures, and C. P. Verdon, Opt. Commun. **133**, 495 (1997).

19. Saint-Gobain Crystals, Newbury, OH 44065 (see http://www.crystals.saint-gobain.com/).

20. R. A. Lerche *et al*., Rev. Sci. Instrum. **75**, 4042 (2004).

21. C. Stoeckl, M. Cruz, V. Yu. Glebov, J. P. Knauer, R. Lauck, K. Marshall, C. Mileham, T. C. Sangster, and W. Theobald, Rev. Sci. Instrum. **81**, 10D302 (2010).

22. C. Stoeckl, J. A. Delettrez, J. H. Kelly, T. J. Kessler, B. E. Kruschwitz, S. J. Loucks, R. L. McCrory, D. D. Meyerhofer, D. N. Maywar, S. F. B. Morse, J. Myatt, A. L. Rigatti, L. J. Waxer, J. D. Zuegel, and R. B. Stephens, Fusion Sci. Technol. **49**, 367 (2006).

23. Schott North America, Inc., Elmsford, NY 10523 (see http://www.us.schott.com).

24. W. R. Donaldson, R. Boni, R. L. Keck, and P. A. Jaanimagi, Rev. Sci. Instrum. **73**, 2606 (2002).

25. Y. Arikawa *et al*., *2007 Annual Progress Report*, 47, Institute for Laser Engineering, Osaka University, Osaka, Japan (February 2008).

26. W. Theobald, A. A. Solodov, C Stoeckl, K. S. Anderson, F. N. Beg, R. Epstein, G. Fiksel, E. M. Giraldez, V. Yu. Glebov, H. Habara, S. Ivancic, L. C. Jarrott, F. J. Marshall, G. McKiernan, H. S. McLean, C. Mileham, P. M. Nilson, P. K. Patel, F. Pérez, T. C. Sangster, J. J. Santos, H. Sawada, A. Shvydky, R. B. Stephens, and M. S. Wei, Nat. Commun. **5**, 5785 (2014).

27. J. D. Lindl and E. I. Moses, Phys. Plasmas **18**, 050901 (2011).

28. D. Besnard, J. Phys.: Conf. Ser. **112**, 012004 (2008).

The Role of HfO_2/SiO_2 Thin-Film Interfaces in Near-Ultraviolet Absorption and Pulsed-Laser Damage

Introduction

It has been well established that nanosecond-pulse laser damage of multilayer coatings comprised of HfO_2/SiO_2 pairs in the near-ultraviolet (near-UV) spectral range is initiated in the high-index HfO_2 component of the coating. Still, very limited information about optical and structural properties of interfacial areas between layers renders interfaces as a probable source of enhanced absorption and damage. The reduced E-field design,[1] which moves intensity peaks away from interfaces into the more-damage–resistant SiO_2 layer, frequently improves damage threshold[2] but does not clarify the role of interfaces in laser damage. The only (to our knowledge) study[3] directly addressing interface absorption and its role in pulsed laser damage used a 1064-nm laser wavelength, with e-beam–deposited metal oxides (including HfO_2) and SiO_2 as high- and low-index materials, respectively. In that study, based on comparative absorption and damage-threshold measurements for half-wave stacks with numerous interfaces and a single-layer high-index material, HfO_2/SiO_2 interfaces made a significant contribution to total absorption and produced lower damage thresholds compared to a single HfO_2 layer. In this work a similar approach is used, but with different coatings designs, to study the contribution of HfO_2/SiO_2 interfaces to absorption in the near-UV and their role in the nanosecond-pulse damage initiation. One of the study goals is to explore how interfaces perform in coatings with different porosity and packing density. For this purpose the coatings were deposited using two techniques: (1) conventional electron-beam evaporation, typically producing rather porous films, and (2) ion-beam sputtering, which creates very densely packed films with sharp interfaces.[4] Despite the difference in thin-film structure, we found that in both cases the interfaces contribute insignificantly to total absorption and are not the main source of damage initiation.

Experimental

The coatings containing HfO_2 and SiO_2 materials were manufactured using either e-beam evaporation with a rate of 1.2 Å/s and 4.6 Å/s for HfO_2 and SiO_2, respectively, and an oxygen backfill pressure of 2×10^{-4} Torr, or reactive ion-beam sputtering, with no assist ion gun, and post-deposition annealing at 300°C for 8 h. The two types of coating samples—single HfO_2 layer and HfO_2/SiO_2 multilayer—were manufactured using a design shown schematically in Fig. 145.42. In the case of e-beam deposition, both samples were prepared in a single vacuum cycle run using shutters beneath the single-layer sample during thin SiO_2 layer deposition. This approach ensured that exactly the same HfO_2 material and deposition conditions were used for either film formation. The ion-beam–sputtered

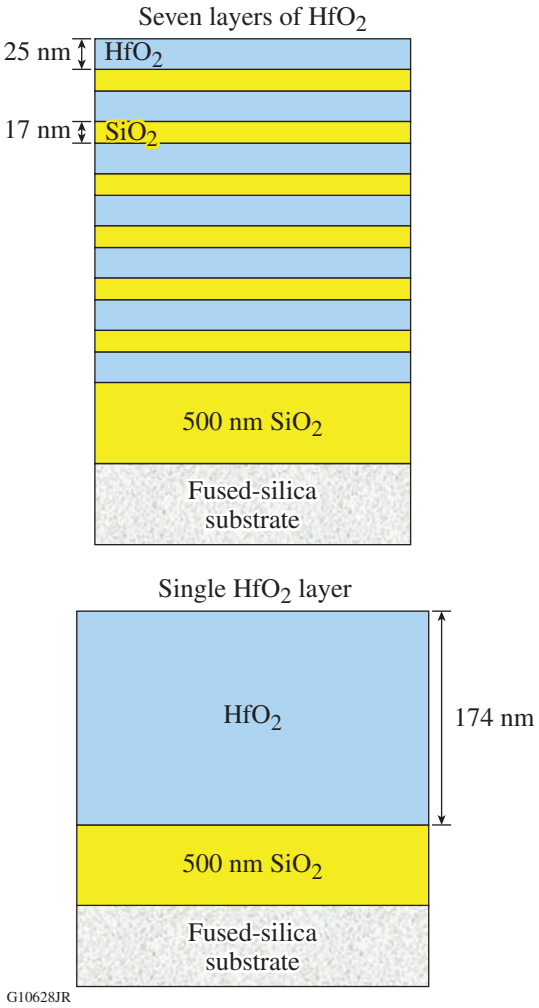

Figure 145.42
Schematic of the film containing seven HfO_2 layers separated by narrow SiO_2 layers and a single layer of HfO_2 film.

coatings were prepared in two separate coating depositions because of hardware limitations. Based on the high reproducibility of the sputtered-coating optical parameters measured for a number of runs, we anticipate that it should not affect the outcome of the experiment.

It is important to note here that a comparative laser-damage study imposes a few stringent requirements on the thin-film design and the resulting laser intensities inside the films. The thin-film structure should not change with the increasing HfO_2 layer thickness (the deposition conditions described above were selected to accomplish this goal); the total integrated HfO_2 layer thickness should be the same for single-layer and multilayer films, and E-field intensities inside both types of film samples must be comparable (preferably very close in value). To fulfill these requirements, HfO_2 single-layer films and HfO_2/SiO_2 multilayer films were manufactured with a total HfO_2 material optical thickness equal to one wave at 355 nm, which corresponds to a physical thickness of 174 nm. The multilayer film was comprised of seven HfO_2 layers, each 25 nm thick, separated by 17-nm-thick SiO_2 layers (see Figs. 145.42 and 145.43).

The thickness of the SiO_2 layers in the multilayer film (seven-layer film for future reference) was optimized to produce an E-field peak and average intensity as close as possible to the E-field intensity in the single-layer film (see Fig. 145.44). High-resolution transmission electron microscopy (TEM) along with x-ray diffraction (XRD) analysis (depicted in Fig. 145.45) reveals a fully amorphous, highly homogeneous film structure for both the seven-layer and single-layer sputtered films. The seven-layer film's interfaces [Fig. 145.45(a)] are sharp, have a roughly estimated width of 2 nm to 4 nm, and indicate no locally increased defect density. The e-beam–evaporated films were also mostly amorphous, but interfaces were not as clearly defined compared to the sputtered films [(see Fig. 145.43(c)].

The coatings were deposited on polished fused-silica substrates with a 500-nm-thick SiO_2 layer that served as an

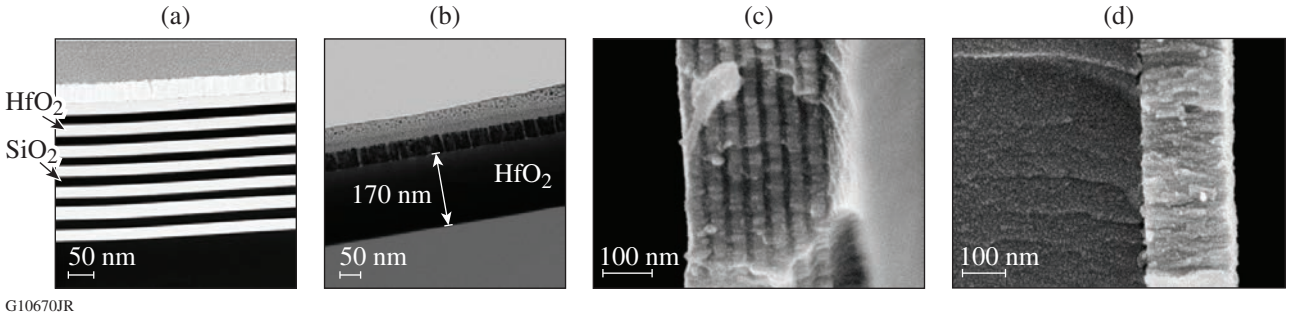

Figure 145.43
Transmission electron microscopy (TEM) images of sputtered HfO_2 films: (a) seven layer and (b) single layer. The top-most conductive layer in (a) and (b) is for TEM imaging purposes only. Electron microscopy images of electron-beam–deposited HfO_2 films: (c) seven layer and (d) single layer.

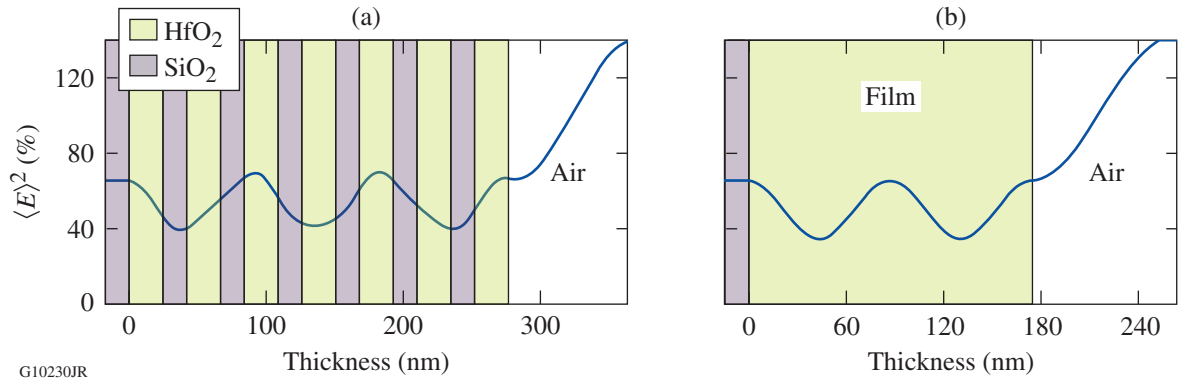

Figure 145.44
E-field intensity distribution in (a) seven-layer and (b) single-layer films.

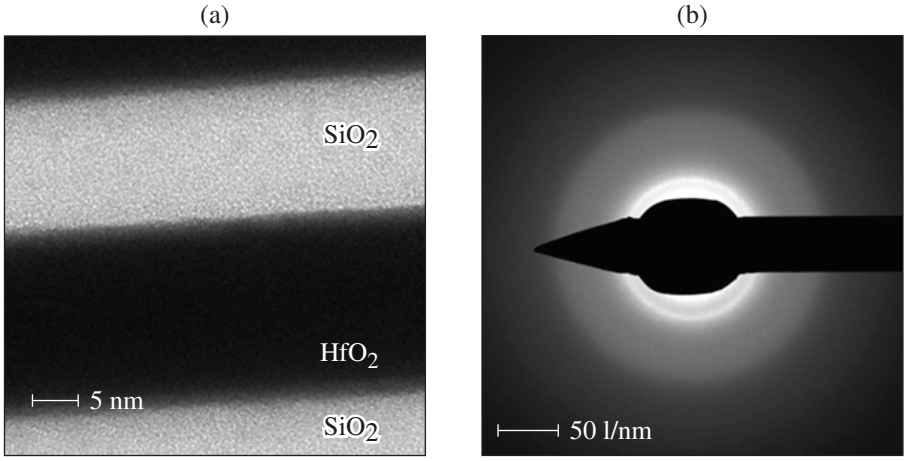

Figure 145.45
(a) A high-resolution TEM image of a seven-layer sputtered film shows a homogeneous structure with sharp interfaces and no evidence of local increased defect density. (b) X-ray diffraction (XRD) analysis confirmed a fully amorphous structure in both types of sputtered film.

insulator from defects introduced into the substrate during the finishing process. While not fully suppressing damage initiation by these defects, introducing such an additional SiO_2 layer leads to distinct substrate defect-driven damage morphology, which could be easily separated from damage initiated inside the HfO_2 film or interfaces (see **Damage Thresholds**, p. 46).

The absorption of the samples was characterized using a continuous-wave, 355-nm laser along with the following two methods: laser calorimetry (LC) and photothermal heterodyne imaging (PHI). The LC method detects heat generated through absorption of laser light and conducted by the film to the calibrated detector located on the front sample surface.[5,6] This method delivers absolute absorption values with good accuracy. The PHI method is a pump–probe laser technique based on the scattering of the probe light caused by local heating of the material by a tightly focused modulated pump beam.[7,8] The PHI method has high sensitivity and submicron spatial resolution but is more suitable for relative measurements because it is very difficult to achieve absolute calibration. Also, since this method is based on modulation of the refractive index of the material, it might be sensitive to the presence of different materials in the multilayer film. For that reason, we will consider LC as the main method of absorption characterization and PHI only as a complementary method.

Laser irradiation of samples was conducted mostly in a 1-on-1 regime (single-pulse irradiation of each sample site) using either 351-nm, 1-ns pulses [at the Laboratory for Laser Energetics (LLE)] or 355-nm, 5-ns pulses [at the Laser Zentrum Hannover (LZH) facility]. The 5-ns pulses were also used with 100-Hz frequency for the multipulse irradiation testing (10,000 pulses in this case) of each site at a fixed laser fluence. In addition, to probe changes in the interfacial structure as compared to the HfO_2 film structure (see **Femtosecond Damage Behavior as a Sensitive Tool to Detect Structural Changes and Its Application to HfO_2/SiO_2 Interfaces**, p. 49), single-pulse irradiation with 1053-nm, 600-fs pulses was conducted for both types of samples in vacuum (to avoid the self-focusing effects in air). Damage was detected using 110×-magnification dark-field microscopy or 150×-magnification Nomarsky microscopy. Laser-damage morphology was further investigated using atomic force microscopy (AFM) and scanning laser microscopy (SLM) as high-resolution tools. The high-spatial-resolution study of damage morphology was essential for separating the contribution to damage from film defects and defects residing in a subsurface layer of the substrate. The latter defects gave rise to large damage craters of up to ~10 μm in diameter, which, after high-resolution mapping, were excluded from damage statistics.

Results and Discussion

1. Absorption Measurements

Absorption-measurement data may provide guidance for anticipated optical losses in the laser system and, in some cases, for nanosecond-pulse damage performance of HfO_2 films.[8] For this study, the total contribution to near-UV absorption in the seven-layer film can come from two sources: structural defects in HfO_2 layers of the film and defects residing within the interfacial structure (absorption inside SiO_2 layers is negligibly small).

Considering additivity, total absorption A_{total} may be presented as follows: $A^7_{total} = A_{HfO_2} + A_{interface}$ for the seven-layer film, and $A^1_{total} = A_{HfO_2}$ for the single-layer film, where the superscripts 7 and 1 represent seven-layer and single-layer films, respectively.

Consequently, since the total thickness of seven hafnia layers is equal to the thickness of the single-layer film, a large-enough

contribution from interfaces should result in a larger total absorption for the seven-layer film as compared to the single-layer film. Absorption-measurement results are summarized in Table 145.V.

LC measurement results show, within a margin of error, nearly equal absorption in both seven-layer and single-layer film samples and almost two times higher absorption in the single-layer e-beam film as compared to seven-layer film. This result points to an insignificant contribution to absorption from interfaces.

The PHI method shows an even smaller relative absorption for a seven-layer film containing numerous interfaces that might be partially attributed (as discussed in **Experimental**, p. 43) to different conditions for signal formation (not just absorption) in single-layer and seven-layer films. Still, a 50% difference in the case of sputtered films and an even higher ratio for e-beam films indicates a small contribution from interfaces.

2. Damage Thresholds

The transparent nature of the coatings involved in this study required the careful separation of damage originating from film volume (seven-layer film or single-layer film) and from substrate–subsurface defects introduced during the substrate-finishing process. The presence of an isolating 500-nm-thick SiO_2 layer (see Fig. 145.42) leads to much deeper and larger damage craters initiated by substrate defects, compared to craters formed by absorption inside the HfO_2 layers. AFM mapping clearly reveals this difference (see Figs. 145.46 and 145.47) and allows one to exclude craters initiated by substrate defects from damage statistics.

To find the 351-nm, 1-ns damage threshold, ten sample sites were irradiated with a different laser fluence, and subsequent AFM mapping enabled us to acquire the damage-crater statistics depicted in Fig. 145.48. The thresholds were obtained by

Table 145.V: The 355-nm absorptance of seven-layer and single-layer films measured by laser calorimetry (LC) and photothermal heterodyne imaging (PHI) signals produced with a 355-nm pump laser.

Film type	LC (%)		PHI signal (μV)	
	Ion beam	e-beam	Ion beam	e-beam
Seven layers	0.14±0.01	0.015±0.001	31.5±0.5	0.24±0.10
Single layer	0.13±0.01	0.027±0.002	47.0±0.5	1.28±0.16

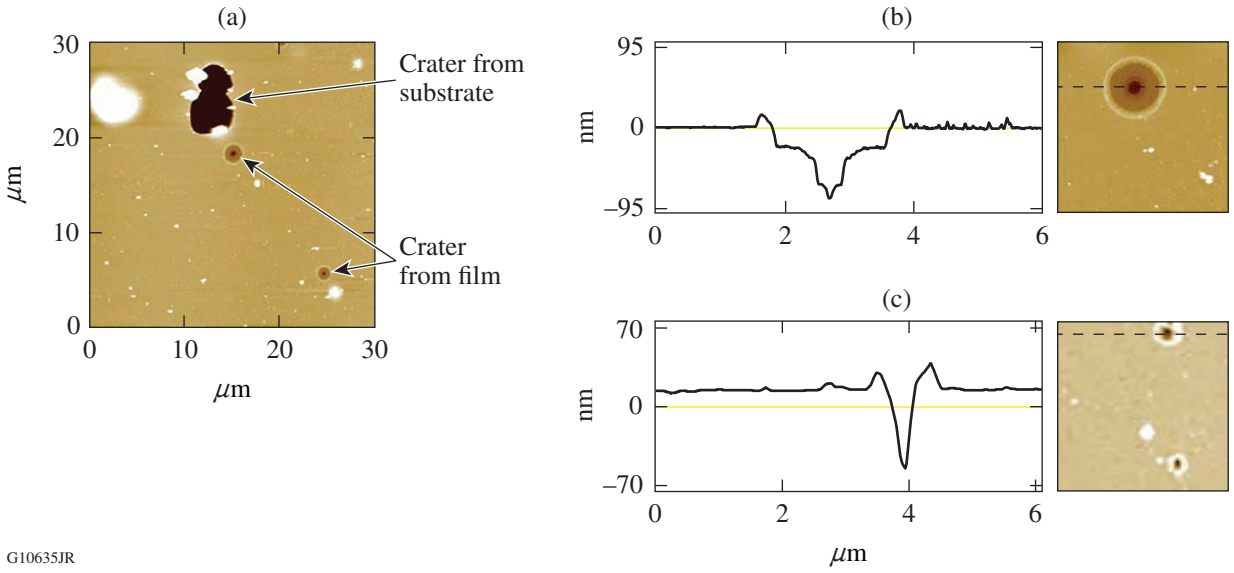

Figure 145.46
Atomic force microscopy mapping of damage morphology in sputtered films: (a) 30 × 30-μm image of the seven-layer film. Large (~10-μm-diam) craters originate from a location corresponding to substrate–subsurface defects and much smaller (≤2-μm-diam) craters originate from the film volume; (b) cross-sectional profile through a crater originating inside the seven-layer film; (c) cross-sectional profile through a crater originating inside the single-layer film.

linear fitting and extrapolation of the trend line to the fluence at which the number of craters is equal to zero. It should be noted that in the case of the e-beam–deposited, seven-layer film, only the upper limit of the threshold value was estimated because of collateral damage caused by substrate defects at laser fluences exceeding 8 J/cm^2. Below this fluence level no craters originating from the film volume were found using AFM mapping.

In the case of 355-nm, 5-ns pulse irradiation, damage morphology was analyzed using 150×-magnification optical microscopy and, for crater profiling, SLM (see Fig. 145.49). Similar to AFM mapping, SLM analysis made it possible to separate the damage originating within the film volume from the substrate-defect–driven damage. Damage thresholds were obtained from the damage probability curves shown in Fig. 145.50. The threshold measurement results are summarized in Table 145.VI.

The thresholds increase only marginally with the pulse-length increase (practically no scaling), which might be explained by different methodology used to derive the thresholds at the two

Table 145.VI: Damage thresholds of ion-beam–sputtered and e-beam–evaporated films.

Thresholds (J/cm^2)			
Film type	351 nm, 1 ns		355 nm, 5 ns
	Ion beam	e-beam	Ion beam
Single layer	5.5±0.3	4.5±0.3	6.2±0.5
Seven layer	6.5±0.3	≥8	7.5±0.5

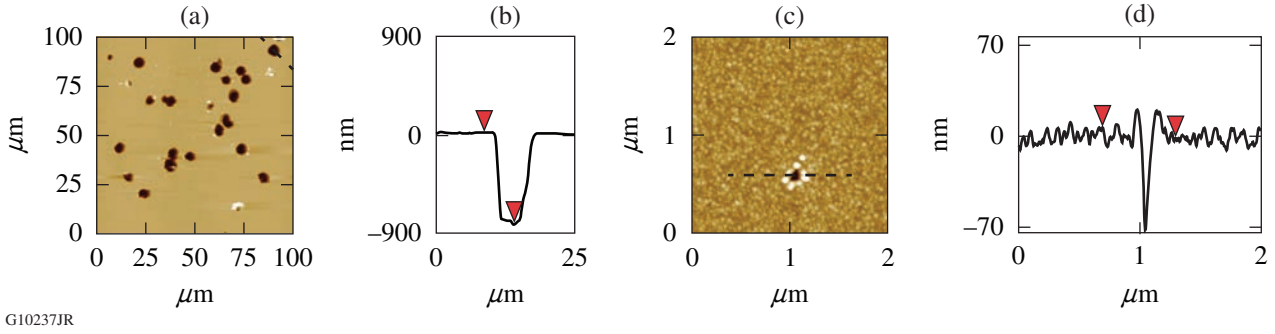

Figure 145.47
Atomic force microscopy mapping of damage morphology in e-beam–deposited films: (a) 100 × 100-μm image of the seven-layer film irradiated with a 5.9-J/cm^2 fluence. Damage morphology is dominated by craters initiated by substrate defects; (b) cross-sectional profile through a typical crater showing depth corresponding to substrate–subsurface absorbing-layer location (~800 nm); (c) 2 × 2-μm image of the single-layer film irradiated with a 4.6-J/cm^2 fluence, which shows a crater originating from within the HfO_2 film volume; and (d) cross-sectional profile through the crater shown in (c).

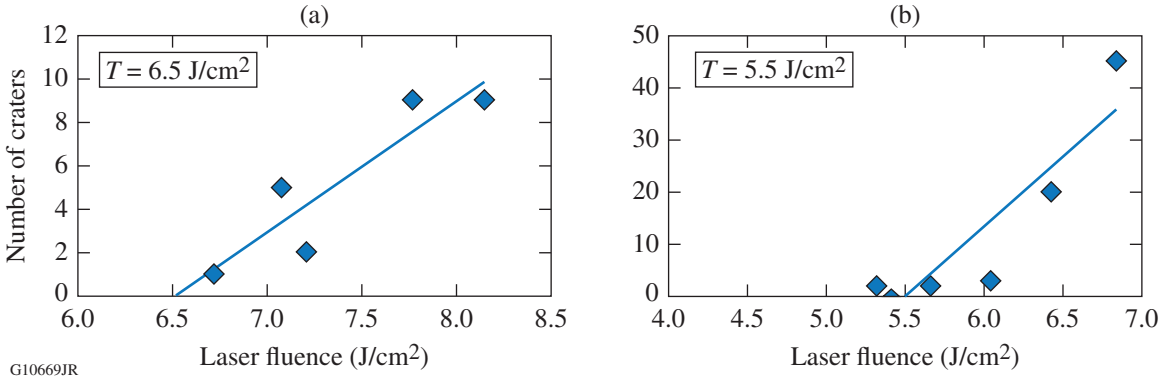

Figure 145.48
The number of damage craters originating from sputtered HfO_2 films as a function of 351-nm, 1-ns laser fluence for (a) seven-layer and (b) single-layer films. The thresholds are obtained by linear extrapolation to the fluence at which the number of craters is equal to zero.

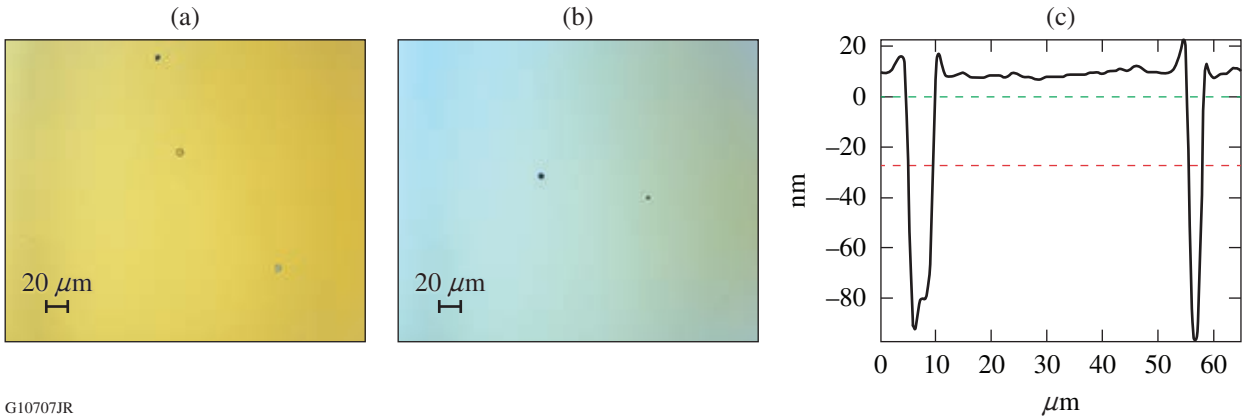

Figure 145.49
Optical microscope images of damage morphology of sputtered films irradiated at close-to-threshold conditions: (a) seven-layer film irradiated at 7.7 J/cm^2 and (b) single-layer film irradiated at 6.3 J/cm^2. (c) An example of crater cross-sectional analysis using scanning laser microscopy (SLM).

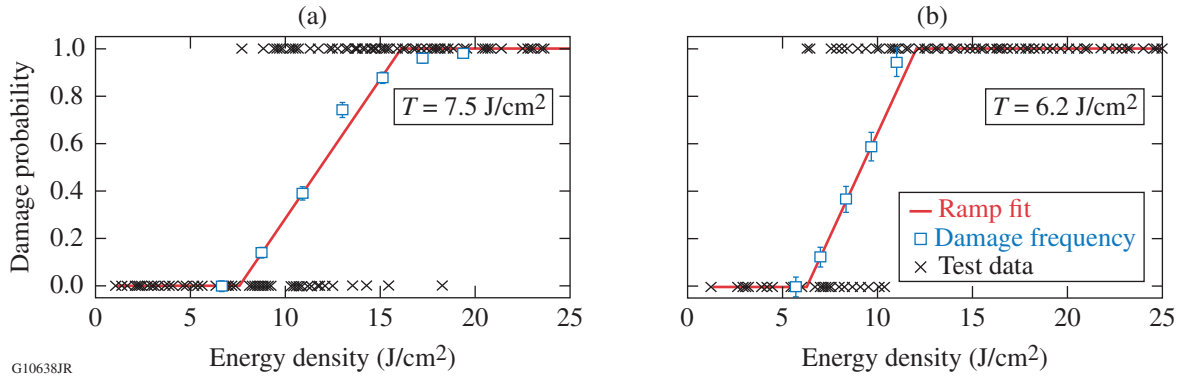

Figure 145.50
Damage-probability curves resulting from 355-nm, 5-ns irradiation of sputtered films: (a) seven-layer and (b) single-layer film. The thresholds are obtained by a linear extrapolation to zero probability.

different facilities (LLE and LZH). More importantly, these results obtained for thin films with distinctly different morphology—densely packed ion-beam–deposited films and highly porous e-beam films—demonstrate higher nanosecond-pulse damage resistance for the film containing numerous HfO_2/SiO_2 interfaces as compared to a single-layer HfO_2 film. Note that the E-field peak intensity in the seven-layer film is slightly (~7%) higher than that in the single-layer film, which means that the threshold ratio normalized by internal intensity would be even higher. Also, at close-to-threshold conditions, only a few damage sites (craters) are initiated in the sputtered seven-layer film [(see Fig. 145.48(a)], and at the same laser fluence of 6.5 J/cm^2 the number of craters initiated in the single-layer film exceeds 20 [(see Fig. 145.48(b)], therefore pointing to lower damage resistance of the single-layer film. All of these facts lead to the conclusion that HfO_2/SiO_2 interfaces are not a source of enhanced near-UV localized absorption and laser damage. One possible explanation for these findings comes from the hypothesis that the interfacial structure is similar to the film structure formed during co-deposition of HfO_2 and SiO_2. It was convincingly demonstrated that in co-deposited films, near-UV absorption is reduced and damage resistance becomes higher in HfO_2 films with an increased SiO_2 content.[9]

3. E-Field Intensity Distribution and Damage Morphology

A correlation between E-field intensity inside a coating and damage initiation is well established. One example is damage originating in nodular-coating defects where a large E-field may be generated.[10] To test the presence of such a link in this study, crater-depth distributions obtained at ~70% above threshold conditions using SLM (see Fig. 145.51) were compared to the E-field intensity distributions depicted in Fig. 145.44. One

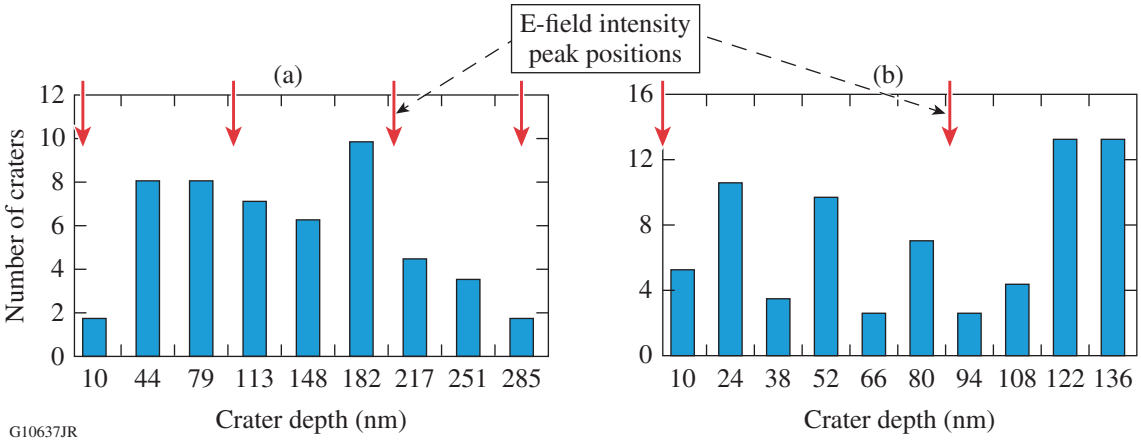

Figure 145.51
Crater-depth distributions obtained from SLM analysis for (a) seven-layer and (b) single-layer films.

can see that crater-depth distributions show no correlation with E-field peak positions; this observation does not change even when the depth bin size used to calculate the distribution is varied.

There are several reasons why a correlation was not observed: First, the intensity variation from the minimum to maximum value was not high for both types of film; the normalized intensity $\left(|E|^2\right)$ varied from 40% to 70% and from 34% to 65% in the seven-layer and single-layer films, respectively. For comparison, in standard quarter-wave reflectors, $|E|^2$ might vary from 0% to 100% (Ref. 11). Second, crater depth depends not only on the location of the localized absorber but also on the amount of energy locally deposited,[12] which leads to a distribution in the crater-depth values.

4. Femtosecond Damage Behavior as a Sensitive Tool to Detect Structural Changes and Its Application to HfO_2/SiO_2 Interfaces

The key to understanding the role of interfaces in pulsed laser damage is a knowledge of how the electronic structure changes during the spatial transition from HfO_2 to SiO_2 and vice versa. An important parameter here is a band gap of E_g and characteristics of the electronic defect states,[13,14] such as location in a gap (see Fig. 145.52), densities, and absorption coefficients. In the absence of structural data for interfaces, an alternative empirical approach is to study the interaction of subpicosecond laser pulses with optical materials—in this particular case, with a film containing numerous HfO_2/SiO_2 interfaces and a single-layer HfO_2 film. Femtosecond-pulse laser damage in dielectrics typically starts with the multiphoton ionization (MPI) process, which is very sensitive to band-gap and defect-state characteristics.[15,16] The sensitivity is linked to a possible change in the number of absorbed photons required to promote an electron into the conduction band, which leads to a dramatic change in the multiphoton absorption coefficient.[17] Since the same defect states might participate in multiphoton absorption of infrared light and single-photon absorption of UV light (see Fig. 145.52), a femtosecond damage study may indicate whether an interfacial structure is more or less damage resistant than an HfO_2 structure in the case of UV light and nanosecond pulses. In this study, the existence of such a correlation was tested by 1053-nm, 600-fs pulse irradiation (1-on-1 test) of single-layer and seven-layer samples. The damage thresholds T, normalized by internal E-field intensity

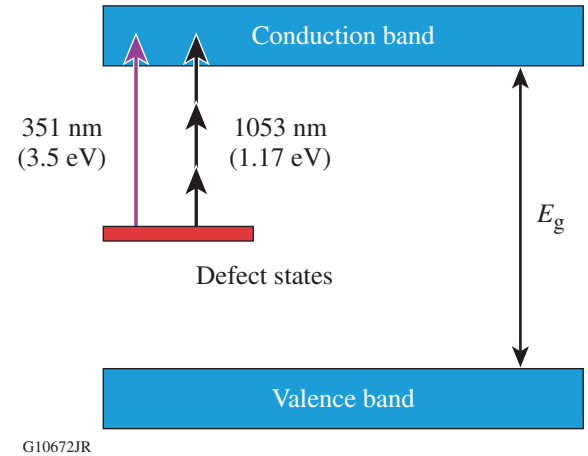

Figure 145.52
Schematic of the dielectric band structure with electronic defect states taking part in single-photon and multiphoton absorption promoting an electron into the conduction band.

[(average intensity was used for normalization because of slow changes across the film (see Fig.145.53)] showed a ratio of $T_{\text{seven layer}}/T_{\text{single layer}} \geq 1.1$ for both ion-beam–sputtered and e-beam–evaporated films.

This result points to a low contribution of interfaces to the MPI process and correlates well with higher near-UV, nanosecond-pulse damage resistance of the interfacial structure as compared to the HfO_2 film, in agreement with the 351-/355-nm threshold measurement results presented in **Damage Thresholds** (p. 46). This result also strongly supports the possibility that initial absorption—single photon for nanosecond pulses and multiphoton for femtosecond pulses—is initiated by the same structural defects.

5. Multipulse Irradiation

From a practical point of view, it is of interest to know how interfaces respond to multipulse, fixed-fluence irradiation. The typical behavior of coatings is characterized by the fatigue effect manifested by a lower threshold and increased scale of damage.[18] For this purpose, 10,000-pulse (355-nm, 5-ns) irradiation at a fixed laser fluence and a 100-Hz repetition rate was performed for seven-layer and single-layer films. The density of produced damage sites (craters) was calculated and compared with damage-site density produced using single-shot irradiation at a fluence slightly above the single-shot threshold. The fatigue effect was observed for both types of films but with a less-pronounced effect for the film with numerous interfaces. The seven-layer film showed a seven-fold increase in damage-site density compared to a 12-fold increase for a single-layer film. This result points to an interfacial structure that is less susceptible to absorbing-defect formation under near-UV light irradiation, as compared to the pure-HfO_2 material.

Conclusions

The role of ion-beam–sputtered and e-beam–evaporated HfO_2/SiO_2 film interfaces in near-UV absorption and nanosecond-pulse damage was investigated by comparing the damage performance of a film with numerous interfaces (seven HfO_2 layers) and a monolayer HfO_2 film. The films were characterized by an overall equal HfO_2 material thickness, comparable E-field intensity, and fully amorphous material structure.

The study revealed a low contribution of interfaces to near-UV absorption and higher nanosecond-pulse damage thresholds for a film with numerous interfaces as compared to a single-layer HfO_2 film. These results indicate that HfO_2/SiO_2 interfacial structures have a higher laser-damage resistance than a structure of a pure HfO_2 film.

The similarity of an interfacial HfO_2/SiO_2 structure to a structure formed during co-deposition of HfO_2 and SiO_2 materials, which is documented to have higher pulsed-laser-damage resistance as compared to a pure HfO_2 film material, may offer a possible explanation for these findings. A correlation found between near-UV, nanosecond-pulse and 1053-nm, 600-fs pulse damage of HfO_2 coatings used for this study allows one to suggest that the initial absorption (single photon for nanosecond pulses and multiphoton for femtosecond pulses) involves the same electronic defect states. The relevance of these results to other high-/low-index film material pairs requires additional studies.

ACKNOWLEDGMENT

This material is based upon work supported by the Department of Energy National Nuclear Security Administration under Award Number DE-NA0001944, the University of Rochester, and the New York State Energy Research and Development Authority. This work is also supported by the

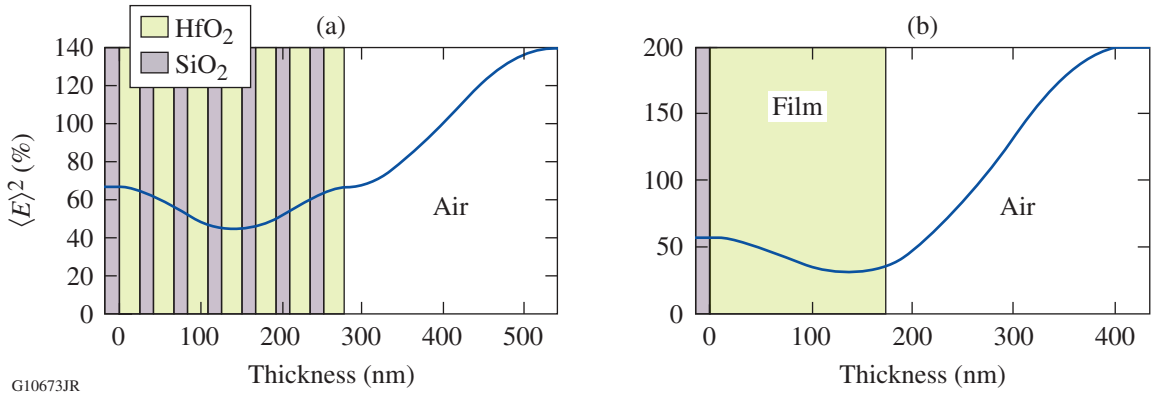

Figure 145.53
The distribution of 1053-nm E-field intensity in (a) seven-layer and (b) single-layer films.

German Federal Ministry of Education and Research within Ultra-Life project under contract #13N11558. The support of DOE does not constitute an endorsement by DOE of the views expressed in this article.

REFERENCES

1. J. H. Apfel, Appl. Opt. **16**, 1880 (1977).
2. D. H. Gill, B. E. Newnam, and J. McLeod, in *Laser Induced Damage in Optical Materials: 1977*, edited by A. J. Glass and A. H. Guenther, Nat. Bur. Stand. (U.S.), Spec. Publ. 509 (U.S. Government Printing Office, Washington, DC, 1977), pp. 260–270.
3. D. Ristau, X. C. Dang, and J. Ebert, in *Laser Induced Damage in Optical Materials: 1984*, edited by H. E. Bennett *et al*., Natl. Bur. Stand. (U.S.), Spec. Publ. 727 (U.S. Government Printing Office, Washington, DC, 1986), pp. 298–306.
4. H. K. Pulker, in *Optical Interference Coatings*, edited by N. Kaiser and H. K. Pulker, Springer Series in Optical Sciences, edited by A. Adibi *et al*. (Springer-Verlag, Berlin, 2003), pp. 131–154.
5. U. Willamowski, D. Ristau, and E. Welsch, Appl. Opt. **37**, 8362 (1998).
6. I. Balasa, L. Jensen, and D. Ristau, Proc. SPIE **8885**, 88851L (2013).
7. S. Berciaud *et al*., Phys. Rev. B **73**, 045424 (2006).
8. S. Papernov, A. Tait, W. Bittle, A. W. Schmid, J. B. Oliver, and P. Kupinski, J. Appl. Phys. **109**, 113106 (2011).
9. L. O. Jensen *et al*., Proc. SPIE **7842**, 784207 (2010).
10. X. Cheng *et al*., Appl. Opt. **53**, A62 (2014).
11. P. Baumeister, *Optical Coating Technology* (SPIE Optical Engineering Press, Bellingham, WA, 2004), pp. 9-56–9-57.
12. S. Papernov, in *Laser-Induced Damage in Optical Materials*, edited by D. Ristau (CRC Press/Taylor & Francis, Boca Raton, FL, 2014), Sec. I, Chap. 3, pp. 25–74.
13. A. S. Foster *et al*., Phys. Rev. B **65**, 174117 (2002).
14. T.-J. Chen and C.-L. Kuoa, J. Appl. Phys. **110**, 064105 (2011).
15. L. Gallais *et al*., Proc. SPIE **8530**, 85300K (2012).
16. W. Rudolph *et al*., Proc. SPIE **8885**, 888516 (2013).
17. L. V. Keldysh, Sov. Phys.-JETP **20**, 1307 (1965).
18. A. Hervy *et al*., Proc. SPIE **9237**, 92370J (2014).

A Chromatic-Aberration Diagnostic Based on a Spectrally Resolved Lateral-Shearing Interferometer

Spatiotemporal coupling in an ultrashort-pulse beam is an important feature that must be characterized for laser–matter interactions and focal-spot improvement. Pulse-front tilt (PFT) arising from a misaligned compressor-grating pair or a simple prism disperses the spatial and spectral envelope of the pulse at focus with respect to wavelength, thereby lowering the available peak power density.[1] Radial-group delay (RGD) arising in a circularly symmetric, refractive-image relay similarly smears the focal spot transversely and longitudinally.[2] Compensation schemes for PFT and RGD based on diffraction and refraction were proposed in Refs. 3 and 4. Space−time coupling can be beneficial in some experimental configurations. Spatial chirp in the beam obtains maximum spatial and spectral overlap at focus, creating a "temporal-focusing effect," which has been useful in the area of micromachining[5] and microscopy.[6] The wavefront-rotation effect introduced by focusing a pulse with PFT creates an angularly separated burst of attosecond pulses reflecting off the laser-induced plasma.[7]

A diagnostic is needed to compensate for and control the spatiotemporal effects, not only from well-defined optical systems but also from nonuniform optical properties such as in dielectric optical coatings. A second-harmonic, single-shot autocorrelator can be used to measure the pulse-front tilt angle[8] or the effect of pulse broadening caused by RGD.[9] Linear autocorrelation methods infer the angle or the curvature of the pulse-front delay by examining, in multiple steps, the fringes between two beams.[2] Other linear techniques are based on spectrally resolving spatial interference. These methods analyze the spectrum of the interference between two laterally sheared fields of the same test beam[10] or between the test and reference fields,[11] where the carrier terms are introduced by either temporal delay or relative tilt; direct fringe analysis can be employed for certain referenced schemes.[12] All these spectral interference methods require a separate system of beam splitters and combiners external to the spectrometer. Scanning the spectral interferogram with a fiber tip[13] or using phase diversity on a cylindrically symmetric beam[14]—both require multiple measurement steps and have been demonstrated. A rather unique scheme called STRIPED FISH[15] provides discrete samples of spectral slices with full two-dimensional (2-D) intensity and phase mapping at each slice by interfering each slice with a reference beam; however, spatial and spectral resolution of this method is poor.

A simpler, spectrally resolved lateral-shearing interferometer is proposed in this work. The separate preconditioning system introducing delay or tilt is replaced by a single Ronchi grating located in front of the entrance slit of a spectrometer. No moving parts are involved; therefore, calibration is performed only once. Full one-dimensional (1-D) chromatic aberrations can be characterized in a single-shot measurement.

The side and top views of the setup are schematically shown in Fig. 145.54, with the spectrometer system laid out linearly.

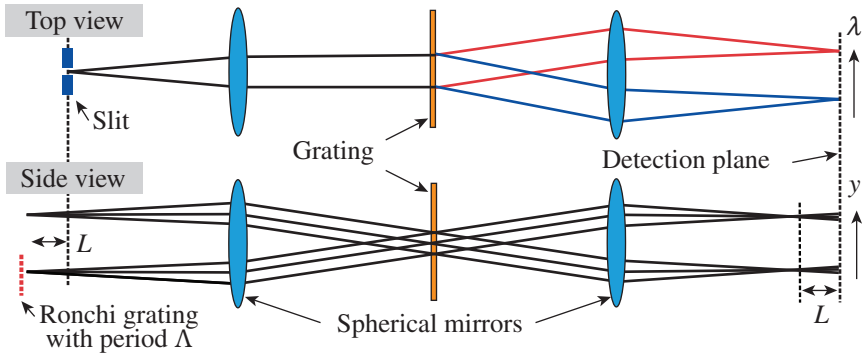

Figure 145.54
A schematic of a spectrally resolved lateral-shearing interferometer. The entrance slit is spectrally resolved in a tangential plane, whereas the sagittal image of the slit is interfered to create a sheared interferogram from which spatial phase can be extracted. Only zeroth- and first-order diffractions are shown in the side view. For convenience, the rays reflected by the spherical mirrors and the spectrometer grating are shown on the other side of the mirror as if they are passing through.

The top view representing the beam diffracting in the horizontal plane corresponds to a normal spectrometer system. The side view shows the beam diffracting through the Ronchi grating in the vertical plane. The detector images the spectrometer slit. The Ronchi plane is imaged before the detector plane; therefore, the first-order diffraction beams are sheared at the detector plane. If the beam is sampled at a fixed horizontal coordinate x_0 by the spectrometer slit, the field at the detector plane going through a Ronchi grating of periodicity Λ is represented by[16]

$$E(x_0,y,\omega) = \sum_{m=0,\pm1,\ldots} \eta_m A\left(x_0, y + m\frac{2\pi cL}{\omega\Lambda}\right) \times \exp\left(i\frac{2\pi m}{\Lambda}y + i|m|\omega\tau\right), \quad (1)$$

where $A(x_0,y,\omega)$ is the spectral envelope and phase at position y at the entrance slit. The index m is the diffraction order and η_m is the diffraction efficiency at the mth order. The spatial coordinate x_0, hereafter, will not be shown. L is the distance from the Ronchi grating to the entrance slit and τ is the arrival time difference between the first- and zeroth-order diffraction beams; τ is sufficiently small that spectral fringes are not observed. The 1-D Fourier-domain analysis of the interferogram along the spatial axis can separate out the first harmonic H_1 (i.e., the interaction between fields at $m = 0$ and $m = \pm1$) from dc and higher-order terms. With the phase of $A(y,\omega)$ defined as $\varphi(y,\omega)$, the first harmonic is

$$H_1 \sim |A(y,\omega)|^2 \exp\left(i\frac{2\pi cL}{\omega\Lambda}\frac{\partial\varphi}{\partial y}\right)\cos(\omega\tau)\exp\left(i\frac{2\pi}{\Lambda}y\right). \quad (2)$$

The phase of H_1, except for the carrier term, contains a phase derivative from which spectrally coupled 1-D spatial phase can be integrated. Purely spectral phase without spatial dependence cancels out in the derivative so it is not measurable in this approach.

Pulse-front delay (PFD) and RGD are linear and quadratic-phase components whose magnitudes vary linearly with the spectral deviation. The phase can be decomposed into chromatic and achromatic components, denoted as $g(y)$ and $f(y)$, respectively:

$$\varphi(y,\omega) = (\omega - \omega_0)\, g(y) + \frac{\omega}{c} f(y), \quad (3)$$

where $f(y)$ is an optical-path difference function in units of distance and $g(y)$ is a relative group delay in units of time; $f(y)$ can be represented as

$$f(y) = \theta_y\, y + y^2/(2R_y) + f_{\mathrm{HO}}(y), \quad (4)$$

where θ_y and R_y are the tilt and radius of curvature in the y dimension, respectively, and $f_{\mathrm{HO}}(y)$ is the remaining higher-order term. Likewise, $g(y)$ is the sum of linear, quadratic, and higher-order terms [$g_{\mathrm{HO}}(y)$]:

$$g(y) = \alpha\left(\frac{y}{r}\right) + \beta\left(\frac{y}{r}\right)^2 + g_{\mathrm{HO}}(y), \quad (5)$$

where r is the radius of the beam and α = PFD(r)–PFD(0) and β = RGD(r)–RGD(0). Equations (3) and (5) suggest that the PFD shifts the carrier-phase offset linearly with respect to frequency change, and RGD modifies the carrier frequency linearly with respect to frequency change. The fringe patterns with PFD or RGD dominant cases are illustrated in Fig. 145.55.

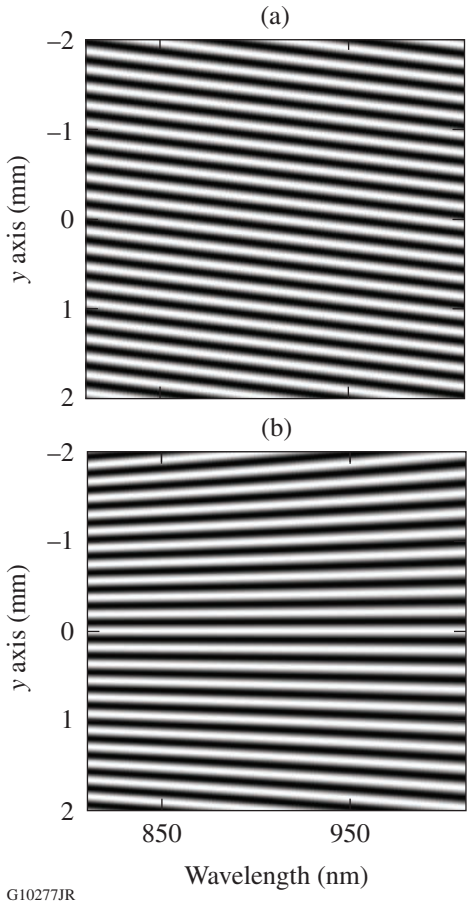

Figure 145.55
Examples of fringe patterns. (a) The tilted fringe indicates pulse-front tilt and (b) the fanning-out fringe indicates radial-group delay.

The algebraic form of $(2\pi cL)/(\omega\Lambda) \cdot \partial\varphi/\partial y$, consistent with Eqs. (3)–(5), is

$$\frac{2\pi cL}{\omega\Lambda}\frac{\partial\varphi}{\partial y} \triangleq \Delta\varphi = c_1 + c_2 y + (c_3 + c_4 y)(\lambda - \lambda_0). \quad (6)$$

Comparing Eqs. (4) and (5), the coefficients of Eq. (6) are determined as

$$c_1 = 2\pi\frac{L}{\Lambda}\theta_y, \quad (7)$$

$$c_2 = 2\pi\frac{L}{R_y\Lambda}, \quad (8)$$

$$c_3 = -\frac{2\pi c}{\lambda_0}\frac{L\alpha}{\Lambda r}, \quad (9)$$

$$c_4 = -\frac{4\pi c}{\lambda_0}\frac{L\beta}{\Lambda r^2}. \quad (10)$$

Extracting RGD and PFD information directly from the low-order polynomial fit of $\Delta\varphi$ is less ambiguous than fitting Eq. (3) to the numerically integrated data of $\Delta\varphi$ because of the arbitrary integration constant.

A test bed was set up to measure RGD in a simple refractive system, as shown in Fig. 145.56. The broadband source is a spectrally incoherent, superluminescent light-emitting diode (SLED) with spectral density from 968 to 1076 nm. An actual ultrashort pulse was not required for the demonstration because only relative phases are required to characterize space–time coupling. The SLED is coupled to a single-mode fiber whose tip is used as a point source. A 200-mm-focal-length concave mirror collimates the diverging beam from the fiber tip. The off-axis configuration of the concave mirror introduces astigmatism, but it is not important since the wavefront must be collimated only in the sagittal plane parallel to the spectrometer slit. The collimated beam is sent to the test telescope (L3 and L4) through a 5-mm input aperture. The aperture plane is imaged to M2 and to the slit. The imaging requirement minimizes the chromatic effect on the beam size. The focal lengths of L3 and L4 are 71.6 mm (fused silica) and 378.9 mm (BK7) at 1037 nm, respectively. The calculated RGD of the test telescope in a double-pass configuration is 50.6 fs over a 5-mm aperture. The input aperture is re-imaged through the beam splitter (BS) to the spectrometer slit by an imaging telescope (L1, L2). L1 and L2 have the same 61.0-mm focal length. The single-pass RGD in the imaging telescope is 0.9 fs over 5 mm. The spectrometer is a Czerny–Turner type with a grating groove density of 150 lines/mm (SP-2556, Princeton Instruments). The chromatic aberrations in the imaging telescope are calibrated using a reference interferogram by inserting a retroreflective mirror (M1) behind the aperture. The reference phase is always subtracted from the measured phase.

The distance between the spherical mirrors is shorter than $2f$, so the collimated input beam slightly diverges at the detector plane in the side view. This is because the commercial spectrometer is required to image only the horizontal dimension while keeping its size compact. The beam sizes at the entrance slit and at the detector plane are, however, the same. The period of the Ronchi grating is separately calibrated using an independently collimated source. The period is found to be 201.1 μm by analyzing the projected image of the Ronchi grating in the Fourier domain.

The measured interferogram and the reconstructed phase are shown in Fig. 145.57. The fringe spacing in Fig. 145.57(a) increases slightly from left to right, indicating the presence of RGD. The reconstructed phase in Fig. 145.57(b) shows the wavelength-dependent quadratic phase, where the curves are spaced out by arbitrary integration constants for visualization purposes. The top curve corresponds to 1068 nm and the bottom to 970 nm. The distance from the Ronchi to the slit, L, is 30.08 mm. To maximize the fringe contrast, L is approximately set to a multiple of the Talbot distance. The measured RGD is

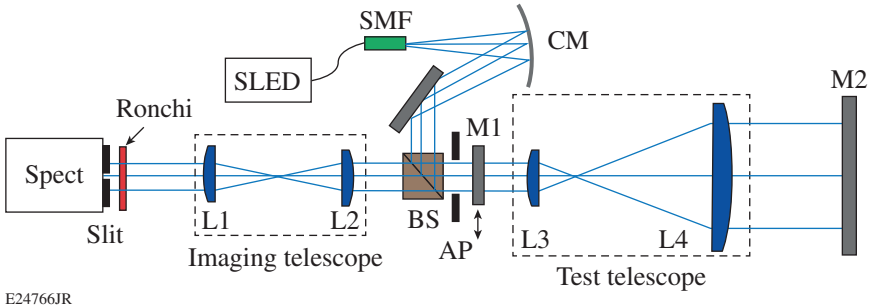

Figure 145.56
Experimental setup. SLED: superluminescent light-emitting diode; SMF: single-mode fiber; CM: concave mirror; BS: beam splitter; AP: aperture; M1 and M2: mirrors; L1–L4: lenses; Spect: spectrometer.

51.1 fs using Eq. (10), which is within 1% of the direct calculation based on dispersion and lens curvature.[17] Figure 145.57(c) shows the sum of both chromatic and achromatic higher-order terms, which is mainly the spherical aberration (i.e., fourth-order phase) in the system.

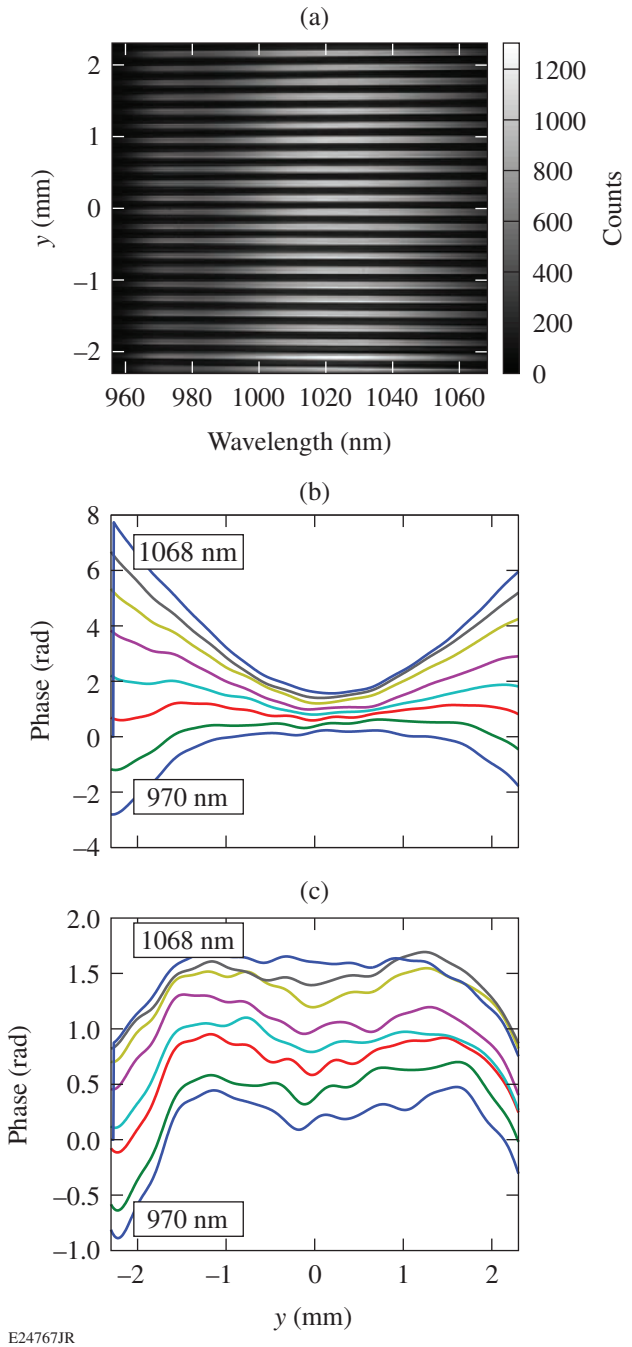

Figure 145.57
Experimental results. (a) Interferogram image, (b) the lineouts of the reconstructed phase at different wavelengths, and (c) the higher-order phase.

A PFD measurement was demonstrated using a BK7 prism (wedge angle of 11°20′) mounted on a rotation stage and placed in front of the Ronchi grating. Since PFD is measured only in the vertical direction (y axis) in this setup, the PFD along the y axis can be varied according to the in-plane rotation angle. Because of the beam deviation and pointing error on insertion of the wedge, the beam centering and pointing must be restored. A flipper mirror was installed between the wedge and the Ronchi grating to send the beam to the pointing and centering diagnostic cameras. The two mirrors between the wedge and L1 were adjusted to restore the alignment. The beam position was aligned within ±50 μm and the pointing within ±150 μrad, with respect to the reference positions recorded without the wedge. The rather large pointing inaccuracy comes mainly from the mechanical instability of the flipper mirror. The simulation suggests this level of fluctuation introduces only a ±0.5-fs error in PFD. The centering camera images the beam at the equivalent imaging plane of the spectrometer slit. The exact centering alignment becomes important in proportion to the amount of RGD, because any centering shift mixed with RGD [i.e., c_4 of Eq. (10)] will result in additional c_3 as calculated by Eq. (9), which is used to estimate PFD. The insertion of retro-mirror M1 redirects the beam through only the imaging telescope (L1 and L2). The aperture diameter was set to 6 mm. The relative PFD with the wedge is shown in Fig. 145.58. The PFD as measured at seven different angles shows good agreement compared with the calculated PFD. The error bar is the standard deviation of the measured fluctuation in five independent sets of measurements. The PFD at 90° rotation

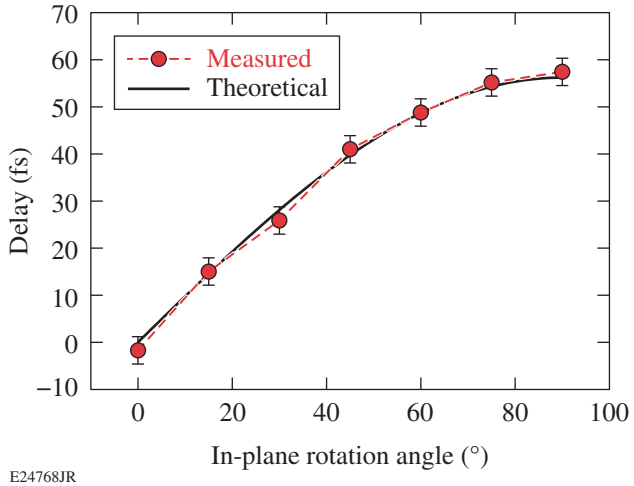

Figure 145.58
Experimental results of measuring the variable pulse-front tilt using an 11° prism.

(wedge parallel to the slit) is 56.2 fs. The standard deviation of the measured PFD with respect to theoretical values is 1.4 fs.

Both RGD and PFD are dependent on beam size; an exact beam size must be specified for given RGD and PFD values. The angle of pulse-front tilt ($\theta_{\Delta T}$) and the temporal radius of curvature in the radial-group delay ($R_{\Delta T}$) could be useful alternatives that are independent of beam size. From the definition of group delay ($\partial\varphi/\partial\omega$), $\theta_{\Delta T}$ is found to be $c\alpha/r$ and $R_{\Delta T}$ is $r^2/(2\beta c^2)$; $R_{\Delta T}$ is 682 ps in the above experiment.

A slightly different arrangement of the system could provide greater flexibility. The Ronchi grating, for example, can be placed directly in front of the detector rather than in front of the entrance slit. Additionally, the input beam rotated by 90° can provide the PFD and RGD information in the orthogonal direction. The rotated beam can also be stacked on top of the original beam to provide 2-D information in a single shot.

The form of Eqs. (6), (9), and (10) suggests that the absolute calibration of the wavelength axis is not necessary for estimating chromatic aberrations (i.e., PFD and RGD) as long as the center wavelength λ_0 is known. The error in the estimation of the absolute wavelength will result in the estimation of the achromatic term [$f(y)$ in Eq. (3)] but not in the chromatic terms. A compact setup made of a non-imaging, dispersive element and a Ronchi or a similar grating might be able to provide the same information.

Regarding the measurements of low-order chromatic aberrations, the full spectrum may not be required. A combination of separate measurements using only narrow-bandwidth sources can also provide the RGD. Reprocessing the data using 2-nm-bandwidth, numerically cropped segments of the measured interferogram at three points (970 nm, 1000 nm and 1030 nm) still results in an RGD within a 1% error. The effect of noise between separate measurements, however, has not yet been evaluated.

A simple, spectrally resolved, 1-D lateral-shearing interferometer that can be used to characterize spatiotemporal coupling in a single shot has been demonstrated. The setup requires only a single Ronchi grating attached in front of a spectrometer. The calibration is done only once, and it can be easily transported. Its accuracy was experimentally demonstrated in the measurements of RGD and PFD. Suggestions have been made on different ways of implementing the basic idea and on the possibility of improving and simplifying the system.

ACKNOWLEDGMENT

This material is based upon work supported by the Department of Energy National Nuclear Security Administration under Award Number DE-NA0001944, the University of Rochester, and the New York State Energy Research and Development Authority. The support of DOE does not constitute an endorsement by DOE of the views expressed in this article.

REFERENCES

1. G. Pretzler, A. Kasper, and K. J. Witte, Appl. Phys. B **70**, 1 (2000).
2. H.-M. Heuck *et al*., Appl. Phys. B **84**, 421 (2006).
3. J. Néauport, Appl. Opt. **46**, 1568 (2007).
4. S.-W. Bahk, J. Bromage, and J. D. Zuegel, Opt. Lett. **39**, 1081 (2014).
5. D. N. Vitek *et al*., Opt. Express **18**, 18,086 (2010).
6. G. Zhu *et al*., Opt. Express **13**, 2153 (2005).
7. H. Vincenti and F. Quéré, Phys. Rev. Lett. **108**, 113904 (2012).
8. Z. Sacks, G. Mourou, and R. Danielius, Opt. Lett. **26**, 462 (2001).
9. T. A. Planchon *et al*., Opt. Lett. **29**, 2300 (2004).
10. C. Dorrer and I. A. Walmsley, Opt. Lett. **27**, 1947 (2002).
11. J. Jasapara and W. Rudolph, Opt. Lett. **24**, 777 (1999).
12. A. P. Kovács *et al*., Appl. Phys. B **80**, 165 (2005).
13. P. Bowlan *et al*., Opt. Express **14**, 11,892 (2006).
14. P. Bowlan and R. Trebino, J. Opt. Soc. Am. B **29**, 244 (2012).
15. P. Gabolde and R. Trebino, Opt. Express **14**, 11,460 (2006).
16. J. Primot and N. Guérineau, Appl. Opt. **39**, 5715 (2000).
17. Z. Bor, J. Mod. Opt. **35**, 1907 (1988).

Publications and Conference Presentations

Publications

Y. Akbas, A. Stern, L. Q. Zhang, Y. Alimi, A. M. Song, I. Iñiguez-de-la-Torre, J. Mateos, T. González, G. W. Wicks, and R. Sobolewski, "Ultrahigh Responsivity of Optically Active, Semiconducting Asymmetric Nano-Channel Diodes," J. Phys.: Conf. Ser. **647**, 012013 (2015).

R. S. Craxton, K. S. Anderson, T. R. Boehly, V. N. Goncharov, D. R. Harding, J. P. Knauer, R. L. McCrory, P. W. McKenty, D. D. Meyerhofer, J. F. Myatt, A. J. Schmitt, J. D. Sethian, R. W. Short, S. Skupsky, W. Theobald, W. L. Kruer, K. Tanaka, R. Betti, T. J. B. Collins, J. A. Delettrez, S. X. Hu, J. A. Marozas, A. V. Maximov, D. T. Michel, P. B. Radha, S. P. Regan, T. C. Sangster, W. Seka, A. A. Solodov, J. M. Soures, C. Stoeckl, and J. D. Zuegel, "Direct-Drive Inertial Confinement Fusion: A Review," Phys. Plasmas **22**, 110501 (2015).

J. R. Davies, R. Betti, P.-Y. Chang, and G. Fiksel, "The Importance of Electrothermal Terms in Ohm's Law for Magnetized Spherical Implosions," Phys. Plasmas **22**, 112703 (2015).

C. Dorrer, L. J. Waxer, A. Kalb, E. M. Hill, and J. Bromage, "Single-Shot High-Resolution Characterization of Optical Pulses by Spectral Phase Diversity," Opt. Express **23**, 33,116 (2015).

S. X. Hu, L. A. Collins, V. N. Goncharov, J. D. Kress, R. L. McCrory, and S. Skupsky, "First-Principles Equation of State of Polystyrene and its Effect on Inertial Confinement Fusion Implosions," Phys. Rev. E **92**, 043104 (2015).

M. Margala, H. Wu, and R. Sobolewski, "Ballistic Deflection Transistors and Their Application to THz Amplification," J. Phys.: Conf. Ser. **647**, 012020 (2015).

K. L. Marshall, E. R. Sekera, and K. Xiao, "Computational Chemistry Modeling and Design of Photoswitchable Alignment Materials for Optically Addressable Liquid Crystal Devices," Proc. SPIE **9565**, 95650T (2015) (invited).

S. Papernov, A. A. Kozlov, J. B. Oliver, C. Smith, L. Jensen, D. Ristau, S. Günster, and H. Mädebach, "The Role of Film Interfaces in Near-Ultraviolet Absorption and Pulsed-Laser Damage in Ion-Beam–Sputtered Coatings Based on HfO_2/SiO_2 Thin-Film Pairs," Proc. SPIE **9632**, 96320B (2015).

B. W. Plansinis, W. R. Donaldson, and G. P. Agrawal, "What is the Temporal Analog of Reflection and Refraction of Optical Beams?" Phys. Rev. Lett. **115**, 183901 (2015).

S. Salzman, L. J. Giannechini, H. J. Romanofsky, N. Golini, B. Taylor, S. D. Jacobs, and J. C. Lambropoulos, "Advanced Zirconia-Coated Carbonyl-Iron Particles for Acidic Magneto-rheological Finishing of Chemical-Vapor–Deposited ZnS and Other IR Materials," Proc. SPIE **9633**, 963307 (2015).

J. Serafini, Y. Akbas, L. Crandall, R. Bellman, C. Kosik Williams, and R. Sobolewski, "Nonequilibrium Carrier Dynamics in Ultrathin Si-on-Glass Films," J. Phys.: Conf. Ser. **647**, 012032 (2015).

W. T. Shmayda, M. Sharpe, A. M. Boyce, R. Shea, B. Petroski, and W. U. Schröder, "Dependence of Tritium Release From Stainless Steel on Temperature and Water Vapor," Fusion Sci. Technol. **68**, 766 (2015).

Forthcoming Publications

B. P. Chock, T. B. Jones, and D. R. Harding, "Effect of a Surfactant on the Electric-Field Assembly of Oil/Water Emulsions for Making Foam Targets," to be published in Fusion Science and Technology.

R. Epstein, S. P. Regan, B. A. Hammel, L. J. Suter, H. A. Scott, M. A. Barrios, D. K. Bradley, D. A. Callahan, C. Cerjan, G. W. Collins, S. N. Dixit, T. Döppner, M. J. Edwards, D. R. Farley, K. B. Fournier, S. Glenn, S. H. Glenzer, I. E. Golovkin, A. Hamza, D. G. Hicks, N. Izumi, O. S. Jones, M. H. Key, J. D. Kilkenny, J. L. Kline, G. A. Kyrala, O. L. Landen, T. Ma, J. J. MacFarlane, A. J. Mackinnon, R. C. Mancini, R. L. McCrory, D. D. Meyerhofer, N. B. Meezan, A. Nikroo, H.-S. Park, P. K. Patel, J. E. Ralph, B. A. Remington, T. C. Sangster, V. A. Smalyuk, P. T. Springer, R. P. J. Town, and J. L. Tucker, "Applications and Results of X-Ray Spectroscopy in Implosion Experiments on the National Ignition Facility," to be published in the Proceedings of Atomic Processes in Plasmas (invited).

D. R. Harding, D. C. Whitaker, and C. Fella, "Growth of a Solid DT Crystal from the Liquid Inside Inertial Confinement Fusion Targets," to be published in Fusion Science and Technology.

V. V. Ivanov, A. A. Anderson, and I. A. Begishev, "Four-Color Laser Diagnostics for Z-Pinch and Laser-Produced Plasma," to be published in Applied Optics.

F. J. Marshall, P. B. Radha, M. J. Bonino, J. A. Delettrez, R. Epstein, V. Yu. Glebov, and D. R. Harding, "Polar-Direct-Drive Experiments with Contoured-Shell Targets on OMEGA," to be published in Physics of Plasmas.

P. B. Radha, V. N. Goncharov, M. Hohenberger, T. C. Sangster, R. Betti, R. S. Craxton, D. H. Edgell, R. Epstein, D. H. Froula, J. A. Marozas, F. J. Marshall, R. L. McCrory, P. W. McKenty, D. D. Meyerhofer, D. T. Michel, S. X. Hu, W. Seka, A. Shvydky, S. Skupsky, J. A. Frenje, M. Gatu Johnson, R. D. Petrasso, T. Ma, S. Le Pape, and A. J. Mackinnon, "Direct-Drive–Implosion Physics: Results from OMEGA and the National Ignition Facility," to be published in the Journal of Physics: Conference Series.

S. Salzman, H. J. Romanofsky, L. J. Giannechini, S. D. Jacobs, and J. C. Lambropoulus, "Magnetorheological Finishing of Chemical-Vapor–Deposited Zinc Sulfide via Chemically and Mechanically Modified Fluids," to be published in Applied Optics.

S. Salzman, H. J. Romanofsky, S. D. Jacobs, and J. C. Lambropoulos, "Surface-Texture Evolution of Different Chemical-Vapor-Deposited Zinc Sulfide Flats Polished with Various Magnetorheological Fluids," to be published in Precision Engineering.

J. Serafini, Y. Wang, R. Bellman, C. K. Williams, and R. Sobolewski, "Time-Resolved Carrier Dynamics of Thin Film Si-on-Glass Absorbers for Photovoltaic Cells," to be published in Semiconductor Science and Technology.

M. Sharpe, W. T. Shmayda, and W. U. Schröder, "Tritium Migration to the Surfaces of Stainless-Steel 316, Aluminum 6061, and Oxygen-Free, High-Conductivity Copper," to be published in Fusion Science and Technology.

N. D. Viza, M. H. Romanofsky, M. J. Moynihan, and D. R. Harding, "The Effect of a Surfactant on the Operation of T-Junctions for Mass-Producing Foam Targets," to be published in Fusion Science and Technology.

Conference Presentations

D. Polsin, T. R. Boehly, S. Ivancic, M. C. Gregor, C. A. McCoy, D. D. Meyerhofer, D. E. Fratanduono, and P. M. Celliers, "Probing the Release of Shocked Material," 3rd High-Power Laser Workshop, Menlo Park, CA, 5–6 October 2015.

The following presentations were made at the Industrial Associates Fall 2015 Meeting, Rochester, NY, 12–13 October 2015:

B. W. Plansinis, G. P. Agrawal, and W. R. Donaldson, "Temporal Analog of Reflection and Refraction."

K. A. Sharma, T. A. Germer, J. D. Zuegel, and T. G. Brown, "A Review of Scattered Light Analysis for Distributed Polarization Rotators."

The following presentations were made at Optifab 2015, Rochester, NY, 12–15 October 2015:

S. Salzman, L. J. Giannechini, H. J. Romanofsky, N. Golini, B. Taylor, S. D. Jacobs, and J. C. Lambropoulos, "Advanced Zirconia-Coated Carbonyl-Iron Particles for Acidic Magnetorheological Finishing of Chemical-Vapor–Deposited ZnS and Other IR Materials."

K. Tinkham, T. Jacobs, M. Mayton, Z. Hobbs, K. L. Marshall, and S. D. Jacobs, "Cerium Oxide Polishing Slurry Reclamation Project: Characterization Techniques and Results."

W. T. Shmayda, "Tritium Operations at the Laboratory for Laser Energetics," Health Physics Society, Rochester, NY, 15 October 2015.

The following presentations were made at Frontiers in Optics, San Jose, CA, 18–22 October 2015:

T. Petersen and J. Bromage, "A High-Average-Power, Degenerate, 2.06 μm BiB_3O_6 Femtosecond Optical Parametric Oscillator."

B. W. Plansinis, G. P. Agrawal, and W. R. Donaldson, "Temporal Analog of Reflection and Refraction."

R. L. McCrory, "From ALPHA to OMEGA EP—The History of LLE," OSA Rochester Section, Rochester, NY, 27 October 2015.

W. Theobald, "Shock Ignition—An Alternative Concept for Laser Fusion," GSI Presentation, Darmstadt, Germany, 27 October 2015 (invited).

The following presentations were made at the Tritium Focus Group, Los Alamos, NM, 3–5 November 2015:

W. T. Shmayda, "Radiological Challenges at the Laboratory for Laser Energetics."

W. T. Shmayda, M. Sharpe, and M. Cody, "Modeling Tritium on Metal Surfaces."

W. R. Donaldson, "Electro-Optic Measurements on the OMEGA Laser System: How to do Small Science in a Big Science Environment," 39th Annual IEEE EDS Activities in Western New York Conference, Rochester, NY, 6 November 2015 (invited).

The following presentations were made at the 57th Annual Meeting of the APS Division of Plasma Physics, Savannah, GA, 16–20 November 2015:

K. S. Anderson, P. W. McKenty, A. Shvydky, J. P. Knauer, T. J. B. Collins, J. A. Delettrez, D. Keller, and M. M. Marinak, "Characterizing Hot-Spot Dynamics of Direct-Drive Cryogenic Implosions on OMEGA."

D. H. Barnak, R. Betti, P.-Y. Chang, and J. R. Davies, "First Results from Laser-Driven MagLIF Experiments on OMEGA: Time Evolution of Laser Gas Heating Using Soft X-Ray Diagnostics."

P. X. Belancourt, P. A. Keiter, R. P. Drake, W. Theobald, T. J. B. Collins, M. J. Bonino, and P. Kozlowski, "Equation-of-State Measurements of Resorcinol Formaldehyde Foam Using Imaging X-Ray Thomson Spectrometer."

T. R. Boehly, M. J. Rosenberg, M. Hohenberger, D. N. Polsin, P. B. Radha, A. Shvydky, V. N. Goncharov, D. R. Harding, S. P. Regan, T. C. Sangster, P. M. Celliers, D. E. Fratanduono, and S. N. Dixit, "Polar-Direct-Drive Shock-Timing Measurements at the National Ignition Facility."

A. Bose, R. Betti, K. M. Woo, A. R. Christopherson, and D. Shvarts, "Effects of Long- and Intermediate-Wavelength Asymmetries on Hot-Spot Energetics."

D. Cao, J. A. Marozas, T. J. B. Collins, P. B. Radha, and P. W. McKenty, "A New Immediate Far-Field Spot Design for Polar Direct Drive at the National Ignition Facility."

P.-Y. Chang, D. H. Barnak, R. Betti, E. M. Campbell, J. R. Davies, J. P. Knauer, K. J. Peterson, A. B. Sefkow, D. B. Sinars, S. A. Slutz, and G. Fiksel, "First Results from Laser-Driven MagLIF Experiments on OMEGA: Optimization of Illumination Uniformity."

A. R. Christopherson, A. Bose, K. M. Woo, J. Howard, K. S. Anderson, E. M. Campbell, J. A. Delettrez, V. N. Goncharov, F. J. Marshall, R. L. McCrory, S. P. Regan, T. C. Sangster, C. Stoeckl, W. Theobald, M. J. Edwards, R. Nora, B. K. Spears, J. Sanz, O. A. Hurricane, J. D. Lindl, P. K. Patel, and D. Shvarts, "Alpha Heating and Burning Plasmas in Inertial Confinement Fusion" (invited).

T. J. B. Collins, J. A. Marozas, S. Skupsky, D. Cao, P. W. McKenty, J. A. Delettrez, and G. Moses, "Design Options for Polar-Direct-Drive Targets: From Alpha Heating to Ignition."

R. S. Craxton, Y. Z. Kong, E. M. Garcia, P. Huang, J. Kinney, P. W. McKenty, R. Zhang, S. Le Pape, F. Coppari, R. F. Heeter, B. J. MacGowan, J. R. Rygg, and M. B. Schneider, "Beam-Pointing Designs for Exploding-Pusher Proton and X-Ray Backlighting Targets at the National Ignition Facility."

A. Davies, S. Bucht, J. Katz, D. Haberberger, J. Bromage, J. D. Zuegel, D. H. Froula, P. A. Norreys, R. Bingham, J. Saldler, R. Trines, and L. O. Silva, "A Tunable (1100-nm to 1500-nm) 50-mJ Laser Enables a Pump-Depleting Plasma-Wave Amplifier."

J. R. Davies, D. H. Barnak, R. Betti, E. M. Campbell, P.-Y. Chang, G. Fiksel, W. Seka, K. J. Peterson, A. B. Sefkow, D. B. Sinars, and S. A. Slutz, "First Results from Laser-Driven MagLIF Experiments on OMEGA: Backscatter and Transmission Measurements of Laser Preheating."

A. K. Davis, D. Cao, D. T. Michel, D. H. Edgell, R. Epstein, V. N. Goncharov, M. Hohenberger, S. X. Hu, I. V. Igumenshchev, J. A. Marozas, A. V. Maximov, J. F. Myatt, P. B. Radha, S. P. Regan, T. C. Sangster, J. G. Shaw, D. H. Froula, M. Lafon, J. D. Moody, and R. J. Wallace, "Angularly Resolved Mass Ablation Rate and Ablation-Front-Trajectory Measurements at the Omega Laser and National Ignition Facilities" (invited).

J. A. Delettrez, B. Yaakobi, J. F. Myatt, and D. H. Edgell, "Recent Advances in the Transport Modeling of Two-Plasmon–Decay Electrons in the 1-D Hydrodynamic Code *LILAC*."

T. Eckert, A. Gula, L. Vincett, M. Yuly, S. J. Padalino, M. Russ, A. Simone, D. Ellison, M. Bienstck, H. Desmitt, T. C. Sangster, and S. P. Regan, "Efficiency Calibration for Measuring the $^{12}C(n,2n)^{11}C$ Cross-Section."

D. H. Edgell, R. K. Follett, V. N. Goncharov, I. V. Igumenshchev, J. Katz, J. F. Myatt, W. Seka, and D. H. Froula, "Diagnosing Cross-Beam Energy Transfer Using Beamlets of Unabsorbed Light from Direct-Drive Implosions."

R. Epstein, M. J. Rosenberg, A. A. Solodov, J. F. Myatt, S. P. Regan, W. Seka, M. Hohenberger, M. A. Barrios, and J. D. Moody, "Application and Analysis of the Isoelectronic Line Ratio Temperature Diagnostic in a Planar Ablating-Plasma Experiment at the National Ignition Facility."

T. M. Filkins, J. A. Steidle, R. Ward, C. Freeman, T. C. Sangster, and S. P. Regan, "Radiochromic Film Sensitivity Calibrations Using Ion Beams from a Palletron Accelerator."

R. K. Follett, J. G. Shaw, D. H. Edgell, R. J. Henchen, S. X. Hu, J. Katz, D. T. Michel, J. F. Myatt, A. A. Solodov, C. Stoeckl, B. Yaakobi, and D. H. Froula, "Modeling Hot-Electron Measurements in Multibeam Two-Plasmon–Decay Experiments."

C. J. Forrest, V. Yu. Glebov, J. P. Knauer, P. B. Radha, S. P. Regan, T. C. Sangster, C. Stoeckl, W. U. Schröeder, J. A. Frenje, M. Gatu Johnson, M. W. Paris, G. Hale, and A. B. Zylstra, "Neutron Induced Deuterium Breakup in Inertial Confinement Fusion at the Omega Laser Facility."

D. H. Froula, R. K. Follett, R. J. Henchen, V. N. Goncharov, D. T. Michel, A. A. Solodov, J. A. Delettrez, D. H. Edgell, B. Yaakobi, C. Stoeckl, and J. F. Myatt, "Mitigation of Two-Plasmon Decay in Direct-Drive Implosions Using Multilayer Targets."

V. Yu. Glebov, C. J. Forrest, J. P. Knauer, S. P. Regan, T. C. Sangster, and C. Stoeckl, "A New Neutron Time-of-Flight Detector for DT Yield and Ion-Temperature Measurements on OMEGA."

V. N. Goncharov, S. P. Regan, T. C. Sangster, R. Betti, T. R. Boehly, M. J. Bonino, E. M. Campbell, T. J. B. Collins, R. S. Craxton, J. A. Delettrez, D. H. Edgell, R. Epstein, C. J. Forrest, D. H. Froula, V. Yu. Glebov, D. R. Harding, S. X. Hu, I. V. Igumenshchev, R. T. Janezic, J. H. Kelly, T. J. Kessler, T. Z. Kosc, S. J. Loucks, J. A. Marozas, F. J. Marshall, R. L. McCrory, P. W. McKenty, D. D. Meyerhofer, D. T. Michel, J. F. Myatt, P. B. Radha, W. Seka, W. T. Shmayda, A. Shvydky, S. Skupsky, C. Stoeckl, W. Theobald, F. Weilacher, B. Yaakobi,

J. A. Frenje, M. Gatu Johnson, R. D. Petrasso, S. P. Obenschain, and M. Karasik, "Cross-Beam Energy Transfer Mitigation in Cryogenic Implosions on OMEGA."

X. Gong, V. N. Goncharov, and I. V. Igumenshchev, "A 3-D Model of Hot-Spot Formation in Inertial Confinement Fusion Implosions."

M. C. Gregor, T. R. Boehly, C. A. McCoy, D. N. Polsin, D. D. Meyerhofer, D. E. Fratanduono, P. M. Celliers, and G. W. Collins, "The Release Behavior of Diamond Shocked to 25 Mbar."

D. Haberberger, D. H. Froula, S. X. Hu, C. Joshi, S. Tochitsky, C. Gong, F. Fiuza, and L. Silva, "Shock-Wave Acceleration of Ions on OMEGA EP."

R. J. Henchen, S. X. Hu, R. K. Follett, J. Katz, V. N. Goncharov, D. H. Froula, and W. Rozmus, "Heat-Flux Measurements from Collective Thomson-Scattering Spectra."

M. Hohenberger, A. Shvydky, P. B. Radha, M. J. Rosenberg, V. N. Goncharov, S. Le Pape, F. J. Marshall, D. T. Michel, J. P. Knauer, S. P. Regan, T. C. Sangster, S. R. Nagel, A. Nikroo, V. A. Smalyuk, and R. J. Wallace, "Hydrodynamic Instability Growth in Polar-Direct-Drive Implosions at the National Ignition Facility."

S. X. Hu, L. A. Collins, J. D. Kress, V. N. Goncharov, T. R. Boehly, R. L. McCrory, and S. Skupsky, "First-Principles Investigations on Thermal Conductivity and Average Ionization of CH Ablators Under Extreme Conditions."

I. V. Igumenshchev, V. N. Goncharov, F. J. Marshall, K. Silverstein, J. P. Knauer, D. H. Froula, and S. P. Regan, "Numerical Study of Large-Scale, Laser-Induced Nonuniformities in Cryogenic OMEGA Implosions."

S. Ivancic, P. M. Nilson, C. R. Stillman, C. Mileham, and D. H. Froula, "Design of an Extreme Ultraviolet Spectrometer Suite for Isochoric-Heated Warm-Dense-Matter Studies."

J. P. Knauer, M. Gatu Johnson, R. M. Bionta, E. J. Bond, D. K. Bradley, J. A. Caggiano, D. A. Callahan, D. T. Casey, C. J. Cerjan, T. Doeppner, M. J. Eckart, M. J. Edwards, J. A. Frenje, V. Yu. Glebov, G. P. Grim, E. P. Hartouni, R. Hatarik, D. E. Hinkel, O. A. Hurricane, W. W. Hsing, J. D. Kilkenny, A. Kritcher, O. L. Landen, S. Le Pape, T. Ma, A. J. Mackinnon, D. H. Munro, H.-S. Park, P. K. Patel, R. D. Petrasso, J. E. Ralph, B. A. Remington, T. C. Sangster, D. B. Sayre, B. K. Spears, and C. B. Yeamans, "Neutron Yield and Ion Temperature from DD and DT Fusion in National Ignition Facility High-Foot Implosions."

P. Lawson-Keister, J. Padawar-Curry, H. Visca, K. Fletcher, S. J. Padalino, T. C. Sangster, and S. P. Regan, "Characterizing ICF Neutron Scintillation Diagnostics on the nTOF Line at SUNY Geneseo."

J. Li, S. X. Hu, and C. Ren, "Effects of Laser–Plasma Instabilities on Hydro Evolution in Direct-Drive Inertial Confinement Fusion."

J. A. Marozas, T. J. B. Collins, P. W. McKenty, and J. D. Zuegel, "Improved Wavelength Detuning Cross-Beam Energy Transfer Mitigation Strategy for Polar Direct Drive at the National Ignition Facility."

F. J. Marshall, V. N. Goncharov, V. Yu. Glebov, S. P. Regan, T. C. Sangster, and C. Stoeckl, "Framed X-Ray Imaging of Cryogenic Target Implosion Cores on OMEGA."

A. V. Maximov, J. F. Myatt, R. W. Short, I. V. Igumenshchev, and W. Seka, "Beam Energy Exchange Driven by Incoherent Laser Beams with Frequency Detuning."

C. A. McCoy, M. C. Gregor, D. N. Polsin, T. R. Boehly, D. E. Fratanduono, P. M. Celliers, G. W. Collins, and D. D. Meyerhofer, "Measurements of Sound Velocity and Grüneisen Parameter in CH and MgO Shocked to TPa Pressures."

P. W. McKenty, J. A. Marozas, F. J. Marshall, J. Weaver, S. P. Obenschain, and A. J. Schmitt, "Evaluation of Wavelength Detuning to Mitigate Cross-Beam Energy Transfer Using the Nike Laser."

D. T. Michel, T. C. Sangster, V. N. Goncharov, A. K. Davis, I. V. Igumenshchev, R. Epstein, V. Yu. Glebov, S. X. Hu, D. D. Meyerhofer, S. P. Regan, W. Seka, A. Shvydky, C. Stoeckl, and D. H. Froula, "Measurements of the Conduction-Zone Length and Mass Ablation Rate in Cryogenic Direct-Drive Implosions on OMEGA to Restrict Thermal-Transport Models."

J. F. Myatt, J. G. Shaw, V. N. Goncharov, J. Zhang, A. V. Maximov, R. W. Short, R. K. Follett, W. Seka, D. H. Edgell, D. H. Froula, D. F. DuBois, D. A. Russell, and H. X. Vu, "A Numerical Model for Two-Plasmon–Decay Hot-Electron Production and Mitigation in Direct-Drive Implosions."

P. M. Nilson, G. Fiksel, C. Stoeckl, P. A. Jannimagi, C. Mileham, W. Theobald, J. R. Davies, J. F. Myatt, A. A. Solodov, D. H. Froula, R. Betti, and D. D. Meyerhofer, "Supersonic Propagation of a K-Shell Ionization Front in Metal Targets."

S. J. Padalino, A. Simone, E. Turner, M. K. Ginnane, M. Glisic, B. Kousar, A. Smith, T. C. Sangster, and S. P. Regan, "Time-Resolved Tandem Faraday Cup Development for High-Energy TNSA Particles."

D. N. Polsin, T. R. Boehly, S. Ivancic, M. C. Gregor, C. A. McCoy, K. S. Anderson, D. E. Fratanduono, P. M. Celliers, and D. D. Meyerhofer, "Probing the Release of Shocked Material."

P. B. Radha, M. Hohenberger, T. R. Boehly, T. J. B. Collins, R. S. Craxton, J. A. Delettrez, D. H. Edgell, D. H. Froula, V. N. Goncharov, S. X. Hu, J. P. Knauer, J. A. Marozas, F. J. Marshall, R. L. McCrory, P. W. McKenty, D. D. Meyerhofer, D. T. Michel, J. F. Myatt, S. P. Regan, M. J. Rosenberg, T. C. Sangster, W. Seka, A. Shvydky, S. Skupsky, J. A. Frenje, R. D. Petrasso, H. Sio, A. B. Zylstra, S. N. Dixit, S. Le Pape, J. W. Bates, M. Karasik, and S. P. Obenschein, "Direct Drive: Simulations and Experiments at the National Ignition Facility" (invited).

S. P. Regan, V. N. Goncharov, T. C. Sangster, R. Betti, T. R. Boehly, M. J. Bonino, E. M. Campbell, D. Cao, T. J. B. Collins, R. S. Craxton, A. K. Davis, J. A. Delettrez, D. H. Edgell, R. Epstein, C. J. Forrest, D. H. Froula, V. Yu. Glebov, D. R. Harding, M. Hohenberger, S. X. Hu, I. V. Igumenshchev, R. T. Janezic, J. H. Kelly, T. J. Kessler, J. P. Knauer, T. Z. Kosc, J. A. Marozas, F. J. Marshall, R. L. McCrory, P. W. McKenty, D. T. Michel, J. F. Myatt, P. B. Radha, M. J. Rosenberg, W. Seka, W. T. Shmayda, A. Shvydky, S. Skupsky, A. A. Solodov, C. Stoeckl, W. Theobald, M. D. Wittman, B. Yaakobi, J. D. Zuegel, J. A. Frenje, M. Gatu Johnson, R. D. Petrasso, S. P. Obenschain, M. Karasik, A. J. Schmitt, D. D. Meyerhofer, and M. J. Schmitt, "Energy Coupling and Hot-Spot Pressure in Direct-Drive Layered DT Implosions on OMEGA" (invited).

M. J. Rosenberg, A. A. Solodov, W. Seka, R. Epstein, J. F. Myatt, S. P. Regan, M. Hohenberger, T. J. B. Collins, D. P. Turnbull, P. Michel, J. D. Moody, J. E. Ralph, and M. A. Barrios, "Planar Two-Plasmon–Decay Experiments at Polar-Direct-Drive Ignition-Relevant Scale Lengths at the National Ignition Facility."

W. Seka, S. P. Regan, P. B. Radha, M. J. Rosenberg, M. Hohenberger, V. N. Goncharov, J. F. Myatt, J. E. Ralph, J. D. Moody, and D. P. Turnbull, "Stimulated Raman Scattering as Coronal T_e Diagnostic for Direct-Drive Experiments on the Current National Ignition Facility."

R. W. Short, A. V. Maximov, J. F. Myatt, W. Seka, and J. Zhang, "Absolute Two-Plasmon Decay and Stimulated Raman Scattering in Direct-Drive Irradiation Geometries."

A. Shvydky, M. Hohenberger, P. B. Radha, M. J. Rosenberg, R. S. Craxton, V. N. Goncharov, J. A. Marozas, F. J. Marshall, P. W. McKenty, S. P. Regan, and T. C. Sangster, "Numerical Simulations of Hydrodynamic Instability Growth and Imprint Experiments at the National Ignition Facility."

A. A. Solodov, M. J. Rosenberg, J. F. Myatt, R. Epstein, S. P. Regan, W. Seka, J. G. Shaw, M. Hohenberger, J. W. Bates, J. E. Moody, J. E. Ralph, D. P. Turnbull, and M. A. Barrios, "Modeling of Two-Plasmon–Decay Experiments at Direct-Drive Ignition-Relevant Plasma Conditions at the National Ignition Facility."

C. R. Stillman, P. M. Nilson, S. Ivancic, C. Mileham, D. D. Meyerhofer, D. H. Froula, M. E. Martin, and R. A. London, "X-Ray Spectroscopy of Rapidly Heated Buried-Aluminum Layers."

C. Stoeckl, C. J. Forrest, V. Yu. Glebov, T. C. Sangster, W. U. Schröder, and E. Henry, "Spectroscopy of Neutrons Generated Through Nuclear Reactions in Short-Pulse Laser Experiments."

A. Tantillo, M. C. Watson, E. Pogozelski, T. C. Sangster, and S. P. Regan, "Target Chamber Manipulator."

W. Theobald, R. Betti, W. Seka, A. Bose, D. T. Michel, C. Stoeckl, R. Yan, R. Nora, A. Casner, M. Lafon, X. Ribeyre, E. Llor-Aisa, A. Vallet, J. Peebles, F. N. Beg, and M. S. Wei, "Hot-Electron Generation in Various Ablator Materials at Shock-Ignition–Relevant Laser Intensities."

H. Wen, A. V. Maximov, R. Yan, C. Ren, J. Li, and J. F. Myatt, "Three-Dimensional Modeling of Laser–Plasma Interactions Near the Quarter-Critical Density in Plasmas."

M. P. Wiesner, R. Ume, J. G. McLean, T. C. Sangster, and S. P. Regan, "Enhancement of Particle Track Etch Rate in CR-39 by UV Exposure."

K. M. Woo, R. Betti, A. Bose, R. Epstein, J. A. Delettrez, K. S. Anderson, R. Yan, P.-Y. Chang, D. Jonathan, and M. Charissis,

"Three-Dimensional Simulations of the Deceleration Phase of Inertial Fusion Implosions Using *DEC3D*."

R. Yan, R. Betti, J. Sanz, B. Liu, and A. Frank, "Three-Dimensional Single-Mode Nonlinear Ablative Rayleigh–Taylor Instability."

J. Zhang, J. F. Myatt, R. W. Short, A. V. Maximov, H. X. Vu, D. F. DuBois, and D. A. Russell, "Self-Consistent Calculation of Half-Harmonic Emission Generated by the Two-Plasmon–Decay Instability."

D. R. Harding, B. Chock, W. Wang, Z. Bei, and T. B. Jones, "Electric-Field–Assisted Motion of Low-Surface–Energy Fluid Droplets on Dielectric Surfaces," 2015 MRS Fall Meeting, Boston, MA, 29 November–4 December 2015.

E. M. Campbell, D. Haberberger, A. Davies, S.-W. Bahk, J. Bromage, J. D. Zuegel, D. H. Froula, J. Sadler, and P. A. Norreys, "Ultrahigh Brightness Laser Development at the Laboratory for Laser Energetics," George Washington University, Washington, DC, 14 December 2015.

R. L. McCrory, "Perspectives on Inertial Fusion Energy," Fusion Power Associates, Washington, DC, 16–17 December 2015.


1850
MELIORA
UNIVERSITY of
ROCHESTER